Production of tau pairs at the Z resonance

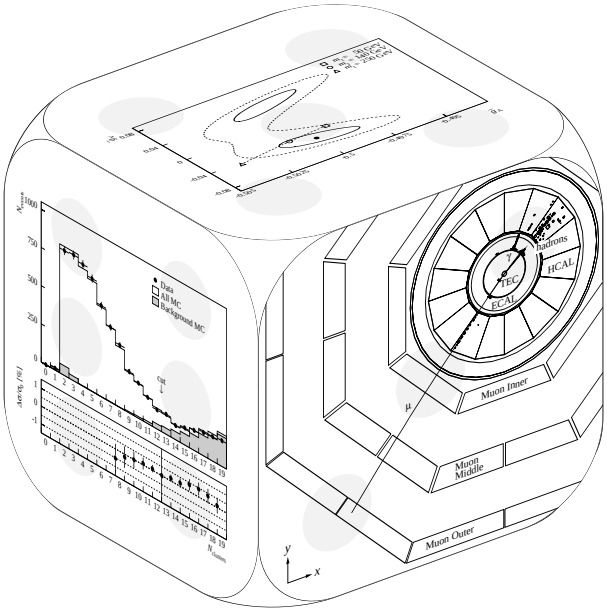

Xaveer Leijtens

Production of tau pairs at the Z resonance

ACADEMISCH PROEFSCHRIFT

TER VERKRIJGING VAN DE GRAAD VAN DOCTOR
AAN DE UNIVERSITEIT VAN AMSTERDAM
OP GEZAG VAN DE RECTOR MAGNIFICUS
PROF. DR. P.W.M. DE MEIJER
IN HET OPENBAAR TE VERDEDIGEN IN DE AULA DER UNIVERSITEIT
(OUDE LUTHERSE KERK, INGANG SINGEL 411, HOEK SPUI)
OP MAANDAG 29 NOVEMBER 1993 TE 12.00 UUR

door

Xaverius Jacques Maria Leijtens

geboren op 6 april 1962 te Uithoorn

Promotor:	Prof. Dr. P. Duinker
Co-promotor:	Dr. G.G.G. Massaro

The work described in this thesis is part of the research programme of ‘het Nationaal Instituut voor Kernfysica en Hoge-Energie Fysica (NIKHEF-H)’ in Amsterdam. The author was financially supported by ‘de Stichting voor Fundamenteel Onderzoek der Materie (FOM)’.

Contents

Introduction

The start of operation of the Large Electron-Positron collider LEP in 1989 opened a new era of precision experiments testing the electroweak interactions. The energy available at LEP is sufficient to produce the Z^0 boson in abundance. This heavy boson was predicted by the Standard Model, the theory describing the interactions between all fundamental particles. Together with the photon and the $\mathrm{W}^{\pm}$ bosons, the Z^0 is the carrier of the electroweak force. The Z^0 and $\mathrm{W}^{\pm}$ were first detected at CERN in 1983 [1].

The measurements of the properties of the Z^0 that are being performed at LEP provide a precise experimental determination of many of the Standard Model parameters, such as the mass and width of the Z^0 and the coupling of the Z^0 to fermions. The analysis presented in this thesis concerns the production of a pair of tau leptons through the process:

$$\mathrm{e}^+\mathrm{e}^- \rightarrow \mathrm{Z}^0 \rightarrow \tau^+\tau^-$$

The τ lepton is a sequential lepton: it is the third lepton in the sequence:

$$\begin{aligned} \mathrm{e}, &\quad \nu_{\mathrm{e}} \\ \mu, &\quad \nu_{\mu} \\ \tau, &\quad \nu_{\tau} \end{aligned}$$

where the e, μ and τ leptons differ only in mass, and each charged lepton has it's own (massless) neutrino: ν_{e}, ν_{μ} and ν_{τ}.

Ever since the discovery of the muon, people realized that other heavy leptons may also exist in nature. New leptons have been searched for in the weak decay of hadrons, in the interactions of neutrinos and in $\mathrm{e}^+\mathrm{e}^-$ collisions. The searches for heavy leptons, $L^{\pm}$, using the signature:

$$\begin{aligned} \mathrm{e}^+\mathrm{e}^- &\rightarrow L^+L^- \\ L^+ &\rightarrow \mathrm{e}^+\nu_{\mathrm{e}}\bar{\nu}_{\mathrm{L}} \\ L^- &\rightarrow \mu^-\bar{\nu}_{\mu}\nu_{\mathrm{L}} \end{aligned}$$

began in 1973 at the ADONE $\mathrm{e}^+\mathrm{e}^-$ storage ring [2], but were negative due to too small energy of the machine. In 1975, the first evidence for a new lepton was observed by the MARK I detector

at SPEAR [3]. Events were found in e^+e^- annihilations at a center of mass energy of 4.8 GeV which contained an electron and a muon and no other visible charged or neutral particles. These events could not be explained from known processes and their properties suggested they came from the decay of a pair of heavy leptons. The new lepton was named τ after the Greek word $\tau\rho\iota\alpha$ (three), since it is the third known charged lepton. The tau was the first particle of the third family of elementary fermions. Up to its discovery, there had been only two families: the first family containing the electron, electron neutrino and the up and down quarks; the second family containing the muon, muon neutrino and the strange and charm quarks. The existence of a third family had been suggested already in 1973 by Kobayashi and Maskawa [4] as possible solution for the CP violation problem. In 1977 the first quark of the third family, the bottom quark, was discovered [5]. The third family is completed by the tau neutrino and the top quark, but these particles have not yet been observed directly.

Many of the properties of the tau, like its mass, spin, decay branching ratios and coupling to the photon, have been experimentally well determined at the e^+e^- machines preceding LEP. LEP provides a laboratory for testing the Standard Model parameters at an energy around the mass of the Z^0, where the cross section is sharply peaked and eventually millions of Z^0 events will be available for analysis. Through the predicted universality of the Z^0 couplings to the three fermion families, members of the third family should be produced at LEP just as copiously as those of the first two. The analysis presented in this thesis aims at an accurate determination of the couplings of the Z^0 to tau leptons and a detailed comparison of the results with those of the other fermions, thereby checking the relations predicted by the Standard Model.

This thesis is organized as follows. The first chapter discusses the theoretical background relevant for the experimental analysis. It treats the calculation of the tau pair cross section and forward-backward charge asymmetry and the electroweak radiative corrections. The experimental apparatus, the L3 detector at the LEP e^+e^- collider, is described in the second chapter. Chapter 3 discusses the L3 muon chamber alignment system. This alignment system is required for obtaining high precision muon momentum measurements. Chapters 4 and 5 treat the experimental measurements of the tau pair cross section and forward-backward charge asymmetry. The event sample selection and background subtraction and the calculations of the experimental values are discussed in detail. The measurements are interpreted in terms of the Standard Model parameters in chapter 6.

Chapter 1

Theory

This chapter discusses the theoretical background necessary for the interpretation of the experimental results on τ pair production at LEP energies presented in this thesis. First some general aspects of the Standard Model are described. Sections 1.2 and 1.3 treat the calculation of the tau pair cross section and forward-backward charge asymmetry in lowest order. The tau pair polarization asymmetry is described in section 1.4. The last section treats the electroweak radiative corrections.

1.1 The Standard Model

The principle constituents of matter are spin 1/2 fermions. These fermions are either leptons or quarks and can be grouped in families of two leptons and two quarks each. The families are listed in table 1.1, together with the electric charge Q for the particles and the value of I_3, the third component of the weak isospin. The quarks and leptons are considered to be pointlike

	Family			Q/e	I_3
	1	2	3		
Leptons	ν_{e}	ν_μ	(ν_τ)	0	$+1/2$
	e	μ	τ	-1	$-1/2$
Quarks	u	c	(t)	2/3	$+1/2$
	d	s	b	$-1/3$	$-1/2$

Table 1.1 The three lepton and quark families. The values of the electric charge Q and of the third component of the weak isospin I_3 are listed for the various particles. The particles in brackets have not yet been directly observed.

particles. The particles are subject to the following interactions*:

Electromagnetic interaction between all charged particles is mediated by the exchange of massless photons (γ). The theory describing this interaction is Quantum Electro Dynamics (QED).

Weak interaction between all quarks and leptons is mediated by massive vector bosons. There are two kinds of weak interactions: charged, mediated by the $\mathrm{W}^{\pm}$ and neutral, mediated by the Z^0. The theory describing this interaction, the Glashow-Weinberg-Salam (GWS) theory of electroweak interactions [6], treats weak and electromagnetic interactions as different manifestations of a single electroweak force.

Strong interaction between all particles carrying color charge (quarks) is mediated by the exchange of massless gluons. The theory describing this interaction is Quantum Chromo Dynamics (QCD).

All interactions listed above have been incorporated in a single theoretical model known as the Standard Model. This model is characterized by the gauge group $\mathrm{SU}(3)_C \times \mathrm{SU}(2)_L \times \mathrm{U}(1)_Y$. The group $\mathrm{SU}(3)_C$ corresponds to the strong interaction and the group $\mathrm{SU}(2)_L \times \mathrm{U}(1)_Y$ corresponds to the GWS theory and is referred to as the Standard Model of electroweak interactions. The left handed fermions are arranged in weak isodoublets; the right handed fermions are weak isosinglets, and right handed neutrinos should not exist. Table 1.1 only lists the left handed fermions. In the Standard Model, the Higgs mechanism is responsible for the masses of the vector bosons, through spontaneous symmetry breaking [7]. All fermions are assumed to acquire their mass through their interaction with the Higgs field.

The Standard Model with three families contains 18 free parameters. They are the three lepton masses, the six quark masses, three quark mixing angles and one phase, the mass and vacuum expectation value of the Higgs boson and three coupling constants. In the electroweak sector one normally chooses instead of the vacuum expectation value and two coupling constants three parameters that correspond more directly to physically measurable quantities. For Z^0 physics at LEP the natural choice is given by the electromagnetic fine structure constant α, and the masses of the $\mathrm{W}^{\pm}$ and Z^0 bosons. Since m_{W} has not yet been measured accurately—this will be done at LEP in the future—the precisely known Fermi constant G_μ is used in stead of m_{W}.

The tree level diagrams of the electroweak couplings to fermions and the coupling constants are summarized as follows:

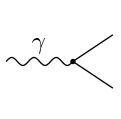

$= -ieQ_f\gamma_\mu$ (Here f is any quark or lepton and $e = \sqrt{4\pi\alpha}$)

*Gravitational interaction between particles is too weak to play a significant role at accelerator energies.

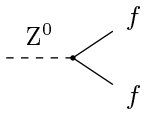

$$= \frac{-ie\gamma_\mu(g_{\rm V}^f - g_{\rm A}^f\gamma_5)}{2\sin\theta_{\rm W}\cos\theta_{\rm W}}$$

(Here f is any quark or lepton)

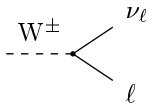

$$= \frac{-ie\gamma_\mu(1-\gamma_5)}{2\sqrt{2}\sin\theta_{\rm W}}$$

(Here ℓ is any lepton and ν_ℓ the corresponding neutrino)

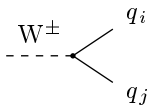

$$= \frac{-ie\gamma_\mu(1-\gamma_5)}{2\sqrt{2}\sin\theta_{\rm W}} \cdot U_{ij}$$

(Here $i = \mathrm{u}$, c or t and $j = \mathrm{d}$, s or b; U is the Kobayashi-Maskawa matrix)

The γ_i ($i = 1, 2, 3, 4, 5$) are the Dirac gamma matrices and the vector and axial vector coupling constants

$$\begin{aligned} g_{\rm V}^f &= I_3^f - 2Q_f\sin^2\theta_{\rm W} \\ g_{\rm A}^f &= I_3^f \end{aligned} \tag{1.1}$$

where I_3^f and Q_f denote the third isospin component and the electric charge of a given fermion species, respectively, as listed in table 1.1 and $\theta_{\rm W}$ is the weak mixing angle defined in terms of the W and Z masses as:

$$\sin^2\theta_{\rm W} = 1 - \frac{m_{\rm W}^2}{m_{\rm Z}^2} \tag{1.2}$$

Within the Standard Model the masses of the W and Z are related to the Fermi constant G_μ and the electromagnetic coupling constant α. Both the coupling constants G_μ and α are known with high accuracy. In lowest order approximation the relation is:

$$G_\mu = \frac{\pi\alpha}{\sqrt{2}}\frac{1}{m_{\rm W}^2\sin^2\theta_{\rm W}} \tag{1.3}$$

The analysis presented in this thesis concerns the tau pair production from $\mathrm{e^+e^-}$ annihilations, hence the cases of interest are $f \equiv \mathrm{e}$ and $f \equiv \tau$. Using the values from table 1.1 the vector and axial vector coupling constants then become:

$$\begin{aligned} g_{\rm V}^{\mathrm{e},\tau} &= -\tfrac{1}{2} + 2\sin^2\theta_{\rm W} \\ g_{\rm A}^{\mathrm{e},\tau} &= -\tfrac{1}{2} \end{aligned} \tag{1.4}$$

where one may note that $|g_{\rm V}| \ll |g_{\rm A}|$ since experimentally $\sin^2\theta_{\rm W} \simeq 0.23$.

1.2 Cross section

In lowest order, or so-called Born approximation, two Feynman diagrams contribute to the process $\mathrm{e^+e^-} \to \tau^+\tau^-$, as is shown in figure 1.1. Neglecting terms of the order m_τ^2/s, where

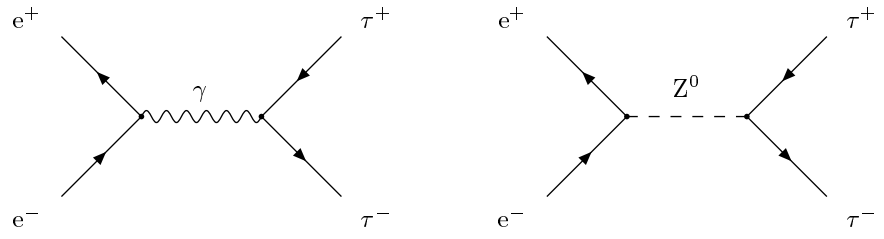

Figure 1.1 Feynman diagrams for the process $e^+e^- \to \tau^+\tau^-$ in lowest order.

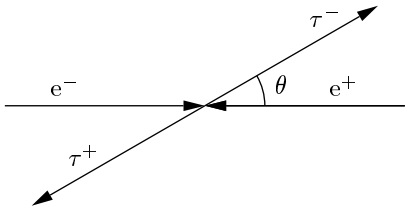

Figure 1.2 Definition of the polar angle θ between the incoming e^- and the outgoing τ^-.

m_τ is the tau mass and s the center of mass energy squared, the differential cross section for this process can than be written as follows [8]:

$$\frac{d\sigma}{d\Omega} = \frac{\alpha^2}{4s}\left\{A(s)(1+\cos^2\theta) + 2B(s)\cos\theta\right\} \tag{1.5}$$

where $d\Omega = d\phi\, d\cos\theta$ with ϕ the azimuthal angle and θ is the scattering angle in the center of mass system, as defined in figure 1.2 and

$$A = 1 + \frac{G_\mu m_Z^2}{\sqrt{2}\pi\alpha} g_V^e g_V^\tau \mathrm{Re}\chi(s) + \frac{G_\mu^2 m_Z^4}{8\pi^2\alpha^2}\left((g_V^e)^2 + (g_A^e)^2\right)\left((g_V^\tau)^2 + (g_A^\tau)^2\right)|\chi(s)|^2 \tag{1.6}$$

$$B = \frac{G_\mu m_Z^2}{\sqrt{2}\pi\alpha} g_A^e g_A^\tau \mathrm{Re}\chi(s) + \frac{G_\mu^2 m_Z^4}{2\pi^2\alpha^2} g_V^e g_A^e g_V^\tau g_A^\tau |\chi(s)|^2 \tag{1.7}$$

where $\chi(s)$ is the Z^0 propagator in lowest order:

$$\chi(s) = \frac{s}{s - m_Z^2 + i m_Z \Gamma_Z} \tag{1.8}$$

and

$$\Gamma_{\mathrm{Z}} = \sum_f \frac{N_C^f G_\mu m_{\mathrm{Z}}^3}{6\sqrt{2}\pi}\sqrt{1-4\frac{m_f^2}{s}}\left((g_{\mathrm{V}}^f)^2(1+2\frac{m_f^2}{s})+(g_{\mathrm{A}}^f)^2(1-4\frac{m_f^2}{s})\right) \tag{1.9}$$

is the total width of the Z^0, with the QCD color factor $N_C^f = 1$ for leptons and $N_C^f = 3$ for quarks.

Integrating the expression for the differential cross section (1.5) over the full solid angle gives the total cross section:

$$\sigma(s) = \frac{s}{(s-m_{\mathrm{Z}}^2)^2+m_{\mathrm{Z}}^2\Gamma_{\mathrm{Z}}^2}\left\{\frac{12\pi\Gamma_{\mathrm{e}}\Gamma_\tau}{m_{\mathrm{Z}}^2}+\frac{(s-m_{\mathrm{Z}}^2)I}{s}\right\}+\frac{4\pi\alpha^2}{3s} \tag{1.10}$$

where

$$\Gamma_{\mathrm{e},\tau} = \frac{G_\mu m_{\mathrm{Z}}^3}{6\pi\sqrt{2}}\left((g_{\mathrm{V}}^{\mathrm{e},\tau})^2+(g_{\mathrm{A}}^{\mathrm{e},\tau})^2\right) \tag{1.11}$$

is the partial width of $\mathrm{Z}^0 \to \mathrm{e}^+\mathrm{e}^-,\ \tau^+\tau^-$. The first term in eq. (1.10) is the Breit-Wigner Z exchange term, the last is the γ exchange term and the second term is the γ-Z interference term, with

$$I = \tfrac{2}{3}\sqrt{2}\alpha G_\mu m_{\mathrm{Z}}^2 g_{\mathrm{V}}^{\mathrm{e}} g_{\mathrm{V}}^{\tau} \tag{1.12}$$

The total width of the Z^0, Γ_{Z}, can be split in three parts:

$$\Gamma_{\mathrm{Z}} = \Gamma_{\mathrm{had}} + \Gamma_{\mathrm{lep}} + \Gamma_{\mathrm{inv}}$$

where Γ_{had} is the total hadronic width, $\Gamma_{\mathrm{lep}} = \Gamma_{\mathrm{e}} + \Gamma_\mu + \Gamma_\tau$, the total leptonic width and Γ_{inv}, the invisible width, is $N_\nu\Gamma_\nu$, with N_ν the number of light neutrinos[†] and Γ_ν the partial width of $\mathrm{Z}^0 \to \bar{\nu}\nu$. In the Standard Model each neutrino connects to only one family, so the number of light neutrinos is equal to the total number of families. Results of L3 measurements determine the number of light neutrinos to be $N_\nu = 2.98 \pm 0.06$ [9], from which follows that there exist no more than the three families listed in table 1.1.

1.3 Forward-backward charge asymmetry

The forward-backward charge asymmetry A_{FB} is defined as:

$$A_{\mathrm{FB}} = \frac{\sigma_{\mathrm{F}} - \sigma_{\mathrm{B}}}{\sigma_{\mathrm{F}} + \sigma_{\mathrm{B}}} \tag{1.13}$$

with

$$\sigma_{\mathrm{F}} = 2\pi\int_0^1 \mathrm{d}(\cos\theta)\frac{\mathrm{d}\sigma}{\mathrm{d}\Omega};\quad \sigma_{\mathrm{B}} = 2\pi\int_{-1}^0 \mathrm{d}(\cos\theta)\frac{\mathrm{d}\sigma}{\mathrm{d}\Omega} \tag{1.14}$$

[†] This is valid if the invisible width is entirely due to light neutrinos. In this context a 'light' neutrino is a neutrino with mass $m_\nu \ll m_{\mathrm{Z}}/2$. All present data is consistent with the neutrinos being massless.

and $\mathrm{d}\sigma/\mathrm{d}\Omega$ as in (1.5). After substitution of (1.5) the asymmetry becomes:

$$A_{\mathrm{FB}}(s) = \frac{3}{4}\frac{B(s)}{A(s)} \tag{1.15}$$

with A and B as in (1.6) and (1.7). Neglecting the terms $(\Gamma_{\mathrm{Z}}/m_{\mathrm{Z}})^2$ gives an on-resonance asymmetry $(s = m_{\mathrm{Z}}^2)$ [10]:

$$A_{\mathrm{FB}}(m_{\mathrm{Z}}^2) = \frac{3}{4}\frac{2g_{\mathrm{V}}^{\mathrm{e}}g_{\mathrm{A}}^{\mathrm{e}}}{((g_{\mathrm{V}}^{\mathrm{e}})^2+(g_{\mathrm{A}}^{\mathrm{e}})^2)}\frac{2g_{\mathrm{V}}^{\tau}g_{\mathrm{A}}^{\tau}}{((g_{\mathrm{V}}^{\tau})^2+(g_{\mathrm{A}}^{\tau})^2)} \tag{1.16}$$

Near the Z^0 resonance, again neglecting terms of order $(\Gamma_{\mathrm{Z}}/m_{\mathrm{Z}})^2$ and using $g_{\mathrm{V}}^2 \ll g_{\mathrm{A}}^2$, the lowest order asymmetry can be written as:

$$A_{\mathrm{FB}}(s) = \frac{3\sqrt{2}\pi\alpha}{G_\mu m_{\mathrm{Z}}^2 g_{\mathrm{A}}^{\mathrm{e}}g_{\mathrm{A}}^{\tau}}\left(1-\frac{m_{\mathrm{Z}}^2}{s}\right)+\frac{3g_{\mathrm{V}}^{\mathrm{e}}g_{\mathrm{V}}^{\tau}}{g_{\mathrm{A}}^{\mathrm{e}}g_{\mathrm{A}}^{\tau}} \tag{1.17}$$

As can be seen in the above approximation, the contribution of g_{V} to the asymmetry does not depend on the center of mass energy but adds a small constant term, whereas both the constant and the s-dependent part of the asymmetry depend on g_{A}.

1.4 Polarization asymmetry

For completeness some relations regarding the tau polarization asymmetry will also be presented here. The tau polarization asymmetry is defined as:

$$A_{\mathrm{pol}}^{\tau} = \frac{\sigma(h_\tau=+1)-\sigma(h_\tau=-1)}{\sigma(h_\tau=+1)+\sigma(h_\tau=-1)} \tag{1.18}$$

with h_τ the helicity of the tau, defined to be $h_\tau = +1$ when the momentum and the spin direction of the tau are parallel and $h_\tau = -1$ if they are anti-parallel and σ is the tau pair cross section for either of the spin states. On the Z^0 resonance one finds [11]:

$$A_{\mathrm{pol}}^{\tau}(s=m_{\mathrm{Z}}^2) \simeq \frac{-2g_{\mathrm{V}}^{\tau}g_{\mathrm{A}}^{\tau}}{(g_{\mathrm{V}}^{\tau})^2+(g_{\mathrm{A}}^{\tau})^2} \equiv \mathcal{P}_\tau \tag{1.19}$$

Using equation (1.4) and $g_{\mathrm{V}}^2 \ll g_{\mathrm{A}}^2$ this can be approximated by:

$$\mathcal{P}_\tau \simeq \frac{-2g_{\mathrm{V}}^{\tau}}{g_{\mathrm{A}}^{\tau}} = -2(1-4\sin^2\theta_{\mathrm{W}}) \tag{1.20}$$

A measurement of the tau polarization $\mathcal{P}_\tau$ thus determines the relative sign of g_{V}^{τ} and g_{A}^{τ}. Only the weak decays of the short lived tau lepton offer the possibility of measuring the polarization of leptons produced in Z^0 decays.

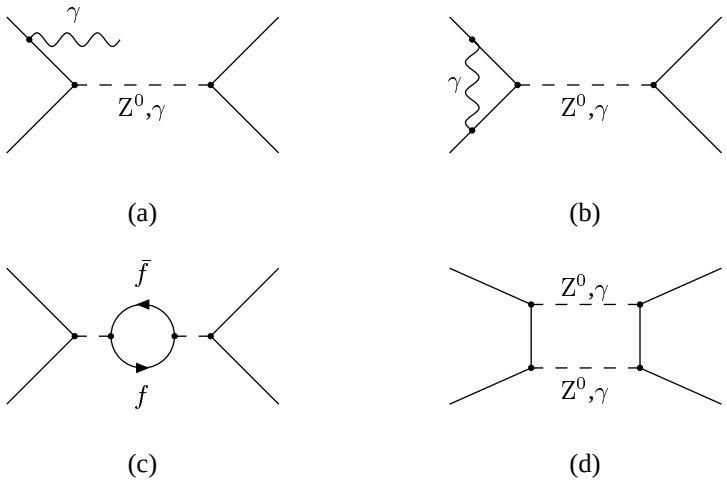

Figure 1.3 Examples of Feynman diagrams for radiative corrections: a) real photon initial state bremsstrahlung; b) virtual photon vertex correction; c) virtual fermion propagator correction; d) box diagram.

1.5 Electroweak radiative corrections

The formulae presented in the previous sections are all lowest order or so-called Born approximations. In this section electroweak radiative corrections to the Born level calculations will be treated.

The one-loop corrections to the process $\mathrm{e}^+\mathrm{e}^- \rightarrow \tau^+\tau^-$ can be subdivided into two subclasses [8]:

- QED corrections, consisting of the Born diagrams with an extra photon added. These can be either a real initial or final state bremsstrahlung photon, or a virtual photon loop.
- Weak corrections, collecting all other one-loop diagrams. They are corrections to the vector boson propagators (γ, Z^0) and corrections from vertex and box diagrams that are not virtual photon corrections.

Examples of Feynman diagrams for radiative corrections are shown in figure 1.3.

At $\sqrt{s}$ values near the peak of the Z^0 resonance, the initial state QED corrections contribute by far the largest effect, reducing the lowest order cross section by ∼30% at the peak. They are incorporated by convoluting the cross section σ_{W} with a radiator function $G(z)$:

$$\sigma(s) = \int_{4m_\tau^2/s}^{1} \mathrm{d}z \sigma_{\mathrm{W}}(s') G(z) \tag{1.21}$$

where σ_{W} is the improved Born cross section, which incorporates the radiative corrections not connected with initial state radiation, as discussed below, and $s' = sz$ is the square of the invariant mass of the produced fermion pair.

The weak corrections are small compared to the QED corrections. The corrections to the propagator, or self-energy corrections, are independent of the initial and final state fermions. These loop corrections involve all particles, including contributions of the top quark and the Higgs boson, and therefore depend also on m_{t} and m_{H}. The vertex corrections do depend on the initial and final fermion species. For electrons, muons and taus, the effects can be expressed in terms of s-dependent vector and axial vector couplings $\bar{g}_{\mathrm{V}}$ and $\bar{g}_{\mathrm{A}}$ (eqs. (1.24) and (1.25)). The one-loop box diagrams with two gauge boson exchange are non-resonant near the Z^0 peak (the box diagrams where at least one boson is a photon are included in the aforementioned QED corrections). The contribution of box diagrams at energies close to the Z^0 resonance is therefore negligibly small.

The remaining radiative corrections are incorporated by absorbing them into the following parameters, which must now be interpreted as effective parameters [8]:

$$\alpha \rightarrow \alpha(s) = \frac{\alpha}{1 - \Delta\alpha(s)} \tag{1.22}$$

$$\Gamma_{\mathrm{Z}} \rightarrow \Gamma_{\mathrm{Z}}(s) = \frac{s}{m_{\mathrm{Z}}^2}\Gamma_{\mathrm{Z}} \tag{1.23}$$

$$g_{\mathrm{V}}^f \rightarrow \bar{g}_{\mathrm{V}}^f = \sqrt{\bar{\rho}}(I_3^f - 2Q_f \sin^2\bar{\theta}_{\mathrm{W}}) \tag{1.24}$$

$$g_{\mathrm{A}}^f \rightarrow \bar{g}_{\mathrm{A}}^f = \sqrt{\bar{\rho}} I_3^f \tag{1.25}$$

$$\sin^2\theta_{\mathrm{W}} \rightarrow \sin^2\bar{\theta}_{\mathrm{W}} \simeq \sin^2\theta_{\mathrm{W}} + \cos^2\theta_{\mathrm{W}}\Delta\bar{\rho} \tag{1.26}$$

$$\rho \rightarrow \bar{\rho} = 1 + \Delta\bar{\rho} \tag{1.27}$$

The parameter ρ is the ratio of the neutral and charged current coupling constants and is unity in the Standard Model at Born level. The corrections to the photon propagator cause the running of the electromagnetic fine structure constant α and corrections to the Z^0 propagator change its width, Γ_{Z}. In using the above substitutions, the Born level formulae are still valid, but now with effective parameters, yielding the so-called improved Born approximation, which thus includes the weak corrections. The factor $\Delta\bar{\rho}$ is sensitive to the top mass through the approximate relation [8]:

$$\Delta\bar{\rho} \simeq \frac{3\sqrt{2}G_\mu}{16\pi^2} m_{\mathrm{t}}^2 \tag{1.28}$$

Figure 1.4 shows the effect of the full radiative corrections to the tau pair cross section, compared to the lowest order Born approximation. On the Z^0 peak the corrections are largest. In figure 1.5 the effect of the full radiative corrections to the charge asymmetry for tau pairs is compared to the lowest order Born approximation. The corrections are largest above the Z^0 peak. The corrected curves were calculated with the program ZFITTER (see [12] and chapter 6)

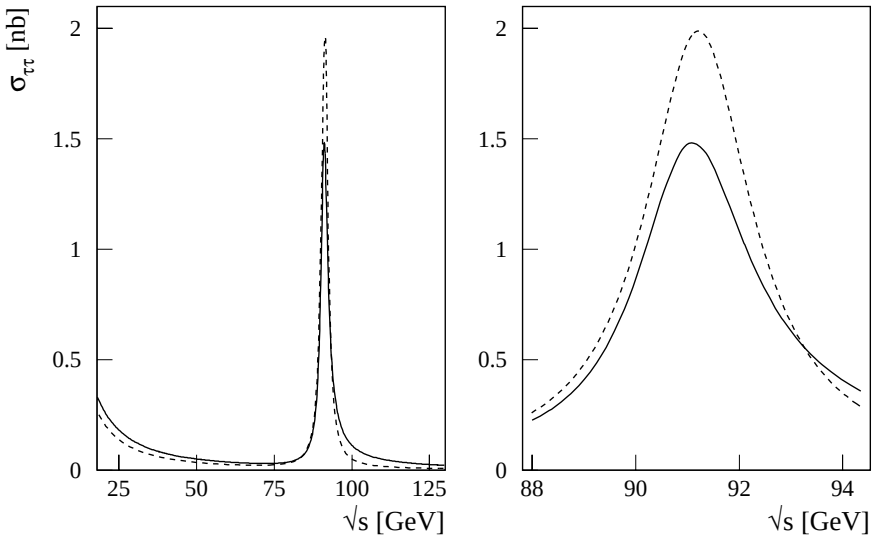

Figure 1.4 The tau pair cross section as function of $\sqrt{s}$ using the lowest order Born approximation (dashed line) compared to the cross section including the radiative corrections (solid line).

using the values $m_{\mathrm{Z}} = 91.195$ GeV, $m_{\mathrm{t}} = 140$ GeV, $m_{\mathrm{H}} = 300$ GeV and $\alpha_{\mathrm{s}} = 0.120$. The values of m_{Z}, Γ_{Z}, $\bar{g}_{\mathrm{A}}$ and $\bar{g}_{\mathrm{V}}$, or $\sin^2\theta_{\mathrm{W}}$ and $\bar{\rho}$ can be extracted from the tau pair measurements corresponding to these curves. They can be compared to the values obtained with other Z^0 decay channels. Since the data agree very well with the predictions, the measurements of the different decay channels can be combined to obtain high precision results. The measurement of the tau pair cross section and of the forward-backward charge asymmetry as function of $\sqrt{s}$ will be treated in chapter 4 and 5. In the last chapter of this thesis, the theoretical curves are fit to the experimental data.

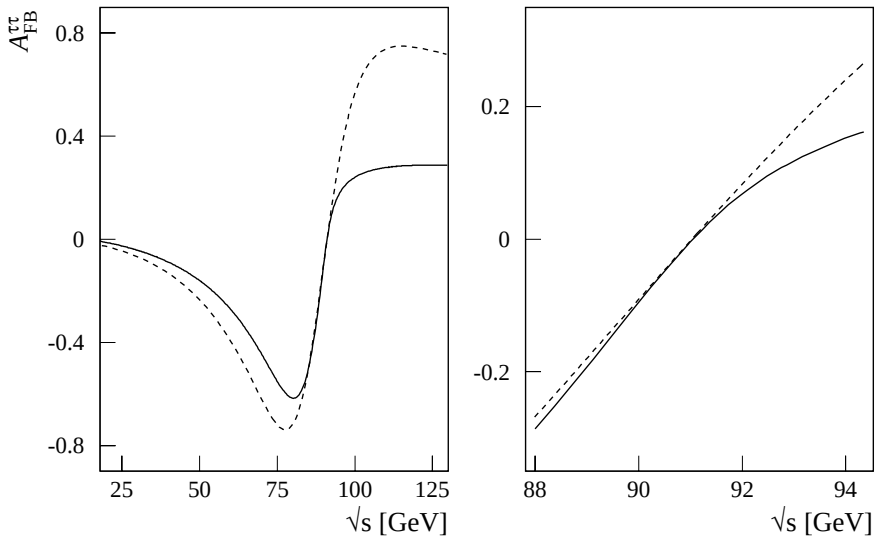

Figure 1.5 The charge asymmetry A_{FB} for tau pairs as a function of $\sqrt{s}$ in lowest order Born approximation (dashed line) compared to the asymmetry including the radiative corrections (solid line).

Chapter 2

The experimental setup

The data used for the analysis described in this thesis were collected with the L3 detector at LEP (Large Electron Positron collider) at CERN. This chapter briefly describes the collider and in much more detail the L3 detector components. The last part of the chapter describes the trigger and treats the basic event reconstruction.

2.1 LEP

Since 1989 the Large Electron-Positron collider (LEP) is in operation at CERN near Geneva on the Swiss-French border. LEP has the form of a ring, located in an underground tunnel with a circumference of 26.7 kilometers and a diameter of 3.8 meters and excavated at between 50 and 170 meters below the surface.

The ring consists of eight curved sections, each 2.8 km long, linked by eight straight sections of 0.5 km length. In the curved sections the particles are guided by about 3400 dipole magnets and the beam is focused by over 800 quadrupole and about 500 sextupole magnets. In the straight sections the particles are accelerated by 128 radio frequency accelerating cavities.

The beam pipe, a water-cooled vacuum chamber, is located in the magnet gaps. Inside the beam pipe the electrons and positrons circulate in opposite directions and they collide at four equidistant positions around the ring, the so-called interaction points.

The positrons are produced by bombarding a target with electrons which have been accelerated to 200 MeV by the first of two LEP Injector Lineacs (LIL). Both electrons and positrons are further accelerated to 600 MeV by the second LIL and are stored in bunches in the Electron Positron Accumulator (EPA). When the required number of particles has been reached, they are transferred to the Proton Synchrotron (PS) for acceleration up to 3.5 GeV and then transferred to the Super Proton Synchrotron (SPS) for acceleration to 22 GeV. At this energy electrons and positrons will be injected into the LEP ring, each in four bunches, with a length of 25 mm, equally spaced around the ring. The RF-cavities accelerate the particles up to about 50 GeV. A

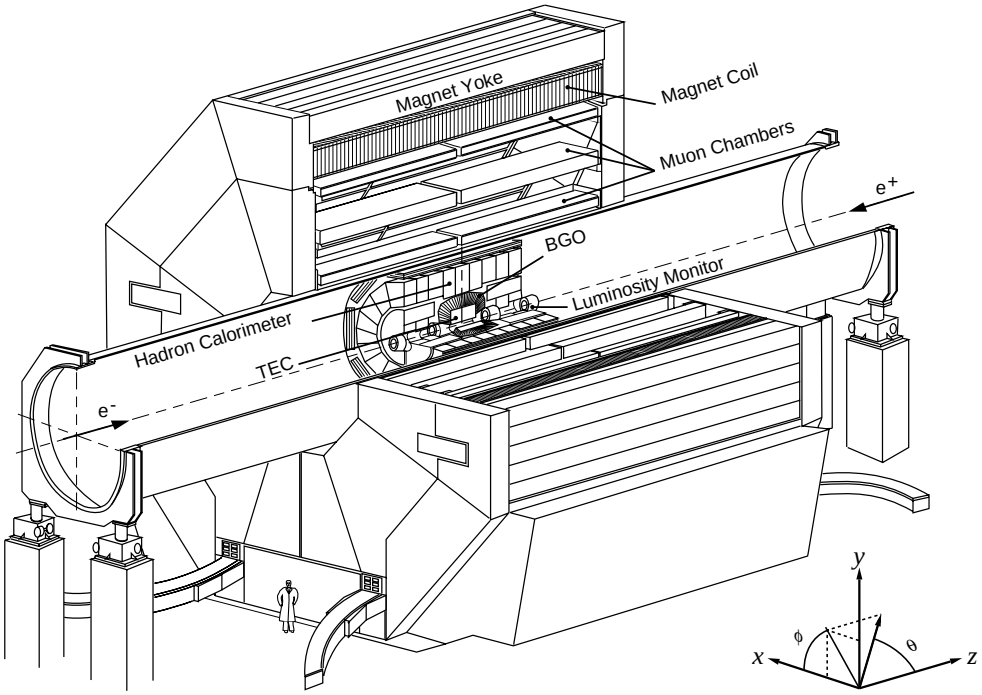

Figure 2.1 Perspective view of the L3 detector.

detailed description of the LEP accelerator and injection chain can be found in the LEP design reports [13, 14].

At the four interaction-points around the LEP ring, detectors have been build: L3 [15], ALEPH [16], OPAL [17] and DELPHI [18]. The next part of this chapter will describe the L3 detector in more detail.

2.2 The L3 detector

The L3 detector set-up is shown in figure 2.1. From the inside out the main components of the L3 detector are:

- Central tracking detector, measuring charged particle tracks;
- Electromagnetic calorimeter, measuring electron and photon energies;
- Hadronic calorimeter, measuring hadron energies;

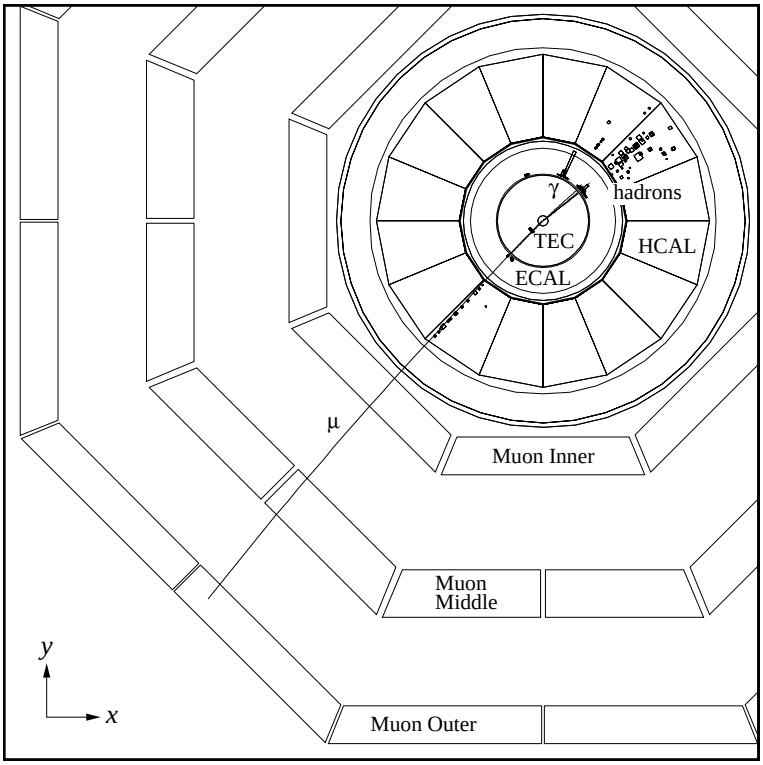

Figure 2.2 Front view of a tau event in the L3 detector. The different sub detectors are indicated.

- Muon spectrometer, measuring muon tracks.

The whole detector is housed in a solenoidal magnet with a magnetic field of 0.5 T. The global L3 coordinate system is also indicated together with the definition of the polar angle θ and azimuth ϕ. Figure 2.2 shows an event as seen by the L3 detector. This picture and all subsequent event display pictures in this thesis are made with the L3 scan program. For details about the L3 scan program see ref. [19]. The event in figure 2.2 originates from the reaction $\mathrm{e^+e^-} \rightarrow \tau^+\tau^-\gamma$, where the negative tau subsequently decays into a muon ($\tau^- \rightarrow \mu^-\bar{\nu}_\mu\nu_\tau$) and the positive tau into three charged hadrons ($\tau^+ \rightarrow \mathrm{hadrons}\ \bar{\nu}_\tau$). The produced neutrinos escape the detector unseen. The charged tracks are measured in the central tracking chamber (TEC). The photon is measured only in the electromagnetic calorimeter (ECAL), which also gives a signal for the muon and the hadrons. The hadrons are further detected in the hadron calorimeter (HCAL). The muon gives a minimum ionization signal in both the ECAL and the

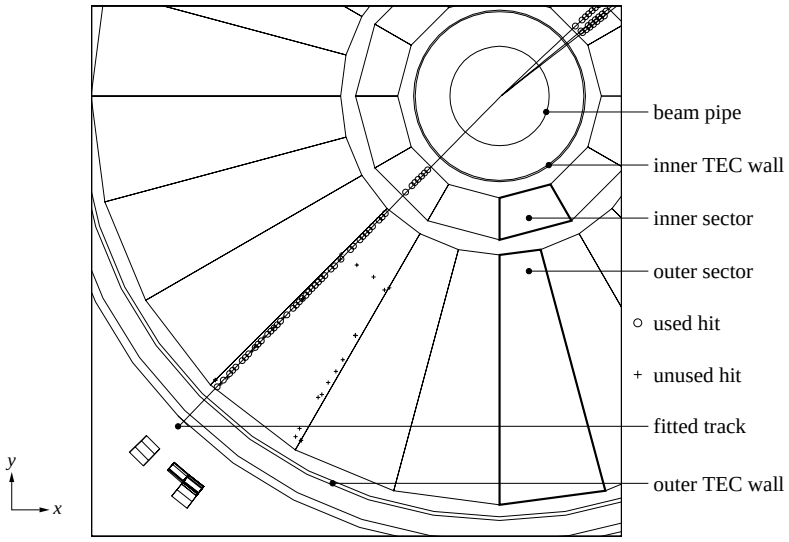

Figure 2.3 A muon track as seen by the inner tracking chamber. This figure depicts a detail of the event previously shown in figure 2.2.

HCAL. Outside the calorimeters, the momentum of the muon is accurately measured by the three layers of the muon spectrometer (MUCH).

In the following sections a description is given of the detector response to this particular event, showing the various aspects of the L3 detector and of the reconstruction of tracks and clusters.

2.3 The central tracking detector

The L3 central tracking detector is a time expansion chamber (TEC). This is a drift chamber with a low drift field region separated by a grid wire plane from a high field amplification region. The TEC is about 1 m long and has a radius of 50 cm. It is designed to accurately measure location and direction of charged particle tracks and to determine the charge and momentum for particles up to 50 GeV. For the details about this detector we refer to ref. [20, 21].

The TEC has 12 inner sectors with 8 readout anode wires and 24 outer sectors with 54 readout anode wires. The anode wires run through the middle of each sector and the electrons, created by ionization along the path of the charged particles, drift towards them.

In order to be able to tell from which side of the anode wire plane the electrons came, each inner sector spans two outer sectors, thereby resolving the ambiguity. Additionally, groups of five wires in the grid wire plane are read out on either side of the anode plane. By comparing

the induced signals on these wires, the left-right ambiguity for the corresponding anode wires can be resolved.

The inner and outer sectors are indicated in figure 2.3, which further shows in detail the TEC track belonging to the muon from the τ^- decay. The small circles represent signals on the anode wire (hits) that were used in the track fit and the small crosses show the hits that were not used in the fit. Most of the unused hits are at the position of the mirror track that has no corresponding hits in the inner sector.

The TEC tracks that are used in the analysis described in this thesis must satisfy the following conditions:

1. the track fit uses at least 30 hits out of the maximum 62;
2. the track span, i.e. the number of wires between the inner and outermost hit on the track, has to be greater than 45;
3. the distance of closest approach (DCA) to the event vertex, in the plane perpendicular to the beam, has to be less than 10 mm.

The first and second criterion remove misidentified tracks, where a small number of hits mimic a track. The last criterion removes tracks that do not originate from the event vertex, for instance real tracks produced by back scattering in the BGO calorimeter.

2.4 The electromagnetic calorimeter

The electromagnetic calorimeter consists of about 11,000 bismuth germanium oxide (BGO) crystals, each in the form of a truncated pyramid whose axis is radial from the interaction region. The barrel region contains 7,680 crystals and covers the polar angular region of $42^\circ < \theta < 138^\circ$. Each of the endcap calorimeters contains 1,536 crystals and extends the angular coverage to 12° and 168°, in forward and backward direction respectively. The endcap BGO calorimeter was installed after the 1990 run.

The crystals measure 2×2 cm^2 at the inner face and about 3×3 cm^2 at the outer face. The length of the crystals is 24 cm, corresponding to 21.4 radiation lengths and 1.1 nuclear interaction lengths. The energy resolution of the ECAL, $\Delta E/E$, is less than 2% for electrons and photons with an energy above 1.5 GeV [9].

Figure 2.4 shows the side view of the electromagnetic calorimeter and the response to the tau event. The thin lines indicate the position and size of the crystals. The thick outlined rectangles represent all crystals with an energy deposit above 50 MeV. For these crystals, the size of the rectangles in the figure is proportional to the energy deposit in the crystal.

The cluster in the lower part of the calorimeter is caused by the passing muon. A minimum ionization track from a muon deposits on average about 250 MeV in the ECAL, as can be seen from figure 2.5. This plot shows the energy loss in the electromagnetic calorimeter, for isolated muons, taken from the data.

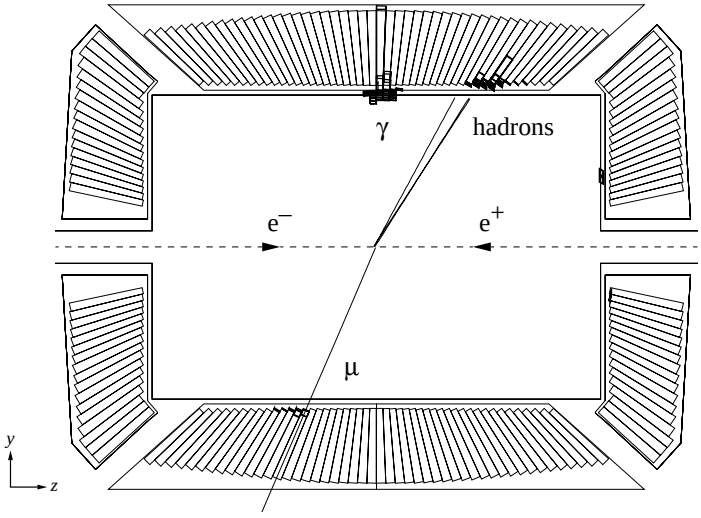

Figure 2.4 A tau event as seen in the electromagnetic calorimeter. This figure depicts a detail of the event previously shown in figure 2.2.

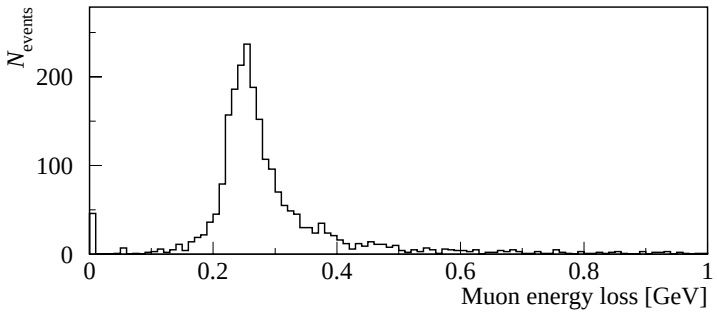

Figure 2.5 Energy loss in the BGO electromagnetic calorimeter for isolated muons, taken from the data.

The signal from the photon in the upper part of the detector shows the response of the calorimeter to an electromagnetic shower in the BGO. The cluster next to it originates from a hadronic shower. Not only does the hadronic shower extend into the hadron calorimeter, also the shape of the cluster in the ECAL is different for an electromagnetic and a hadronic shower. In general, an electromagnetic shower is sharply peaked and a hadronic shower is broad and

extends to more crystals. This difference is used in the off-line analysis to separate for example electrons from charged pions.

A detailed description about the electromagnetic calorimeter can be found in [22].

2.5 The scintillation counters

The scintillation counters are situated between the electromagnetic calorimeter and the hadron calorimeter. There are 30 counters in the barrel part of the detector. Because of the rails supporting the ECAL, the azimuthal coverage is 93%. Both sides of the counters are read out by a photo multiplier. By measuring the time difference between the signals read out by the photo multipliers on either side of the scintillator, the position of the hit along the beam direction can be determined.

The scintillation counters are used for triggering purposes, and provide an effective means for rejecting cosmic ray events. The time resolution is better than 0.5 ns while for example, the time difference between opposite scintillation counters is about 6 ns for a cosmic muon passing through the center of the detector and zero for a dimuon event produced in an $\mathrm{e}^+\mathrm{e}^-$ interaction. The position of the scintillators is indicated in figure 2.6.

2.6 The hadron calorimeter

The hadron calorimeter (HCAL) is designed to absorb all but the non-showering particles and measure the amount and position of the energy deposited. It consists of two parts: the barrel part, covering the central region ($35^\circ < \theta < 145^\circ$) and the endcap region, covering the forward and backward regions ($5.5^\circ < \theta < 35^\circ$ and $145^\circ < \theta < 174.5^\circ$). Both the barrel and the endcap calorimeters fully cover the azimuthal range. In the barrel part the calorimeter is segmented in nine rings, each consisting of 16 modules. The modules in the inner three rings are longer than those in the outer rings. The endcap hadron calorimeter consists of three rings each. The long barrel modules contain about 3.5 nuclear absorption lengths of material in the radial direction. The material of all detectors inside the support tube and the support tube itself corresponds to a total of about 6 nuclear absorption lengths, fairly independent of the polar angle [15].

The hadron calorimeter is a fine sampling calorimeter made of a sandwich of depleted uranium absorbers and proportional wire chambers. The barrel modules contain between 56 and 59 uranium plates. The wire chambers of consecutive layers are perpendicular to each other, thereby measuring the coordinates in both ϕ and z direction.

Figure 2.6 shows a side view of the tau event in the detector. The hadron calorimeter barrel and endcap regions are indicated. The energy deposited by the hadrons produced in the tau decay is measured both in the ECAL and in the HCAL. The photon is completely absorbed in the ECAL and the muon on the opposite side leaves a minimum ionization track in the HCAL before entering the muon chambers.

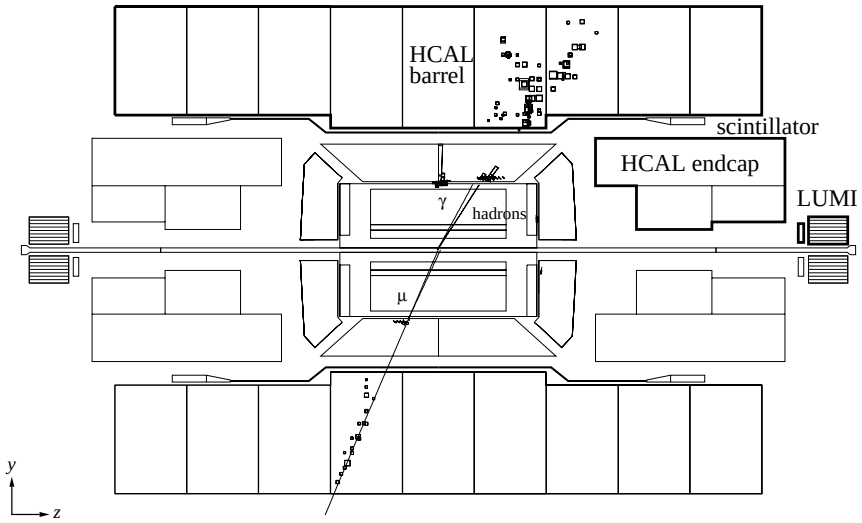

Figure 2.6 A side view of the tau event previously shown in figure 2.2. The black outlined regions show the barrel and endcap parts of the hadron calorimeter, and of the luminosity monitor. The photon is stopped in the electromagnetic calorimeter, the hadrons in the hadron calorimeter, and the muon will enter the muon spectrometer.

2.7 The muon filter

The muon filter is mounted on the inside wall of the support tube, outside the HCAL and adds about one absorption length to the hadron calorimeter. It consists of eight identical octants, each made of six brass absorber plates, interleaved with five layers of proportional chambers. The wires of the proportional chambers run in the direction along the beam, and measure the coordinate in the r-ϕ plane.

2.8 The muon detector

The muon spectrometer consists of drift chambers mounted on two Ferris wheels, each having eight independent octants. Each octant comprises five muon chambers (momentum measuring chambers or P-chambers), arranged in three layers: one inner chamber (Muon Inner, MI), two middle chambers (MM) and two outer chambers (MO). The three layers are about 1.5 m apart and measure the track coordinates in the bending plane.

Figure 2.7 shows a front view of one of the octants and a reconstructed muon track. The different cells inside the muon chambers are indicated. The boundaries of the cells are

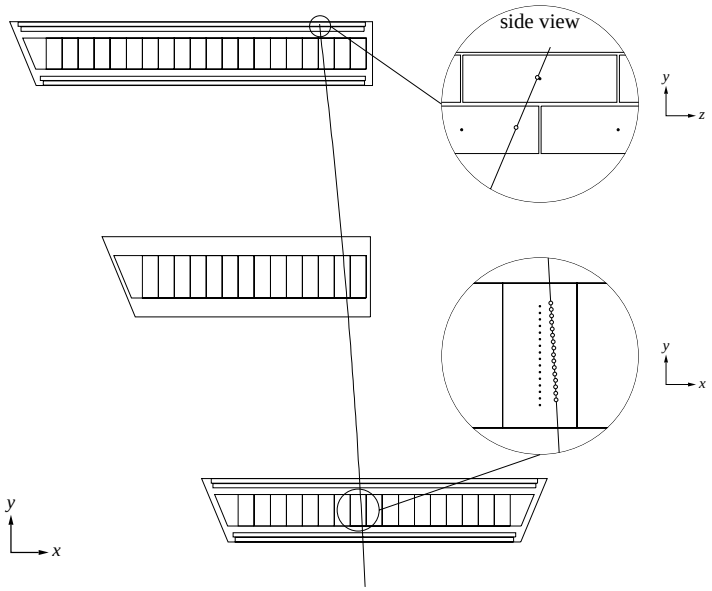

Figure 2.7 A front view of the muon from the tau decay as measured in the muon spectrometer. The blow-up views show the reconstructed hits that make up the track segments, together with the anode wires in the P-chambers (bottom) and in the Z-chambers (top). Note that the blow-up view of the Z-chamber is a side view.

determined by the position of the cathode wire planes. The anode wires or sense wires run through the middle of each cell, as can be seen from the blow-up view of one of the MI cells. The open circles represent the position of the muon track segment, as measured from the drift time corresponding to the hits on the sense wires. The dots indicate the positions of the sense wires. Since the direction of the drifting electrons is not known, the track segment might just as well have been on the other side of the wire plane (unless the track intersects with a cathode wire plane). However, by combining information from the other chamber layers, or even from other sub detectors, remaining ambiguities can be resolved. See [23] for details about track finding in the muon chambers.

In addition to the P-chambers, the top and bottom covers of the MI and MO chambers are also drift chambers, and measure the z-coordinate along the beam (Z-chambers). The Z-chambers consist of two layers of drift cells offset by one half cell with respect to each other to resolve left-right ambiguities. The chamber resolution is typically 500 μm. Figure 2.7 also shows a blow-up view of the muon track going through the Z-chambers on top of an MO chamber. Note that this is the side-view, as the wires in the Z-chamber run perpendicular to the wires in the P-chambers. Again, the dots indicate the positions of the wires and the open circles indicate the hits.

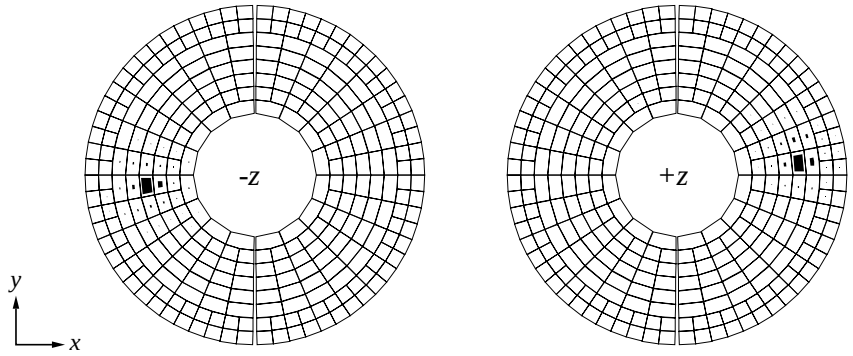

Figure 2.8 A Bhabha event as seen in the calorimeters of the luminosity monitor. The size of each dark box is proportional to the energy deposit in the corresponding crystal.

2.9 The luminosity monitor

The definition of the time integrated luminosity $\mathcal{L}$ is given by $\mathcal{L} = N/\sigma$, where N is the number of detected events, corrected for acceptance and background, and σ the cross section for a particular reaction.

In order to determine $\mathcal{L}$ we use events created through Bhabha scattering ($\mathrm{e^+e^-} \rightarrow \mathrm{e^+e^-}(\gamma)$). At small scattering angles, this reaction has a cross section, which can be precisely calculated within QED and which is almost independent of the weak interaction parameters. For details about the luminosity determination see [24].

The luminosity monitor (LUMI) is composed of two electromagnetic calorimeters, situated symmetrically on either side of the interaction point at about 2.6 m from the interaction point (see figure 2.6). The polar angular range effectively covered by the luminosity monitor is $31 < \theta < 62$ mrad, corresponding to a Bhabha cross section of 100 nb.

Figure 2.8 shows a typical Bhabha event in the luminosity monitor calorimeter. Adjacent crystals with more than 250 MeV of deposited energy are joined into clusters. The θ and ϕ impact coordinates and the energy of the incident particle, necessary for a precise luminosity measurement, are determined from a fit to the shower shape.

2.10 The trigger

The purpose of the trigger is to decide after each beam crossing whether an $\mathrm{e^+e^-}$ interaction took place and if so, whether the event should be recorded. In this decision, extreme care has to be taken: an event that has not been triggered will be lost forever. The triggering function is performed at three levels of increasing complexity, resulting in a tape writing rate of a few Hz at a beam crossing rate of 45 kHz.

The level-1 trigger

The level-1 trigger analyzes the trigger data as produced by each sub detector and decides within 22 μs, i.e. before the next beam crossing, whether or not to accept the event. On a negative decision all electronics are cleared and ready before the next beam crossing. The positive decisions however will introduce dead time, since they start the digitization and storage of detector data. At a typical rate of less than 8 Hz this results in a dead time of less than 5%. The level-1 trigger is the logical OR of trigger conditions from different sources: the energy trigger, the muon trigger, the track trigger, the scintillator trigger and the luminosity trigger:

The energy trigger selects events which deposit more than a few GeV in the ECAL and the HCAL. These events include Z^0 decays into e^+e^-, $\tau^+\tau^-$, $\nu\bar{\nu}\gamma$ (single photon) and hadronic final states. The trigger requires at least 8 GeV in the ECAL barrel or at least 15 GeV in the ECAL and HCAL barrels or at least 25 GeV in all calorimetric detectors. If a cluster in θ and ϕ is found with an energy exceeding 6 GeV, the event is also accepted and if this cluster coincides with a track from the charged track trigger, this threshold is lowered to 2.5 GeV. An event with only a single isolated electromagnetic cluster of more than 1 GeV (single photon) is also accepted. The typical rate of this trigger is 1–2 Hz.

The muon trigger requires tracks in the muon chambers with a transverse momentum exceeding 1 GeV$/c$. The single muon trigger requires one track measured in at least 2 out of 3 P-chamber layers and 3 out of 4 Z-chambers in the same octant. The dimuon trigger requires two tracks: one as measured in at least 2 out of 3 P-chamber layers and one of the MI Z-chamber layers; the other measured in at least two out of 3 P-chamber layers in the five opposite chambers. In addition at least one scintillator should have been hit in time. The combined trigger rate of the single and dimuon trigger is less than 1 Hz.

The charged track trigger requires at least two tracks in the central tracking chamber with a transverse momentum exceeding 150 MeV$/c$ separated by more than 120° in azimuth. Depending on the beam conditions, the TEC trigger rate varies from 1–4 Hz.

The scintillator trigger aims at selecting high multiplicity events and fires when at least 5 out of 30 scintillation counters are hit within 30 ns of the beam crossing and at least one pair of the hits is separated by more than 90° in azimuth. The typical rate of the scintillator trigger is 0.1 Hz.

The luminosity trigger requires more than 15 GeV deposited in both BGO calorimeters or at least 25 GeV in one and 5 GeV in the other or at least 30 GeV in either calorimeter. The latter condition is used as a check of the other two and is prescaled by a factor of 20. Also the first two conditions are prescaled, by a factor of two, as the accuracy of the luminosity measurement is not dominated by the statistical error. The trigger rate is typically 1.5 Hz.

Apart from the luminosity trigger, these triggers are highly redundant, in the sense that the e^+e^- interactions usually are triggered by two or more triggers. The efficiencies of these triggers for tau pair events are calculated in section 4.5.

The level-2 trigger

The function of the level-2 trigger is to reject background events that were accepted by the level-1 trigger. It mainly removes calorimeter triggers generated by electronics noise and beam-gas or beam-wall interactions as well as TEC triggers generated by synchrotron radiation. The second level trigger doesn't add any dead time and reduces the level-1 trigger rate by 20–30% to less than 6 Hz.

The level-3 trigger

The third level trigger uses the complete digital data of the event. Luminosity events and events triggered by more than one of the level-1 triggers pass unhindered. The event energies are recalculated and there are more stringent requirements on the scintillator coincidence with the muon trigger. The TEC tracks have to be associated with at least 100 MeV of energy in the calorimeters and have to fulfill quality and vertex requirements. The level-3 trigger reduces the trigger rate by 40–60% to a rate of 2–3 Hz.

2.11 Reconstruction

The signals in each sub detector, resulting from interactions of single particles or jets of particles with the detectors have to be combined and transformed into quantities that are directly related to the kinematics of the original e^+e^- reaction. The different objects to be distinguished are hadronic jets from quarks and gluons, single hadrons, electrons, photons and muons. The event reconstruction proceeds in two steps. Firstly the objects are reconstructed in each sub detector separately. Secondly, the information from the sub detectors is combined in a global event reconstruction, forming well separated objects (the so called ASJT's).

The first step identifies hits in the calorimeter, where a hit is a localized energy deposit above a certain threshold. Contiguous hits are combined into clusters. The clusters are characterized by their energy and longitudinal and transverse profile. Electromagnetic and hadronic clusters are distinguished. The direction of a cluster is defined as the vector sum of all the hits that make up the cluster, where the vector origin is the interaction vertex. Information about muons reconstructed in the muon chambers is added to the first step calorimeter reconstruction.

The global event reconstruction starts from the most energetic cluster, adding all clusters in a 30° cone around it. In an iterative process, an object axis is defined as the energy weighted vector sum of all included cluster vectors and a new 30° cone is defined about this axis. The iteration stops when no new clusters are added to the object after redefinition of its axis. The unused clusters are grouped in the same way to build new objects. A remaining low energy

cluster is added to the closest existing object if it is not separated by more than 20° from the closest cluster in that object. After the objects are reconstructed they are classified and different energy calibrations are applied. For a muon inside a jet, the momentum as measured in the muon chambers is used. For a single muon the momentum at the vertex, i.e. after back-tracking, is used. Electromagnetic calibration is used for isolated electrons (photons) or for an electromagnetic cluster in a hadronic jet. Different hadronic calibrations are used for low energy jets (single hadrons) and high energy jets.

For some more details about the jet finding algorithm and about hadron calorimetry see ref. [25].

Chapter 3

The L3 muon chamber alignment system

In this chapter the RASNIK alignment system will be discussed. This alignment system is used for the internal alignment of the wires in the muon chamber and for the alignment of the wire planes in different chambers in an octant. Section 3.1 treats the alignment requirements in order to achieve the design muon momentum resolution. The principle of operation of the RASNIK system and the calibration of the individual systems is discussed in section 3.2. The L3 muon chamber monitoring system which controls and monitors not only the muon chamber alignment, but also other items, such as the high voltage and the temperature is described in section 3.3. In section 3.4 the RASNIK hardware layout in the L3 muon chamber system is shown. Sections 3.5 and 3.6 treat the software implementation of the system.

3.1 Alignment requirements

The design value of the L3 muon spectrometer resolution is $\Delta p/p$ = 2% at p = 45 GeV$/c$. In the spectrometer, the sagitta S of a muon track in the 0.5 T magnetic field is only 3.7 mm at 45 GeV$/c$, so in order to measure the sagitta with a 2% resolution this sagitta should be known to an accuracy of better than 74 μm. The contributions of the different error sources to the sagitta measurement are discussed below.

Assuming a very conservative value for the single wire resolution of the L3 muon chambers of 200 μm [26], the position can be measured with an accuracy ε, when sampling the track with N wires:

$$\varepsilon = \frac{200}{\sqrt{N}}\ \mu\text{m} \tag{3.1}$$

The sagitta of a track in the L3 muon chamber system is defined as shown in figure 3.1. For

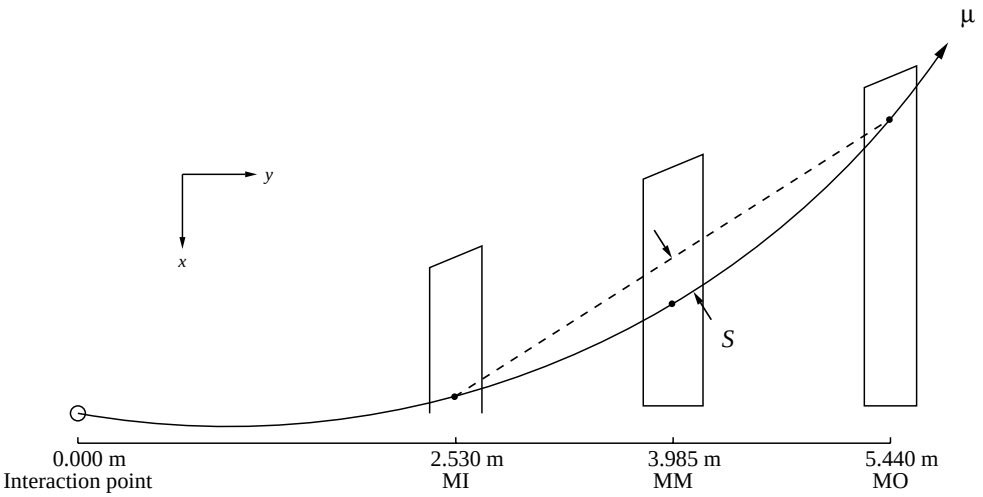

Figure 3.1 Definition of the sagitta S in the L3 muon chamber system.

high momentum tracks this can be well approximated by:

$$S_{\mathrm{ch}} = \frac{x_{\mathrm{MI}}}{2} + \frac{x_{\mathrm{MO}}}{2} - x_{\mathrm{MM}} \tag{3.2}$$

where the coordinate system is as indicated in the same figure. The intrinsic chamber resolution is therefore:

$$\Delta S_{\mathrm{ch}} = \sqrt{\left(\frac{\varepsilon_{\mathrm{MI}}}{2}\right)^2 + \left(\frac{\varepsilon_{\mathrm{MO}}}{2}\right)^2 + \varepsilon_{\mathrm{MM}}^2} \tag{3.3}$$

The number N of anode wires (sense wires) per plane is 16 for the MI and MO chambers and 24 for the MM chambers. Using equations (3.1) and (3.3) and including a 90% detection efficiency for each wire, a value of ΔS_{ch} = 57 μm is found.

Another source of error in the sagitta measurement comes from the multiple scattering of the muon in the chamber material ΔS_{ms}. This contribution has been estimated to be about 31 μm for a muon of 45 GeV/c [26].

The relative alignment of the wire planes inside the chambers and of the alignment of the wire planes inside an octant is a third source of error in measuring the sagitta. Adding the errors in quadrature, one finds that the error on the sagitta, due to alignment, ΔS_{al} must be less than 36 μm in order to reach the required momentum resolution, if no other error sources exist.

Contributions to the alignment error

An estimate of the accuracy requirements on the alignment of the wires in an octant will be made here. Each alignment system in an individual chamber layer (MI, MM and MO) measures the relative x position inside the chamber with an accuracy δ_x. The contribution to the error on the sagitta $\Delta S_{\mathrm{al},x}$ from the three layers is:

$$\Delta S_{\mathrm{al},x} = \sqrt{\left(\frac{\delta_{x,\mathrm{MI}}}{2}\right)^2 + \left(\frac{\delta_{x,\mathrm{MO}}}{2}\right)^2 + \delta_{x,\mathrm{MM}}^2} \tag{3.4}$$

The average ϕ angle of a muon track in an octant is 11.25°. Therefore, an uncertainty in the y measurement introduces an average shift of $\tan(11.25^\circ) \cdot \delta_y = 0.2 \cdot \delta_y$ in the x direction and hence a contribution to the uncertainty in the sagitta of:

$$\Delta S_{\mathrm{al},y} = 0.2 \cdot \sqrt{\frac{\delta_{y,\mathrm{MI}}^2 + 100^2}{4} + \frac{\delta_{y,\mathrm{MO}}^2 + 100^2}{4} + \delta_{y,\mathrm{MM}}^2} \tag{3.5}$$

The extra terms of 100 μm correspond to the accuracy of the relative positioning in y of the MI and MO chamber layers in the octant with respect to the middle layer MM [15].

The MM chamber layer has to be aligned in the x direction with respect to the inner and outer chamber layers as well. This requires an alignment system on either side of an octant, defining the octant center line at the interaction point side and at the magnet door side of an octant. The uncertainty δ_{v} on each of these measurements is directly related to the error on the sagitta:

$$\Delta S_{\mathrm{al,v}} = \sqrt{\left(\frac{\delta_{\mathrm{v}1}}{2}\right)^2 + \left(\frac{\delta_{\mathrm{v}2}}{2}\right)^2} = \frac{\delta_{\mathrm{v}}}{\sqrt{2}} \tag{3.6}$$

Adding the three contributions in quadrature, one finds an expression for the total error on the sagitta, due to alignment:

$$\Delta S_{\mathrm{al}} = \sqrt{(\Delta S_{\mathrm{al},x})^2 + (\Delta S_{\mathrm{al},y})^2 + (\Delta S_{\mathrm{al,v}})^2} \tag{3.7}$$

If ΔS_{al} has to be less than 36 μm (see previous section) and one assumes equal contributions from $\Delta S_{\mathrm{al},x}$, $\Delta S_{\mathrm{al},y}$ and $\Delta S_{\mathrm{al,v}}$, the following requirements for the individual alignments are obtained:

$$\begin{aligned} \delta_x &< 34\ \mu\mathrm{m} \\ \delta_y &< 124\ \mu\mathrm{m} \\ \delta_{\mathrm{v}} &< 29\ \mu\mathrm{m} \end{aligned} \tag{3.8}$$

The values for δ_x and δ_y specify the tolerance of the position of the middle of the wire. The average deviations are thus twice as small.

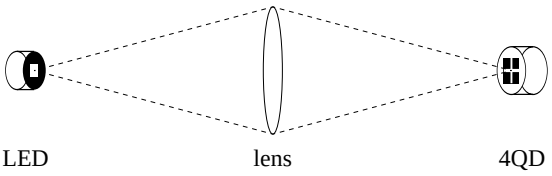

Figure 3.2 Schematic drawing of the RASNIK alignment system, showing the LED, the lens and the light sensitive four quadrant diode.

In order to meet these high accuracy requirements the so called RASNIK alignment system [27] is used. This alignment system will be described in the next section. A detailed description on the mechanical structure and the design tolerances of the muon chamber octants can be found in [26].

3.2 The RASNIK alignment system

The RASNIK system consists of a LED, a lens and a four quadrant light sensitive photodiode (4QD). A schematic drawing of such a system is shown in figure 3.2. The LED provides a homogeneous square light source, which is projected by the lens onto the 4QD. The 4QD measures the relative light intensity on each of the four quadrants. It is straightforward to calculate the position of the square LED image on the 4QD. Let h be the size of the sides of the LED, I_ℓ and I_r the intensities on the left and right two quadrants respectively. The position x of the LED's image on the 4QD is then given by:

$$x = \frac{I_r - I_\ell}{I_r + I_\ell}\frac{h}{2} \tag{3.9}$$

when the LED's image is completely on the 4QD and the size of the gaps between the quadrants can be neglected. Similarly the y position can be calculated using the intensities on the upper and lower two quadrants. In this way, the RASNIK system can be used as an active monitor of the position of the lens with respect to the positions of the LED and 4QD, as long as each quadrant receives at least some of the light.

Horizontal and vertical alignment systems

The alignment system that measures the x and y coordinates of the middle bridge inside the chambers is called the horizontal alignment system. There are three such systems inside each muon chamber, making a total of 240 horizontal alignment systems for the 16 octants with 5 chambers each. In order to measure the y position (perpendicular to the chamber) two alignment systems would suffice, but for redundancy reasons three are used. Figure 3.3 shows a schematic view of the horizontal alignment system inside the muon chamber. Each set of LED,

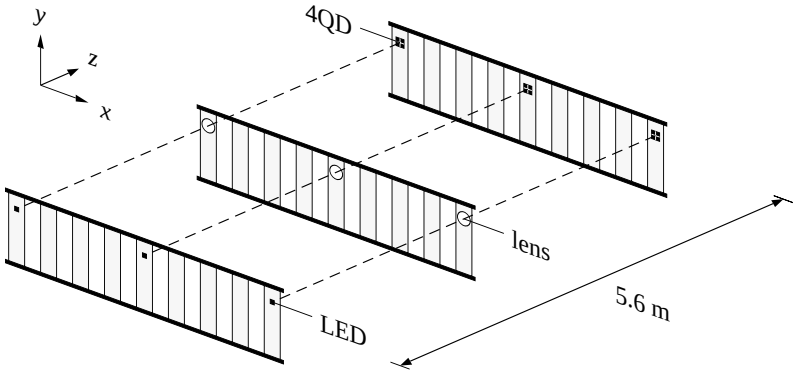

Figure 3.3 Schematic view of the RASNIK alignment systems inside a muon chamber. The bridges can be moved by actuators accessible from outside the chamber.

lens and 4QD has been calibrated before mounting on the bridges. The three bridges are put in position by moving the middle bridge using actuators accessible from outside the chambers.

The alignment system that measures the x coordinate of the MM chamber relative to the positions of the MI and MO chambers is called the vertical alignment system. For each octant, there are two vertical alignment systems. One on the magnet door side (MD) and one on the interaction point side (IP) of the octant. Both are double systems, with two LED's, two 4QD's and one lens. In case of failure of either a LED or 4QD the remaining working parts will still measure the x coordinate accurately.

A schematic view of the vertical alignment system can be seen in figure 3.4. The LED is mounted in a polycarbonate block positioned on the outside of the MI chambers. Inside the block is a conductive pin, accurately positioned relative to the LED. The end bridges of the MI chambers can be moved in such a way that one wire in the middle plane just makes electrical contact with the pin. In this way, the position of the wire planes is referenced to the position of the LED.

The lens and the 4QD are mounted in a structure having two pins, which go inside the MM and MO chambers respectively. The pins have a well defined length and accurately set the distance between the wire planes in the left and right MM and MO chambers. The lens and the 4QD are placed between the two pins, in the middle of the wire planes. The end bridges in the MM and MO chambers can be moved, just like the end bridges in the MI chamber, to just make contact with the pins. By moving the two middle chambers simultaneously inside the octant, the wire planes in the octant can be aligned. The position is monitored with the RASNIK system.

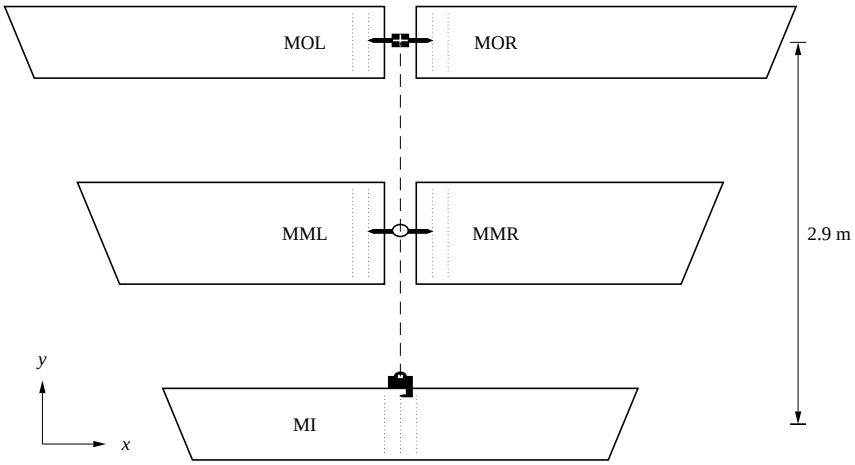

Figure 3.4 Schematic view of the RASNIK system aligning the wire planes inside the MM chambers relative to the inner and outer chambers.

Calibration accuracy

The calibration of each RASNIK system is done on a special alignment stand. This calibration stand, supporting the LED, the lens and the 4QD must first be aligned. This can be done by using the RASNIK system itself, when the LED, lens and 4QD are mounted on special supports with a well defined width. Gauge blocks made by industry with an accuracy better than 1 μm are used for these supports.

The RASNIK system is first placed on the calibration stand, and the position is measured. The special gauge block supports enable a second accurate measurement of the position after a rotation of the three parts over 180 degrees around the z-axis. Because of this rotation the LED's image moves by 4 times the displacement of the lens as is illustrated in figure 3.5. This figure schematically shows an aligned RASNIK system on the calibration stand before and after rotation. The gray part indicates the orientation of the alignment system. The stand itself is not well calibrated, as is indicated by the support being bent, and the position read out is twice the displacement at the lens position. After rotation, the spot moves to the opposite side on the 4QD and the position read out is -2 times the displacement at the lens position. Note that the coordinate system rotates along with the 4QD.

Secondly, the alignment system on the stand has to be calibrated. Figure 3.6 shows a RASNIK system on a flat calibration stand before and after rotation. Since a misalignment of any of the three components can be interpreted as a misalignment of the lens only, the system is shown with the lens displaced. The readout of the spot position on the 4QD is twice the displacement of the lens. In this case, the position does not change after rotation.

Figure 3.5 The effect of a displacement of the alignment stand at the lens position before and after rotation.

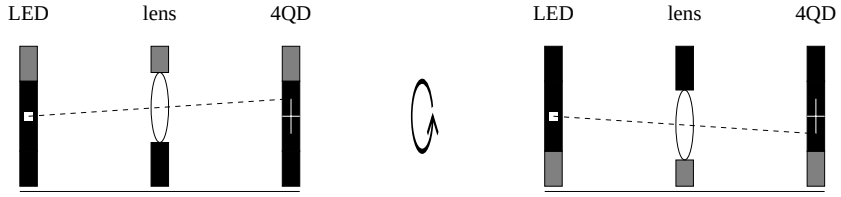

Figure 3.6 The effect of a displacement of the lens before and after rotation.

So in principle both the alignment error of the calibration stand and of the RASNIK system itself are known after one rotation: let x be the first position read out and let x' be the position after rotation. The displacement of the calibration stand at the lens position is then given by $(x - x')/4$ and the alignment error of the RASNIK system by $(x + x')/4$.

The accuracy of the calibration is shown in figure 3.7, which plots the alignment error for the individual systems before mounting in the chambers. The histograms show the resulting errors for the 275 horizontal alignment systems, measuring x and y, and for the 34 vertical alignment systems, measuring x, made at NIKHEF-H. The alignment error is defined as the displacement of the lens relative to the line connecting the LED and the 4QD. The r.m.s. calibration errors are 3.0 μm 7.0 μm and 1.7 μm for the x and y coordinates of the horizontal alignment system, and the average of the two x values of the vertical alignment system respectively. The positioning of the glass plates in the carbon fiber wire bridges can be done with an r.m.s. accuracy of 7.3 μm [28]. The positions of the components of the vertical alignment system relative to the wires are determined by moving the wire bridges and measuring whether or not the wire makes electrical contact with the conductive pin. This can be done with an accuracy of 2 μm.

From figure 3.7 one can see that the calibration accuracy from each individual system is already well below the required value of 34 μm for x, 124 μm for y and 29 μm for the vertical system (see section 3.1). As there are three independent horizontal alignment systems per chamber, the requirement on the horizontal alignment is even further reduced.

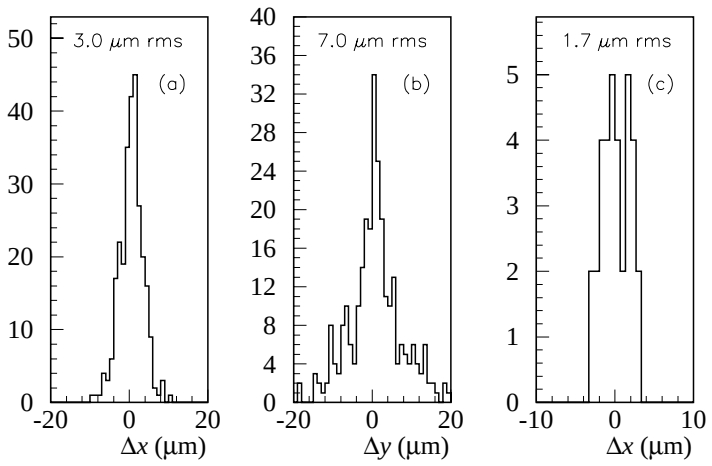

Figure 3.7 Alignment error for the horizontal alignment system measuring the x and y coordinate (a), (b) and for the vertical alignment system measuring the x coordinate (c) before mounting on the chambers.

Linearity

The range of the RASNIK system is determined by the dimensions of the LED and the 4QD. In the implementation used for the L3 muon chamber barrel, the size of the LED is $1700 \times 1700\ \mu\text{m}^2$ and the 4QD measures $2540 \times 2540\ \mu\text{m}^2$. At the lens position the maximum allowed range is therefore $\pm 425\ \mu$m. Figure 3.8 shows the position read out by the RASNIK system as function of true displacement. The linear behavior of the system allows the usage of the measurements to correct for the wire positions off-line. The deviations from the straight line are small, and are mainly due to the non homogeneity of the LED light source. In the range of $\pm 200\ \mu$m the deviations can be well approximated by a line with a slightly different slope. A slope correction has thus been applied in software, both a global correction for the horizontal alignment systems and an individual correction for the vertical alignment systems. Over the full range the true position of the lens can be calculated with an accuracy better than $20\ \mu$m [29]. However, since the wire planes in the muon chamber system have been positioned very accurately, the full range is never used. Typically, the systems are within $30\ \mu$m of the central position, and the deviations from linearity over this small range are negligible.

Stability

Figure 3.9 (top) shows the readout of the vertical alignment system of octant M_7. The data for both x values on the magnet door side have been plotted for the data taking period in 1990. The

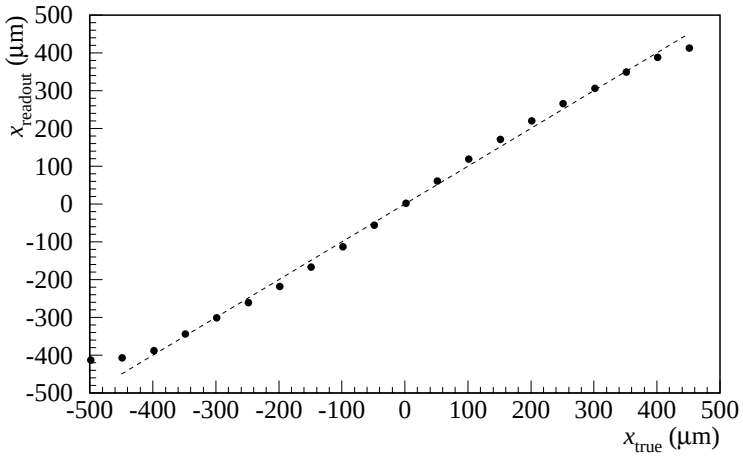

Figure 3.8 Displacement of the lens, measured with the RASNIK alignment system, as function of true displacement. The system shows a good linear behavior.

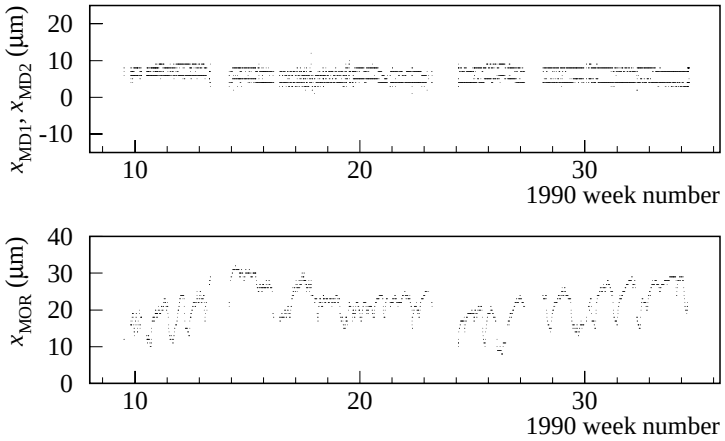

Figure 3.9 Readout of the two x values of the vertical alignment systems 16 and 17 in octant M_7 over the data taking period in 1990 (top) and of one horizontal alignment system in the right MO chamber of the same octant (bottom).

data show that the chambers in the octant hardly move over the half year period, and that the RASNIK system itself is also very stable. The lower plot of figure 3.9 shows the measurements

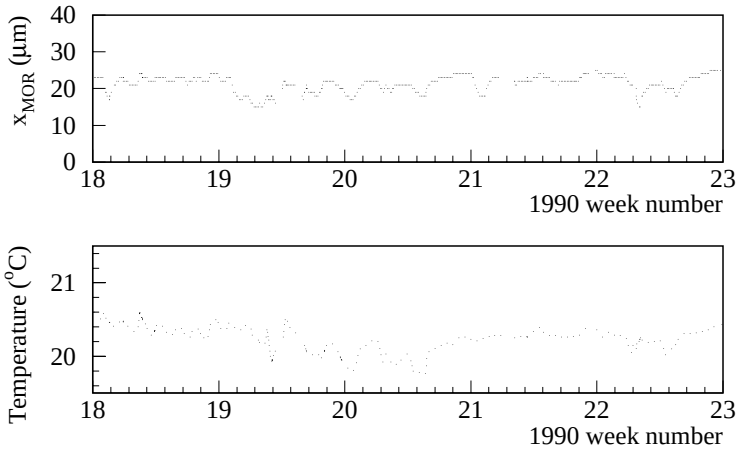

Figure 3.10 Readout of one of the horizontal alignment systems in the right MO chamber of octant M_7 over a 5 week period (top) and the readout for the temperature on the same chamber (bottom).

for one of the horizontal RASNIK systems in the right MO chamber in octant M_7 over the same period. The data presented in this plot show relatively large fluctuations compared to similar measurements in other chambers or octants. However, these movements are still only of order ± 10 μm and stay well within the allowed range of ± 425 μm. The measurements are fed into the database and are used by the off-line software to make time dependent corrections to the muon momentum measurements.

The movement of the wire bridges is correlated with the temperature in the chamber. One can see this correlation from figure 3.10, where again the readout for one of the horizontal alignment systems in octant M_7 (top) is plotted, but this time on a time scale of 5 weeks. The bottom plot of figure 3.10 shows the temperature readout over the same period, as measured by a sensor mounted on the right MO chamber.

Other octant alignment systems

The vertical RASNIK systems define a straight line at each end of an octant. These lines are not necessarily parallel. The octant torque is measured by a laser beacon system [30, 31]. This system consists of a rotating pentaprismatic mirror which makes a laser beam sweep out a plane. The position of the lines defined by the vertical RASNIK systems with respect to the plane is monitored by six position sensors. These sensors are attached directly to the three elements of each of the two vertical RASNIK systems in each octant. The laser beacon system can measure the angle between the two octant lines to better than 25 μrad, corresponding to an

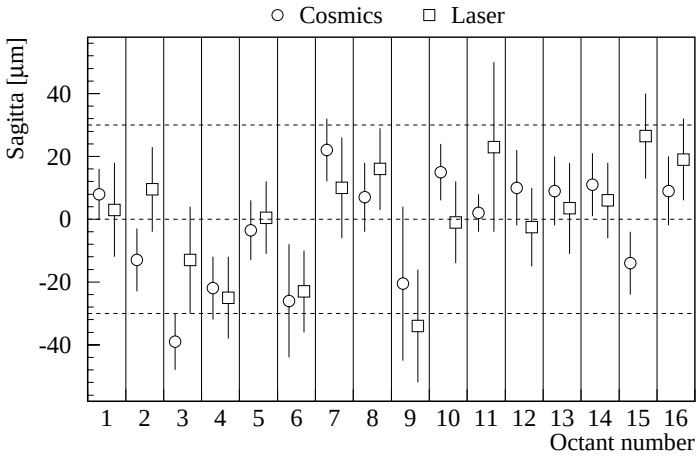

Figure 3.11 The sagitta measured with the UV laser (squares) and cosmic muons (circles) for each octant.

error in the sagitta of less than 10 μm.

The alignment has been verified with cosmic rays and with a UV laser system [32]. The UV laser system consists of an ionizing laser beam which can be directed through the muon chamber octant at different positions. The laser beam trajectories simulate infinite momentum muons and thus the sagitta of these tracks should be zero. In absence of the magnetic field, cosmic ray muons of high enough momentum define straight tracks through the octants. These tracks have been used to check the octant alignment. The result of the alignment verification with cosmic rays and UV laser is shown in figure 3.11. For cosmic rays and UV laser measurements the sagitta is calculated using the alignment monitors to determine the position of the relevant wires. The test shows that the alignment of the octant can be verified and controlled to within 30 μm, which is within the required 36 μm (see section 3.1).

3.3 The L3 muon chamber monitoring system

The L3 muon chamber monitoring system controls and monitors different parameters that vary slowly with time. The main monitor systems are:

- the high voltage system, controlling and monitoring the high voltage on the muon chamber wires [33];
- alignment monitoring of the wire positions inside the muon chambers, using RASNIK alignment systems;

- alignment monitoring of the torque of the muon chamber octants, using the laser beacon alignment system [34];
- temperature monitors probing the temperature at many positions in the muon chamber system;
- discriminator threshold control system, controlling the settings of the wire signal thresholds [33];
- t0cal, the t_0 calibration system [27];
- actuator motor control and readout, positioning the MM chambers in the octants;
- FASTBUS crate operating conditions monitor;
- UV-laser system for calibrating the muon chambers using the UV-laser ionization tracks.

These monitoring systems have been implemented in software running on a VME based OS9-68000 system. This is a multi-process, multi-tasking environment, which provides tools for communication and shared data between different processes. There are in total 10 VME crates, each equipped with a CPU board with a Motorola 68000 processor, a 4 Mb memory board and a 60 Mb hard disk. Each crate typically runs one or two monitoring tasks.

The crates are interconnected through an ethernet network, which also provides the connection to the outside world, e.g. the on-line VAX 8800 computer. Not only can people on shift communicate with the OS9 tasks through the VAX, but also the data generated by the monitoring tasks are transferred automatically to the VAX and to the on- and off-line databases.

All command communication to the different tasks is routed through the command processing program (`cp`). This process runs on every VME crate, and knows the current OS9 network configuration. It also knows on which VME crate the (parts of) different monitoring tasks run. It checks command integrity and user authorization and, if the command was found to be correct, sends it to the monitoring task running on the crate(s) involved. The tasks then send a status back to the command processor, which in turn notifies the user of the (successful) command completion.

It makes no difference to the task whether the command comes directly from the user-interface program running on VME or on the VAX. Some commands however should be given only from a terminal directly connected to the crate running the task. An example is the high voltage system, where remote tampering with the high voltage settings would be highly undesirable. The `cp` process ensures that those commands are carried out only if issued at an authorized terminal.

Systems that monitor slowly varying quantities like alignment, temperature and high voltage will notify the people on shift whenever the measured values exceed predefined limits. Some of these alarms can be sent from the monitoring task itself, while others are being generated by the general muon monitoring program running on a VAX station in the Control Room. For example, the temperature readout task will send an alarm (through the command processor)

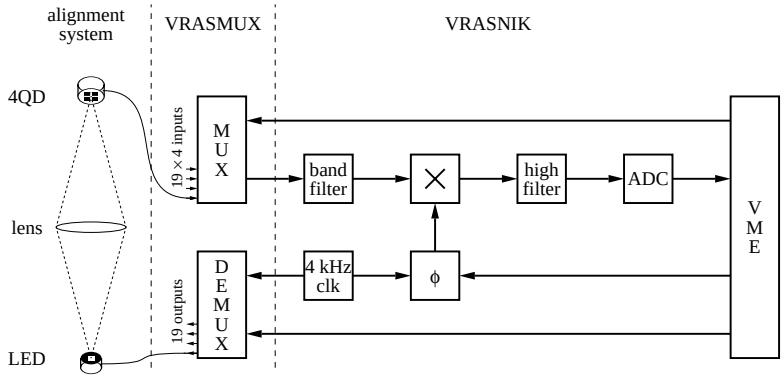

Figure 3.12 Principle of the multiplexing, modulating and demodulating electronics of the RASNIK alignment system.

to the general monitoring program when the temperature gets outside a predefined range. The person on shift will notice this and should then take immediate action. A less severe problem, like no new monitoring data arriving on the VAX, will be noted by the general program itself, which will then notify the people on shift. Since all data is being buffered locally on the VME system, the data will find their way to the VAX at some later time.

3.4 The RASNIK monitoring hardware

The RASNIK hardware can be grouped in three parts:

- The optical alignment system (LED, lens and 4QD);
- The multiplexer modules (VRASMUX);
- The controlling VME module (VRASNIK).

The principles of the alignment system itself have been discussed in detail in section 3.2.

Each octant comprises five chambers, with three RASNIK systems each. This makes 15 horizontal alignment systems. There are 2 double vertical systems, making a total of 19 RASNIK systems per octant.

Figure 3.12 shows the basic layout of the RASNIK electronics. The demultiplexer drives one of the 19 LED's in an octant with a 4 kHz sinusoidal signal. The corresponding 4QD receives this signal and produces a current proportional to the amount of light on each of the quadrants. These currents are converted to a voltage by a converter/amplifier combination connected directly to the 4QD and are fed to the multiplexer and sent to the VME VRASNIK module.

The VRASNIK module controls the RASNIK system and contains the central oscillators for the measuring signals and the filters and analog to digital converters (ADC's) that digitize the resulting signals.

The VRASMUX

Four multiplexer modules are placed in a crate (VRASMUX), containing the electronics needed for interfacing the VRASNIK to the optical parts of the alignment system. One crate connects to four octants, so there are four demultiplexers driving a LED inside four octants and four analog multiplexers connecting the corresponding 4QD segment to an ADC of the VRASNIK.

A microprocessor in the VRASMUX crate enables an easy command structure. The system has been setup in such a way that one simultaneously selects a LED and a segment of the corresponding 4QD for all four octants, with a single command.

The VRASNIK module

The VRASNIK module is divided in four fully separated analog sections each connected to one multiplexer module in the VRASMUX. Each section drives and reads out the 19 RASNIK systems in an octant. The interface to VME and the communication with the VRASMUX is common to the four channels of the VRASNIK.

For each of the four channels a clock signal of about 4 kHz is generated. The frequencies are slightly different for each channel to avoid cross talk. The signal is fed to the VRASMUX and drives one of the LED's in an octant. The light of the LED is projected by a lens onto the 4QD. The 4QD converts the light on each of the segments to a current proportional to the amount of light. These currents are converted to voltages and amplified, and then sent to the VRASMUX. One of the four signals of the selected 4QD is connected to the VRASNIK, where it first goes through a band pass filter. It is then converted to a DC signal, by multiplying it with the original 4 kHz signal and passes a low pass filter. The DC signal is proportional to the amount of light on the 4QD segment. The final filtering of the signal takes place in the ADC. The signal to be converted is integrated over a period of 40 ms, corresponding to two periods of 50 Hz.

The offset of the ADC is canceled by doing two measurements. One normal measurement, and one in 'inverted' mode giving a negative value. By subtracting the two values, the offset will cancel.

3.5 The RASNIK monitoring software

Figure 3.13 shows a schematic layout of the RASNIK monitoring system. The commands given at `ra_user` or `vmectrl` go to the command processor `cp`. The `cp` decides to which `ra_server` process the command should be sent. In the usual configuration, all RASNIK processes run on one VME crate meaning there's only one `ra_server` process running. The `ra_server` then writes the command to the `ra_data` data module from which it is picked

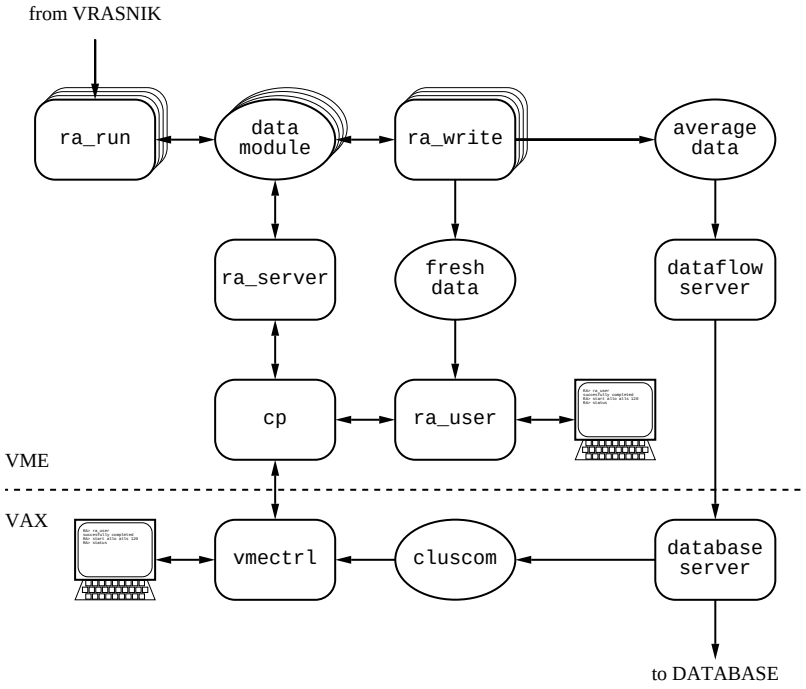

Figure 3.13 Schematic layout of the RASNIK monitoring system. In the usual configuration all processes shown run on the same VME crate. The command path goes from the user-interface (`vmectrl` on VAX or `ra_user` on VME) through the command processor `cp` and the server `ra_server` to the data modules and from there to the actual data taking processes `ra_run`. For each command the `ra_server` sends back the (updated) status. The data path goes from the data modules through the writing processes `ra_write` to averaged and fresh data files. The fresh data can be picked up by `ra_user` for displaying them as they come in. The averaged data are picked up by the data flow server which sends them to the VAX, where they can be sent to the database or be used for display by the `vmectrl` program.

up by the respective data taking processes `ra_run`. The `ra_server` then notifies the `cp` of the successful completion of the command and reports the current status.

The `ra_run` process picks up the data as they are made available by the VRASNIK module. These data consist of the intensities of the 4QD's of all systems for four octants. It calculates the position of the RASNIK systems at the lens positions. For the horizontal RASNIK it applies a global slope correction of 1.05, as is the estimated average factor between calculated and true position. For the vertical systems it applies individual corrections, that have been measured

system by system after their mounting in the octants. `Ra_run` then writes every individual measurement and calculated position for each system into the data module and signals the `ra_write` process that new data have arrived. `Ra_write` reads these data from the data module, and writes them to a file in memory, where they can be picked up by the `ra_user` process for display.

The `ra_run` process also averages the data. It does so by accumulating all the data for a certain amount of time. One measurement of each system in an octant takes around one minute. The time that the `ra_run` process should take to average the data can be set from the `ra_user` or from the `vmectrl` program. The default time during data taking is currently set at two hours, corresponding to about 170 measurements. After enough data have been taken, `ra_run` calculates the average light intensities and positions and writes them to the data module and signals the `ra_write` process that new averaged data have arrived. `Ra_write` then writes these data to a file on disk, where they can be picked up by the data flow server.

`Ra_write` writes the data in two different formats. Firstly, it writes both fresh and averaged data in a system-by-system way, i.e. four intensities, one x position, one y position and a status word for each of the 19 systems in one octant. Secondly, it writes chamber-by-chamber information, i.e. one x position, two y positions and a status word for each of the 5 chambers in an octant, and two x values and two status words for the two vertical systems.

The first form is mainly for debugging purposes. One has all the information available, e.g. for checking one system as function of time. These data are written only to local OS9 files and to the on-line data base. As of 1991 they do not go to the off-line database anymore.

The second form has all the information needed for the off-line muon reconstruction. The chamber information contains the horizontal displacement of the middle bridge (x coordinate) and the vertical displacement of the two outsides of the middle bridge (the two y coordinates). The two values for the vertical alignment system are the displacements of the middle chamber at the magnet door side (MD) and at the interaction point side (IP).

3.6 Data integrity

Several tests are performed to probe the integrity of the individual measurements of each of the systems. If one or more of the tests fail, the corresponding measurement is discarded and a flag in the status word for that system is set. The following sections discuss the various tests.

Intensity check

Any temporary or permanent malfunctioning of one of the RASNIK systems will result in the intensity readout for one or more quadrants in that system to be abnormal. Every intensity readout is therefore checked to be in range. If the intensity readout for one of the quadrants is found to be too low or too high, a bit in the status word is set. Also the sum of the intensities of the four quadrants must be between preset limits. A data overflow can be signaled by the

hardware as well, and such an overflow will be caught by the software and also set a bit in the status word.

These checks on the intensity provide a simple and effective means of detecting spurious measurements and defective systems.

System quality check

A somewhat more refined method of checking the data integrity is to use the ratio of the intensities measured by each quadrant. If the quality Q of a RASNIK system is defined to be:

$$Q = \begin{cases} \dfrac{q_0 q_3}{q_1 q_2}, & \text{for } q_0 q_3 < q_1 q_2 \\ \dfrac{q_1 q_2}{q_0 q_3}, & \text{for } q_0 q_3 > q_1 q_2 \end{cases} \tag{3.10}$$

where q_i is the measured intensity on quadrant i, then a value of $Q \simeq 1$ indicates a good RASNIK system, since the ratio q_0/q_1 should equal q_2/q_3 for a system with a perfectly homogeneous square light source, and four equally responsive quadrants. If one of the four quadrants would slowly breakdown, the value for Q would decrease. When Q becomes too low (the current limit is set at 0.6) a bit is set in the status word, and the measurement will not be used. The value 0.6 is chosen such that all working systems are above that limit, and corresponds to an error in position of about 50 μm. Figure 3.14 shows the quality Q for all the RASNIK systems currently in use in the L3 muon chamber system.

Software noise filter

The data taken by RASNIK sometimes show large fluctuations for individual measurements. These fluctuations come about for instance when the laser beacon system, measuring the octant torque, is switched on. The rotating laser beam occasionally hits one of the 4QD's, resulting in a spurious RASNIK measurement. These measurements and others with similar characteristics, are being filtered out by a software noise filter. The purpose of this filter is to discard the spurious measurements, and to identify real changes in alignment. When a real change is detected, the accumulated data are being averaged and sent to the database, even if the time limit set has not yet been met.

Since the data are sent to the database octant by octant, a not recognized noisy measurement from one of the 19 systems will result in all RASNIK data for the octant concerned to be sent to the database. Therefore, care has to be taken that the filter is not too sensitive, as it would then generate large amounts of data.

The filter works as follows. The first measurement in a series is taken as the starting point x_s. All measurements x_i following, that satisfy $|x_\mathrm{s} - x_i| < \Delta x$ are accumulated until a real change in alignment occurs, or until the time limit has passed. The value of Δx is 5 μm for changes in x and 10 μm for y. A real change is triggered when the previous measurement x_{i-1}

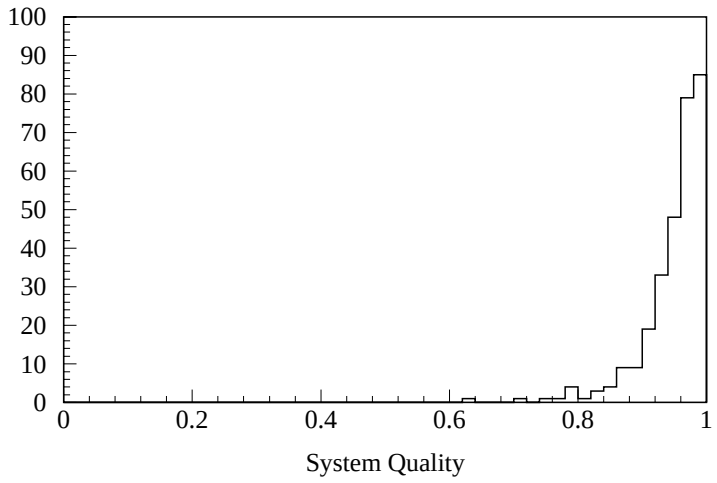

Figure 3.14 The quality of the 300 RASNIK systems which ideally equals one. A system with a non homogeneous LED or with a malfunctioning 4QD has a low quality value. Measurements from a system with a value below 0.6 will not be used.

and the current measurement x_i lie outside $x_\mathrm{s} \pm \Delta x$ but are close together, $|x_{i-1} - x_i| < \Delta x/2$. When such a change occurs, the point x_{i-1} is taken as the new starting point x_s

In order to reject noise measurements that accidentally satisfy the trigger condition $|x_{i-1} - x_i| < \Delta x/2$, the starting point is allowed to change maximally by 2 μm at a time. For example, a jump in position of 20 μm would require about 10 measurements for x_s to become close enough to the current measurement x_i. Since the time between two measurements can be up to about one minute, this limits the response time of the system to jumps in the alignment, but greatly improves the noise filtering capacities. So far, the RASNIK system has not suffered from this response limitation, but if the L3 muon chamber system were to explode, RASNIK would not be the first to sound an alarm.

Chapter 4

Tau pair cross section

This chapter describes the selection of tau pair events coming from the reaction:

$$e^+e^- \rightarrow \tau^+\tau^-(\gamma)$$

and the determination of the cross section for this reaction as a function of $\sqrt{s}$. A short overview of the properties of these events is given and the various background channels are discussed. The selection criteria that have been used are listed in section 4.3 and the simulation of detector inefficiencies and the determination of the trigger efficiency are treated in the sections 4.4 and 4.5. The tau pair cross section is calculated in section 4.6 and finally the systematic errors due to the event selection and other sources are discussed and summarized in the last section.

4.1 Tau pair events

Since the tau lepton itself is short-lived, τ_τ = 0.3 $\times$ 10^{-12} s, it decays even before it enters the sensitive part of the detector and hence the tau pair events have to be selected by the decay products. The tau lepton decays via the W emission diagram shown in figure 4.1. The dominant decay modes of the tau are listed in table 4.1 together with the corresponding branching fractions. The number of charged particles in the decay (i.e. the number of prongs), is one or three, for most of the taus. The charge multiplicity of the tau pair events is between 2 and 6 for more than 99.9% of the events.

Each tau has an energy close to the beam energy, which is about 45 GeV, and travels on average 2.3 mm before decay. At least one neutrino is produced in each tau decay, therefore the event energy seen by the detector (visible energy) can be substantially smaller than the total center of mass energy. Due to the high Lorentz boost at LEP energies, the decay products of one of the taus enter the detector nearly opposite to those of the other one: the average acollinearity angle between objects reconstructed from the decay products of the two taus is three degrees.

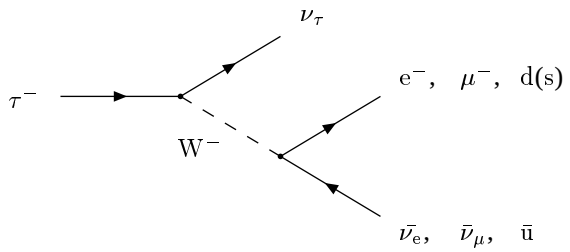

Figure 4.1 Feynman diagram for the decay of the τ^-.

τ Decay Mode		Branching Fraction (%)
$\mu\nu_\mu\nu_\tau$	1 prong	17.58 ± 0.27
$\mathrm{e}\nu_\mathrm{e}\nu_\tau$	1 prong	17.93 ± 0.26
hadrons ν_τ	1 prong	50.3 ± 0.4
hadrons ν_τ	3 prong	14.06 ± 0.25
hadrons ν_τ	5 prong	0.111 ± 0.024

Table 4.1 Branching fractions for leptonic and hadronic tau decays into one, three and five charged particles (prongs). The hadronic decays include production of additional neutral particles [35].

Figure 4.2 shows a tau event as seen by the L3 detector. Identified are a positron on one side from the decay $\tau^+ \rightarrow \mathrm{e}^+\nu_\mathrm{e}\bar{\nu}_\tau$ and three charged hadrons on the other side from the decay of the $\tau^- \rightarrow \mathrm{hadrons}\,\nu_\tau$. The shower profile of the energy deposition in the electromagnetic calorimeter on the right hand side is consistent with that of an electron, positron or photon. The track in the tracking chamber pointing towards the cluster shows that it is not a photon and the curvature of the track determines the charge of the particle (a positron) and, consequently, of the original tau. The energy of the positron was measured to be 19 GeV. The hadronic cluster on the opposite side has an energy of 29 GeV. Because of the Lorentz boost, the hadrons are in a very collimated jet.

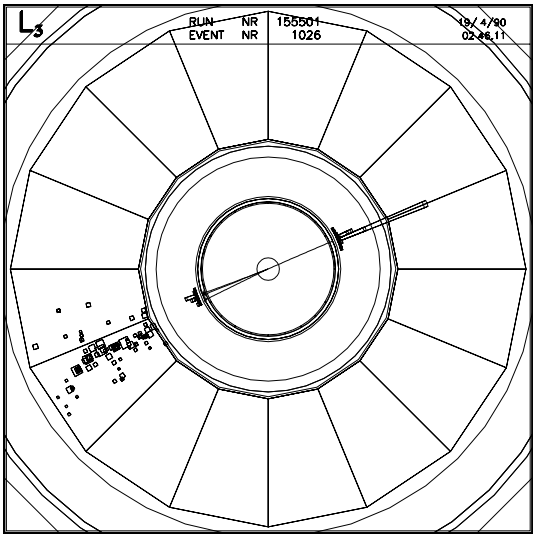

Figure 4.2 An event of the type $e^+e^- \to \tau^+\tau^- \to e^+ + \mathrm{hadrons} + \nu$'s. The positron and hadrons are identified by the depth and shape of the shower in the calorimeters. The charge of the original taus is measured by adding the charge of their respective decay product(s), as measured in the TEC.

4.2 Background processes

The process $e^+e^- \to q\bar{q} \to \mathrm{hadrons}$

Of all possible decays of the Z^0, the hadronic decay has the largest branching ratio. The hadronic cross section is about 21 times the tau pair cross section. Hadronic decays of the Z^0 involve many particles in the final state. The number of charged tracks therefore will be high (the charge multiplicity is 21 on average). Also the number of clusters or bumps in the ECAL (local maxima in the BGO energy deposition) will be high.

Figure 4.3 shows two $e^+e^- \to q\bar{q}$ events. One is a typical hadronic event (*a*), showing many tracks in the TEC and many (mostly low energetic) clusters in the ECAL. Figure 4.3*b* shows one of the few hadronic event candidates remaining in the selected tau cross section sample. This event has 6 charged tracks and 12 electromagnetic clusters in the ECAL. Since in addition the reconstructed total energy is 110 GeV it is likely to be a hadronic event.

The process $e^+e^- \to e^+e^-$

The lowest order diagrams contributing to the Bhabha scattering process $e^+e^- \to e^+e^-$ are

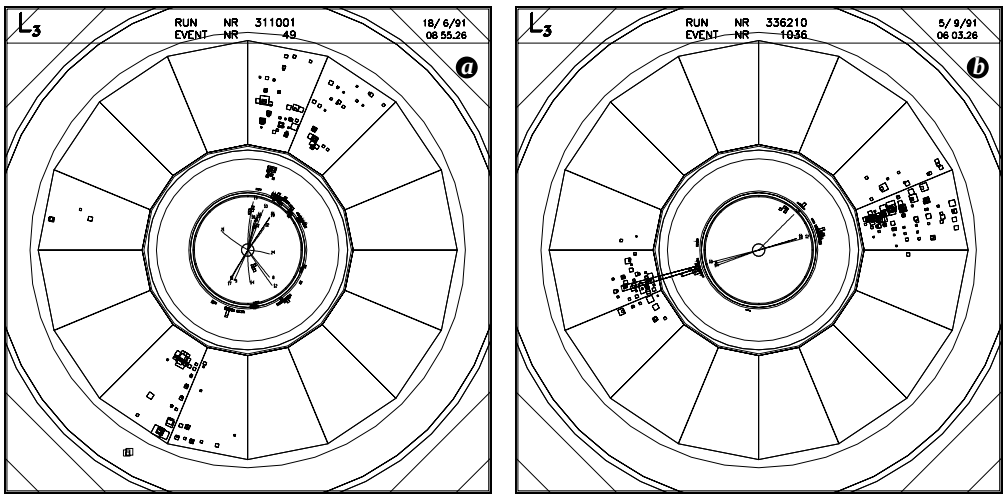

Figure 4.3 *a)* A typical hadronic event and *b)* a hadronic background event candidate selected in the tau sample.

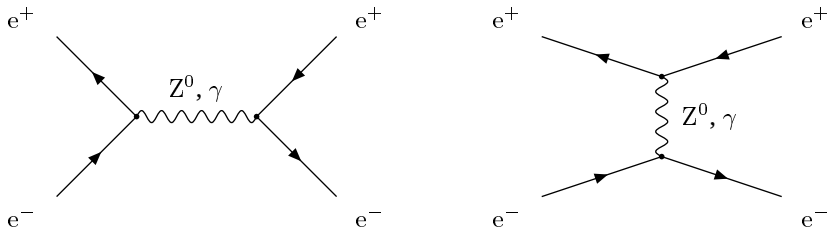

Figure 4.4 Feynman diagrams for the Bhabha scattering process in lowest order. The left and right hand side correspond to the so-called s- and t-channel respectively.

shown in figure 4.4. The events are characterized by two back to back electromagnetic clusters in the ECAL, each having an energy close to the beam energy. The energy distribution for electrons from Bhabha scattering has a long tail towards lower energies. This originates from initial or final state radiation, or from detector defects. Although the energy spectrum for electrons produced in tau decays drops at higher energies because of the two neutrinos that are produced in this decay, it does extend up to the beam energy. For this reason it can sometimes be hard to distinguish Bhabha scattering events from tau pair events. Figure 4.5*a* shows an example of a typical $\mathrm{e^+e^-} \rightarrow \mathrm{e^+e^-}$ event. The reconstruction program identified an electron

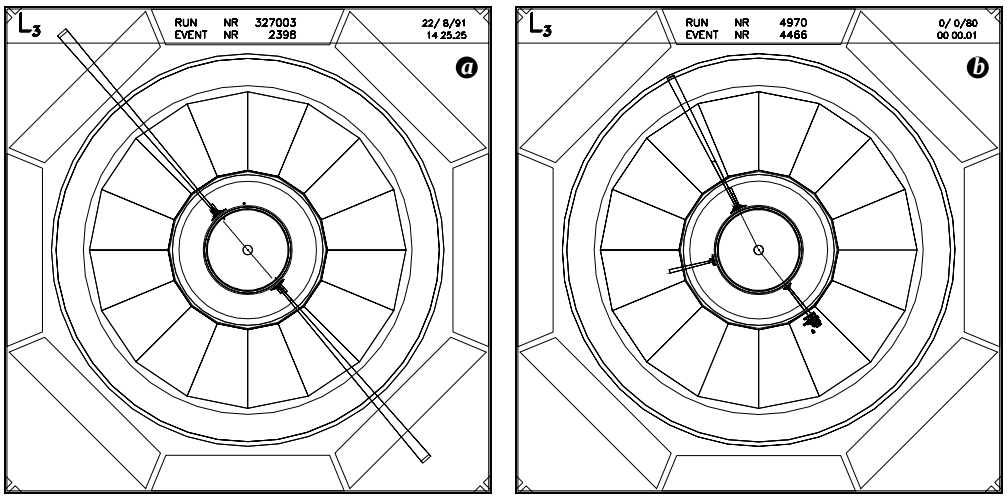

Figure 4.5 *a)* Typical Bhabha scattering event. The energy of both electromagnetic clusters is about 45 GeV. *b)* Radiative Bhabha Monte Carlo event satisfying the tau pair selection criteria.

and a positron each having an energy of about 45 GeV. The two electromagnetic clusters are back to back and both have a track in the TEC. Figure 4.5*b* shows a radiative Bhabha event satisfying the tau pair selection criteria. This is a simulated event. The reconstruction program identified on one side an electron of 39.8 GeVand a photon of 9.2 GeV. Because part of the shower of the positron on the other side probably goes through a gap between the BGO crystals and reaches the hadron calorimeter, this cluster was classified as a hadronic cluster with an energy of 46.5 GeV.

The process $\mathrm{e^+e^-} \rightarrow \mu^+\mu^-$

The dimuon events are characterized by two back to back muons detected in the muon chambers. Each of the muons has an energy close to the beam energy. This background is often hard to distinguish from the process $\mathrm{e^+e^-} \rightarrow \tau^+\tau^- \rightarrow \mu^+\mu^- + \nu'$s, especially for radiative events, or if the muon goes through a dead part in the muon detector. The branching fraction for $\tau \rightarrow \mu\nu\nu$ is 17.6%, so about 3% of the tau pairs decay into two muons. Figure 4.6*a* shows a typical $\mathrm{e^+e^-} \rightarrow \mu^+\mu^-$ event. Both muons have a reconstructed momentum of about 45 GeV, and are back to back. A simulated dimuon event surviving the tau pair selection is shown in figure 4.6*b*. Here both muons pass through the gap between the muon chamber octants. The lower muon has a hard bremsstrahlung photon and the combination of ECAL and HCAL hits was identified as a hadronic jet of 51 GeV. The upper cluster was identified as a low energy hadron

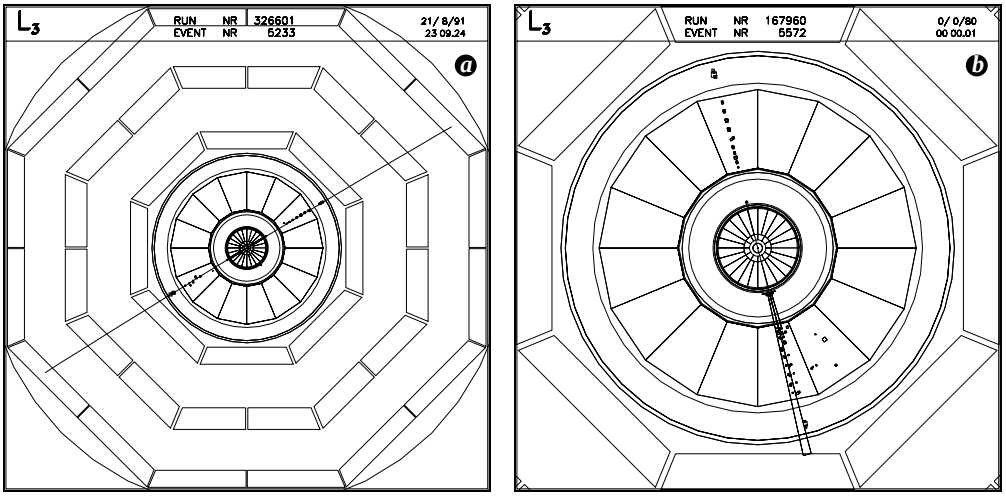

Figure 4.6 *a)* Typical muon event, where both muons have a momentum of about 45 GeV. *b)* A background Monte Carlo muon event satisfying the tau pair selection criteria. Both muons go through the gap between the muon chamber octants. The lower muon has a hard bremsstrahlung photon of 43 GeV.

of 3.2 GeV*.

The process $\mathrm{e^+e^-} \rightarrow \mathrm{e^+e^-}\,f\bar{f}$

Figure 4.7 shows the Feynman diagrams of two of the processes contributing to the production of four-fermion final states in $\mathrm{e^+e^-}$ collisions. These processes usually involve two virtual photons and are therefore often referred to as *two photon events*. Since the cross section for $\mathrm{e^+e^-} \rightarrow \mathrm{e^+e^-}f\bar{f}$ is much larger than the cross section for $\mathrm{e^+e^-} \rightarrow f'\bar{f}'f\bar{f}$ (where f' is not an electron) only the first process is considered [36]. The background has been studied using Monte Carlo simulation, with in the final state $f\bar{f} = \mathrm{e^+e^-}$, $\mu^+\mu^-$, $\tau^+\tau^-$ or $\mathrm{u\bar{u}} \rightarrow \mathrm{hadrons}$. These background events might resemble a selected $\tau^+\tau^-$ event, when the final state particles are at large scattering angle. The angular distribution of the background events, however, is sharply peaked in the forward direction. Moreover, the energy depositions are in general not back to back, as is the case for $\tau^+\tau^-$ events. A typical example of a two photon event candidate with two electrons visible in the barrel detector can be seen in figure 4.8*a*. The electrons are not collinear along the beam direction, but they are back to back in the transverse plane (*a'*). Figure 4.8*b* shows an event selected in the tau sample. It is a possible candidate

*For the tau pair event selection the possibility of identifying muons only by minimum ionizing tracks in the HCAL is not used.

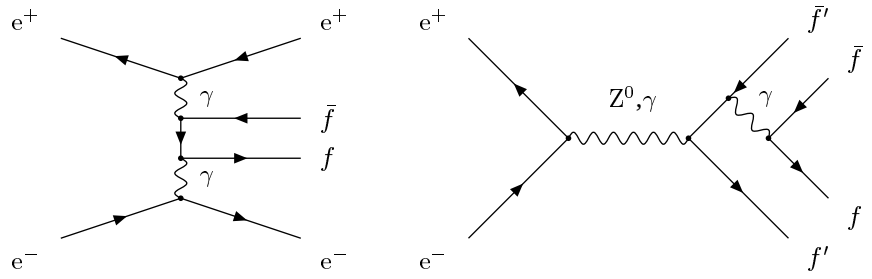

Figure 4.7 Feynman diagrams of two processes involved in the production of four-fermion final states in e^+e^- collisions.

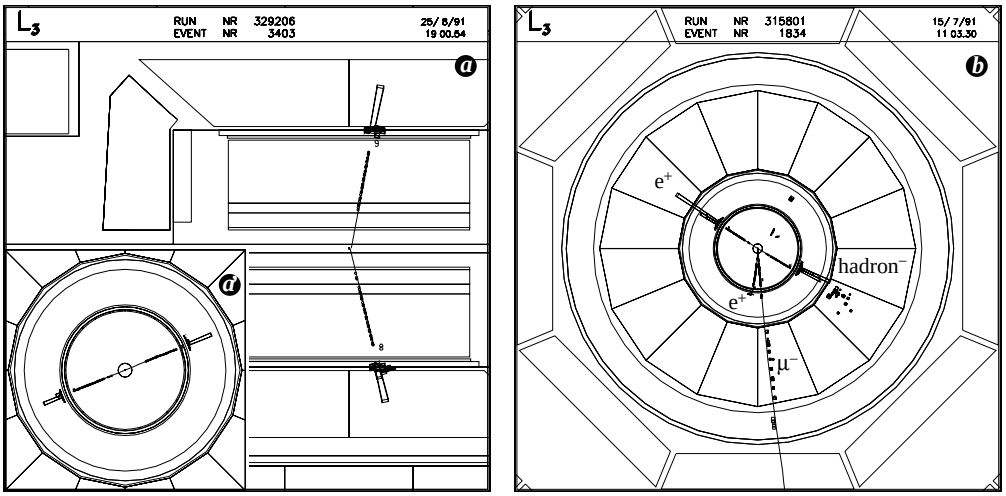

Figure 4.8 *a*) Typical two photon event with two electrons visible in the detector in shown in side view and transverse view (*a'*). *b*) Background four fermion event candidate, probably $\tau^+\tau^-\tau^+\tau^-$, selected in the tau pair sample.

for $e^+e^- \rightarrow \tau^+\tau^-\tau^+\tau^-$ produced through the process shown in the right hand side Feynman diagram of figure 4.7. The following particles are identified: an e^+ (19.3 GeV) nearly back to back with a hadron$^-$ (22.1 GeV); an e^+ (0.26 GeV) and a μ^-(7.8 GeV) [37].

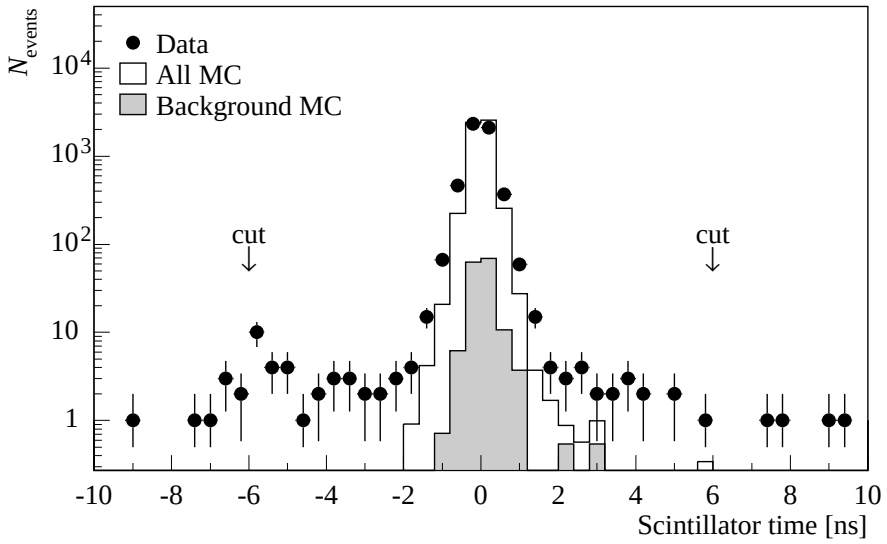

Figure 4.9 Scintillator time distribution for data and Monte Carlo. The tails are due to cosmic rays.

Cosmic rays

Cosmic rays that pass the detector close to the vertex, may look like events originating from the interaction point. Since they pass the detector at random times, their number can be effectively reduced by selecting only those events that occur in a narrow time window around the beam crossing time. The event timing is measured with the scintillator counters. The scintillator time distribution is shown in figure 4.9. The time has been corrected for time of flight such that a particle originating from the interaction point should have a scintillator time of zero. The data points in the histogram represent the events that were selected with the criteria that will be described in the next section. All criteria were applied, except for the requirement on the scintillator timing. The gray histogram shows the Monte Carlo distribution for the background events ($\mathrm{e^+e^-} \to \mathrm{e^+e^-}$, $\mu^+\mu^-$, $\mathrm{hadrons}$; two photon events); the outlined histogram represents the sum of the background Monte Carlo and the Monte Carlo $\mathrm{e^+e^-} \to \tau^+\tau^-$ events. Cosmic ray events are present in the data sample, but have not been simulated. The tails in the scintillator time distribution are mainly due to cosmic rays.

4.3 Selection criteria

The purpose of the selection criteria is to reject the background, while retaining the tau events. These criteria use those properties of the tau events that distinguish them most from one or more of the background channels. As has been shown in section 4.1 tau pair events are characterized by two back to back low multiplicity jets. Although these features can be recognized with the central tracking chamber the selection described in this thesis is based mainly on the calorimetric and muon chamber data of L3. Since the TEC started to work only reasonably well in the beginning of 1990, we decided not to rely heavily on its performance for the 1990 event selection. The 1991 data has been treated in the same way in order to have a consistent analysis.

In figure 4.10 two of the most sensitive measured quantities used for selecting tau events are plotted against each other. They are the distribution of the energy deposited in the electromagnetic calorimeter[†], normalized to $\sqrt{s}$, versus the number of electromagnetic clusters. The number of electromagnetic clusters is a measure for the number of particles produced in the reaction. The plot contains events from Z^0 decay into $\mathrm{e}^+\mathrm{e}^-$, $\mu^+\mu^-$, $\tau^+\tau^-$ and $q\bar{q}$. These events are required to be contained in the BGO barrel region ($|\cos\theta_{\mathrm{thr}}| < 0.7$), and have at least one scintillator hit within 6 ns of the beam crossing time. As is indicated in this plot, the $\mathrm{e}^+\mathrm{e}^-$ events are at low multiplicity ($N_{\mathrm{clusters}} \sim 2$) and high electromagnetic energy ($E_{\mathrm{BGO}}/\sqrt{s} \sim 1$). The $\mu^+\mu^-$ events have low multiplicity and low electromagnetic energy: they typically have two electromagnetic clusters of 250 MeV each, corresponding to the energy loss in the ECAL of a minimum ionizing particle. The hadronic events have medium electromagnetic energy and high multiplicity. The tau events have medium electromagnetic energy and medium multiplicity; very few events contain more than 15 clusters.

The selection criteria used for the cross-section measurement are as follows:

1. The event is required to be contained in the BGO barrel region: the polar angle θ_{thr} of the event thrust axis has to satisfy $|\cos\theta_{\mathrm{thr}}| < 0.7$;

2. The event is required to have at least two well separated objects (ASJT's, as described in section 2.11), each having an energy of more than 3 GeV;

3. The energy deposited in the electromagnetic calorimeter has to be greater than 2 GeV and less than $0.75\sqrt{s}$;

4. The number of clusters in the electromagnetic calorimeter has to be less than 13 and the number of charged tracks in the central tracking chamber must be less than 9;

5. The event has to have at least one scintillator hit which, after time of flight correction, has to coincide with the beam crossing within 6 ns;

[†] The total electromagnetic energy used in this analysis has not been optimized to match either electromagnetic or hadronic showers, but it has been scaled such that $E_{\mathrm{BGO}} \simeq \sqrt{s}$ for Bhabha events.

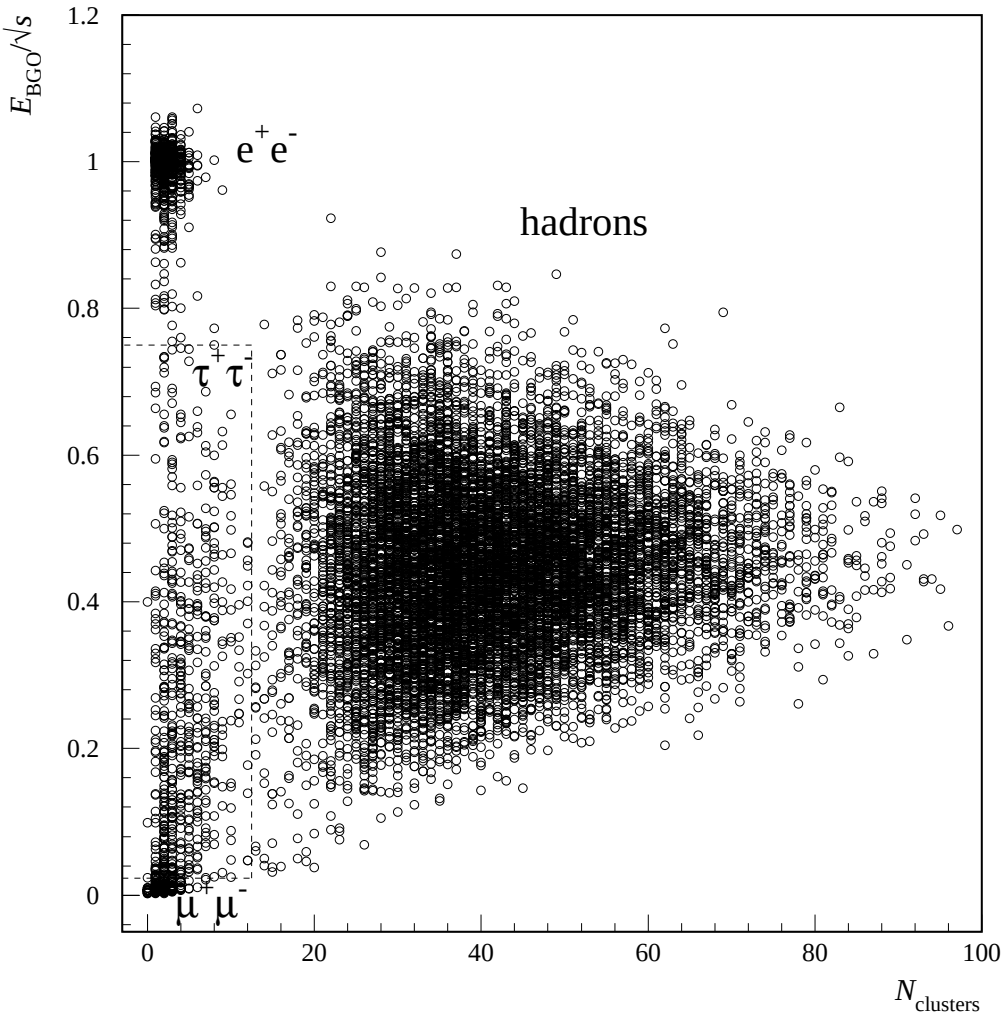

Figure 4.10 Distribution of $E_{\mathrm{BGO}}/\sqrt{s}$ versus the number of electromagnetic clusters. The hadronic events have a high number of clusters; the electron-pair events have high electromagnetic energy, the muon-pair events low. The tau events have medium electromagnetic energy, and a low number of clusters.

6. The acollinearity angle $\zeta_{1,2}$ between the two most energetic jets must be less than 14°.

For events with recognized isolated muons (i.e. the muon momentum should exceed $0.8E_{\text{ASJT}}$), we require:

7. The momentum of the isolated muon should be less than $0.88E_{\text{beam}}$ and there should be no more than one isolated muon;

8. For the 1990 data the muon must satisfy a momentum dependent vertex cut:

$$V_r < 50 + \frac{300}{|P_\mu| \sin\theta_\mu}\,\text{mm}; \quad V_z < 100 + \frac{500}{|P_\mu| \sin\theta_\mu}\,\text{mm}$$

where V_r and V_z are the distance of the muon track to the vertex in the transverse and longitudinal direction respectively, P_μ is the muon momentum in GeV and θ_μ is the polar angle of the muon. For the 1991 data the muon is accepted if it passes through a box around the event vertex with dimensions $r < 50$ mm and $z < 100$ mm. For muons missing one P- (Z-) segment, the box is made twice as big in r (z). The muon is rejected if it passes outside a box ten times as big in r and z. If it passes through the bigger box, but lies outside the smaller, it is accepted only if both r and z are within three standard deviations (error on the muon vertex position after backtracking) from the event vertex.

For events with recognized electrons (i.e. an ASJT classified as an isolated electron or an electron in a jet), we require:

9. The energy deposited in the electromagnetic calorimeter by the electron should not exceed $0.88E_{\text{beam}}$.

Criterion (1) defines the fiducial volume. It requires the event thrust axis to lie inside the region covered by the electromagnetic calorimeter barrel. The event thrust axis is in the direction $\vec{n}_{\text{thr}}$ defined by:

$$T = \frac{\max\limits_{\vec{n}_{\text{thr}}} \sum\limits_i |\vec{E}_i \cdot \vec{n}_{\text{thr}}|}{\sum\limits_i |\vec{E}_i|} \tag{4.1}$$

where T is the event thrust, $\vec{n}_{\text{thr}}$ the unit vector in the thrust direction. $\vec{E}_i$ is the vector in direction of cluster i with energy $|\vec{E}_i|$. For two jet events the thrust axis almost coincides with the first jet axis. Requiring the event to lie in the BGO barrel region enables the use of the good energy resolution of the BGO to reject the Bhabha events, and the use of the number of electromagnetic clusters as a measure for the event multiplicity. Furthermore, two photon events which are mostly produced in the forward direction, will be strongly suppressed at larger angles.

Requiring the event to have more than 2 GeV electromagnetic energy (3) rejects cosmic ray events, that often consist only of a muon going through the detector, and $\mathrm{e^+e^-} \rightarrow \mu^+\mu^-$

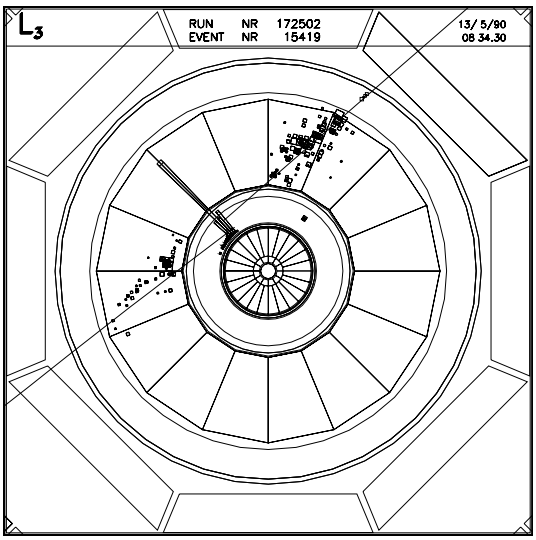

Figure 4.11 Cosmic ray event with three "jets": two were reconstructed as jets with a muon, the third (in the middle) as a hadron jet. The event has a scintillator hit in time relative to the beam crossing, and was removed by requiring that the acollinearity angle between the two most energetic jets be less than 14°.

events. The energy deposited in the BGO by each muon is typically around 250 MeV, as can be seen from figure 2.5. The high cut on the total electromagnetic energy will reject $e^+e^- \to e^+e^-(\gamma)$ events, and the cut on the energy of each recognized electron (9) further reduces this background. The background from $e^+e^- \to \mu^+\mu^-(\gamma)$ is further reduced by criterion (7), the muon momentum cut.

Events of the type $e^+e^- \to q\bar{q}$ will be rejected by the multiplicity cut (4). Almost all tau events have charge multiplicity less than or equal to 6 (cf. table 4.1), so the cut on the number of tracks allows for a possible misfit of tracks (e.g. of mirror tracks) and photon conversion resulting in two additional tracks.

The $e^+e^- \to e^+e^- f\bar{f}$ background and the cosmic ray background will be reduced by the cut on the acollinearity angle (6). Although the two photon events will usually be back to back in the transverse plane, they will in general not be back to back in r-θ. An example of a cosmic ray event removed by this cut, is show in figure 4.11. Cosmic rays will enter the detector at random times. By selecting events which are inside a narrow time window (5) the number of cosmic ray events will be further reduced.

Bad runs are removed from the data. A run is declared bad, if during the run or the reconstruction some failure occurred in one or more of the sub detectors (tracking chamber,

scintillators, electromagnetic calorimeter, hadron calorimeter, muon chambers). In order to eliminate systematic errors from these failures, which might influence the efficiency, events that are recorded in such runs will not be used.

After applying the selection criteria and removing the bad runs, a sample of 2564 events for the 1990 data taking period and 6950 for the 1991 period remains.

The selection criteria will be discussed in more detail in section 4.7 when the determination of the systematic errors is treated.

4.4 Simulation of detector imperfections

The acceptance for tau-pair and background events, using the above listed selection criteria, is determined with simulated events. The kinematics of the final state of these events is generated, according to theoretical predictions, with Monte Carlo event generation programs [38, 39, 40, 41, 42]. The response of the L3 detector to these events is modeled with the GEANT3 [43] detector simulation program which includes the effects of energy loss, multiple scattering and showering in the detector materials and in the beam pipe. The simulation uses a complete representation of the L3 detector, including the details of each sub detector geometry down to a level of accuracy of typically 10–100 microns. Simulation of the detector imperfections needs additional attention since the standard simulation models a 'perfect' detector.

The status of the detector varies with time during the data taking period. For instance hot or dead BGO crystals, disconnected sectors, inefficient wires and dead cells change the behavior of the detector. For a precise measurement of the tau cross section, the time dependent imperfections of the detector response must be simulated.

Removing BGO hits

The information on the status and calibration of the electromagnetic calorimeter is stored in the L3 database. During reconstruction of real events, the appropriate information is retrieved from the database using the time and date recorded in each event. Using this information, data from dead or hot crystals are discarded and appropriate calibrations are applied. During reconstruction of simulated data, each event is temporarily assigned a time and date such that the events are distributed over the data taking period with the correct luminosity weighting. The same information from the database that was used for the real data is then used for the simulated events to discard the dead and hot crystals.

Smearing the muon momentum

For the muon simulation one encounters a similar problem. Cells in the muon chambers can be malfunctioning for various reasons. One of the wires in a chamber might break and cause a short circuit in a number of neighboring cells or dust on the wire might cause high voltage problems. The status and high voltage of the muon chamber cells is stored in the database.

There are two approaches to simulate the bad cells in the Monte Carlo. The first approach uses a method equivalent to that used to discard the BGO crystals, i.e. cells in the muon chamber are switched off in the simulation for a time period proportional to the luminosity corresponding to the dead time of that cell in real life. This method has been used for the 1990 dimuon Monte Carlo.

The second approach takes into account the average effect of the muon chamber inefficiencies over the data taking period [44]. This method is used for the 1991 Monte Carlo and involves the following two steps. Firstly, the number of segments used in fitting the muon track is reduced in the simulation to match the number of segments in the data and, secondly, the momentum of the muon in the Monte Carlo is smeared to make the muon momentum distribution match that of the data. The muons used for this method in both the data and the Monte Carlo sample were selected with the selection cuts listed in section 4.3, but requiring the BGO energy to be less than 0.8 GeV instead of greater than 2 GeV and allowing for more than one isolated muon, without applying the muon momentum cuts. This modified selection yields a rather pure dimuon sample. The two steps of matching the Monte Carlo muon distributions with the data will now be described in more detail.

A muon segment is a fitted track in one P-chamber layer. Usually a muon track passes through three muon chamber layers and hence the track contains three segments (triplet). Because of the aforementioned imperfections, the muon track may lose one or more segments. For a muon track to be used in the tau analysis, it must have at least two segments[‡] (doublet). If η is defined to be the probability for one segment of a muon track to be lost, then the number of triplets and doublets in the Monte Carlo after removing segments will be:

$$\begin{aligned} N_3^{\mathrm{MC}'} &= (1-\eta)^3 N_3^{\mathrm{MC}} \\ N_2^{\mathrm{MC}'} &= 3\eta(1-\eta)^2 N_3^{\mathrm{MC}} + (1-\eta)^2 N_2^{\mathrm{MC}} \end{aligned} \tag{4.2}$$

where N_i^{MC} and $N_i^{\mathrm{MC}'}$ are the numbers of i-segment muon tracks in the Monte Carlo before and after removing segments, respectively. By comparing the fractions of triplets and doublets in the Monte Carlo:

$$\begin{aligned} f_3' &= \frac{N_3^{\mathrm{MC}'}}{N_3^{\mathrm{MC}'}+N_2^{\mathrm{MC}'}} \\ f_2' &= \frac{N_2^{\mathrm{MC}'}}{N_3^{\mathrm{MC}'}+N_2^{\mathrm{MC}'}} \end{aligned} \tag{4.3}$$

with the corresponding fractions for the data, the value of η is fitted to be $(4.0 \pm 0.5)\%$. Doublets (triplets) that lose one (two) or more segments will be lost. In reconstructing the simulated event, the corresponding jet energy that included the muon momentum will then be replaced by the sum of the energy depositions in the electromagnetic and hadronic calorimeters and the selection code will treat the jet as a hadronic jet.

In the second step the momentum distributions of triplet and doublet muon tracks in data and Monte Carlo have to be matched. Figure 4.12 shows the normalized inverse momentum

[‡] No requirement is made on the number of Z-chamber segments.

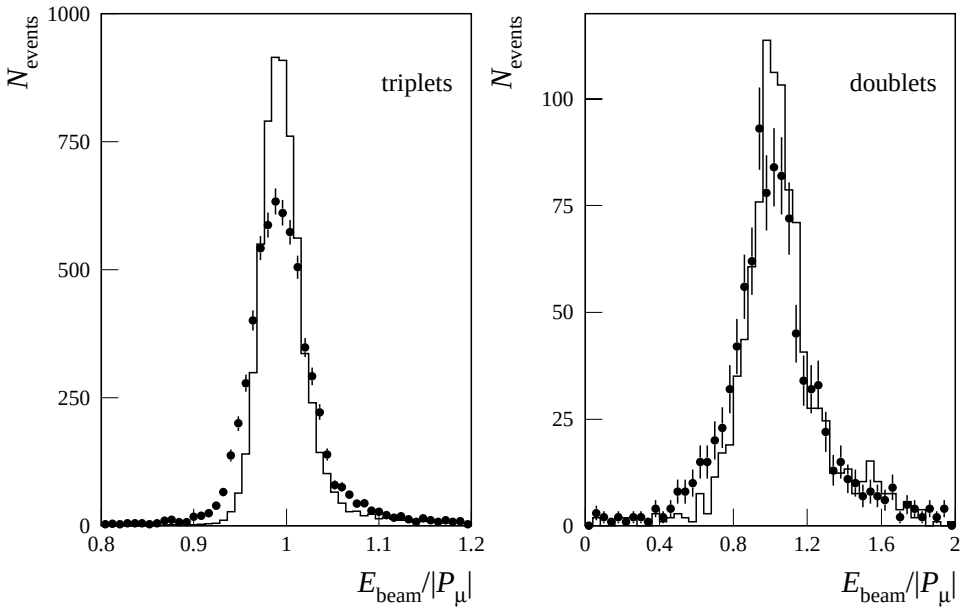

Figure 4.12 Comparison of the muon momentum resolution between Monte Carlo (histogram) and data (points), before removing segments and smearing. The left histogram shows the triplets, the right histogram shows the doublets. The Monte Carlo histograms have been normalized to the data.

distribution in data and Monte Carlo for triplets and doublets. A gaussian fit to these distributions yields the momentum resolutions $\rho = \sigma_{1/p}/(1/p)$ in data and Monte Carlo to be 3.1% (data), 2.1% (Monte Carlo) for triplets and 20% (data), 14% (Monte Carlo) for doublets.

The simulated momentum distributions can now be smeared with a gaussian distribution, to make data and Monte Carlo match. Since the resolution is momentum dependent and so far only momenta close to the beam energy have been considered, the following parameterization of the momentum resolution is used to extrapolate to lower momenta:

$$\rho^2(p) = \alpha^2(p - 2.5)^2 + \beta^2 + \frac{\gamma^2}{p^2} \tag{4.4}$$

where p is the muon momentum at the vertex in GeV and the parameters α, β and γ come from:

α: intrinsic muon spectrometer resolution;

β: multiple scattering in the muon chambers;

γ: energy loss in the inner detectors.

The multiple scattering and the energy loss in the inner detectors is assumed to be well simulated by Monte Carlo. The discrepancy in resolution is then due only to the difference in intrinsic resolution. Since this involves only the muon chambers, the average energy loss in the inner detector (2.5 GeV) is subtracted from the muon momentum in the first term in eq. 4.4. The amount of smearing $\rho_{\rm smear}$ of the Monte Carlo, in order to make it match the data is determined by:

$$\rho^2_{\rm smear} = \rho^2_{\rm data} - \rho^2_{\rm MC} \tag{4.5}$$

or

$$\rho_{\rm smear} = \sqrt{\alpha^2_{\rm data} - \alpha^2_{\rm MC}}\,(p - 2.5) = \Delta_\alpha (p - 2.5) \tag{4.6}$$

This amount of smearing can be determined from the distributions shown in figure 4.12. However, since these distributions are not perfectly gaussian, the value for Δ_α has been extracted in an iterative way, comparing the widths of the smeared distributions with the data. The values obtained are:

$$\Delta_\alpha = \begin{cases} 0.042\% & \text{for triplet} \rightarrow \text{triplet} \\ 0.38\% & \text{for triplet} \rightarrow \text{doublet} \\ 0.32\% & \text{for doublet} \rightarrow \text{doublet} \end{cases} \tag{4.7}$$

The resulting Monte Carlo momentum distribution for doublets and triplets is compared to the data in figure 4.13. The systematic error due to the muon momentum smearing has been estimated by varying the values of Δ_α by $\pm 50\%$. The resulting change in tau cross section was found to be less than 0.1%.

Matching the number of clusters

The number of electromagnetic clusters, or bumps, is a measure for the number of particles coming from Z^0 decay. The number of clusters is used in this analysis to separate the hadronic Z^0 decays from the decays of the Z^0 into tau pairs, as was illustrated in figure 4.10 on page 54. The distributions of the number of bumps in data and Monte Carlo do not agree very well. On average there are more electromagnetic clusters in the data than in the Monte Carlo. These extra clusters could for instance originate from electronics noise that has not been simulated by the Monte Carlo.

The distributions are made to match by replacing the Monte Carlo distribution by the data distribution. In order to do this, the data are first split in three sub samples for which different bump distributions are expected. This is done by considering the number of charged tracks (prongs) in the TEC for each of the two most energetic 'jets' in each event. The sub samples are:

$1 \leftrightarrow 1$**:** events with one prong on one side and one on the other;

$1 \leftrightarrow 3$**:** events with one prong on one side and three on the other;

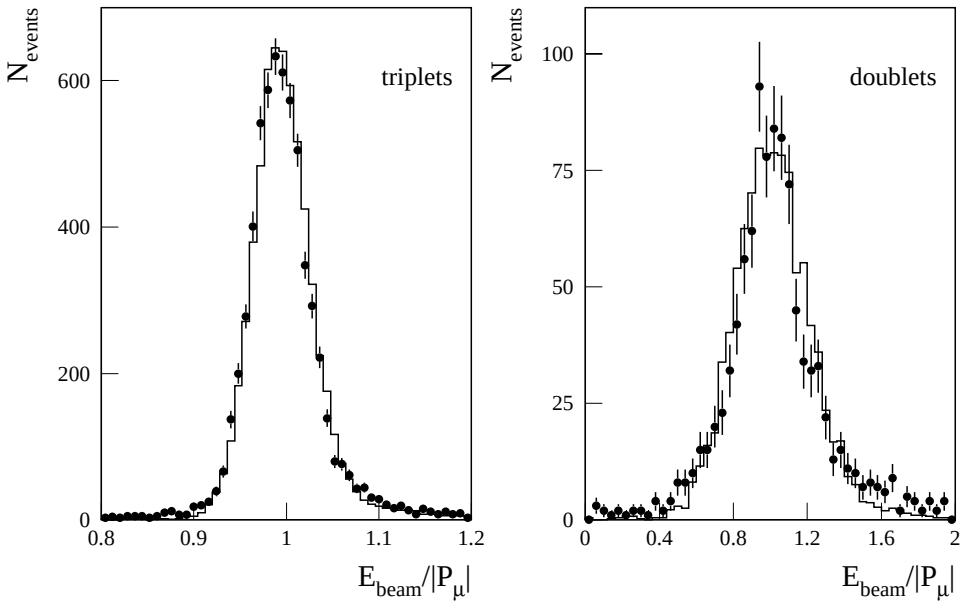

Figure 4.13 Muon momentum resolution after removing segments and smearing. The left histogram shows the triplets and the right histogram the doublets. The Monte Carlo (histogram) has been scaled to the data (points).

$3 \leftrightarrow 3$**:** events with three prongs on one side and three on the other.

By requiring furthermore that the angle between the jet axis and any track in one jet should not be more than 15° most of the hadronic background, mainly present in the third sub sample, has been removed. In total there are 4724 events in these sub samples out of a total of 5482 events on the Z^0-peak ($\sqrt{s}$ =91.2 GeV). Figure 4.14 shows the distributions of the number of bumps for each of the three sub samples compared to Monte Carlo. The Monte Carlo predicts fewer clusters than are present in the data.

When simulating the number of electromagnetic clusters in the ECAL for tau pair events the *generated* number of prongs for each event is determined and the corresponding data distribution is used to randomly assign the number of bumps for that event. The resulting Monte Carlo distribution is shown in figure 4.15, together with the data points. The dashed histogram shows the uncorrected tau pair Monte Carlo distribution. The corrected Monte Carlo distribution matches the data very well.

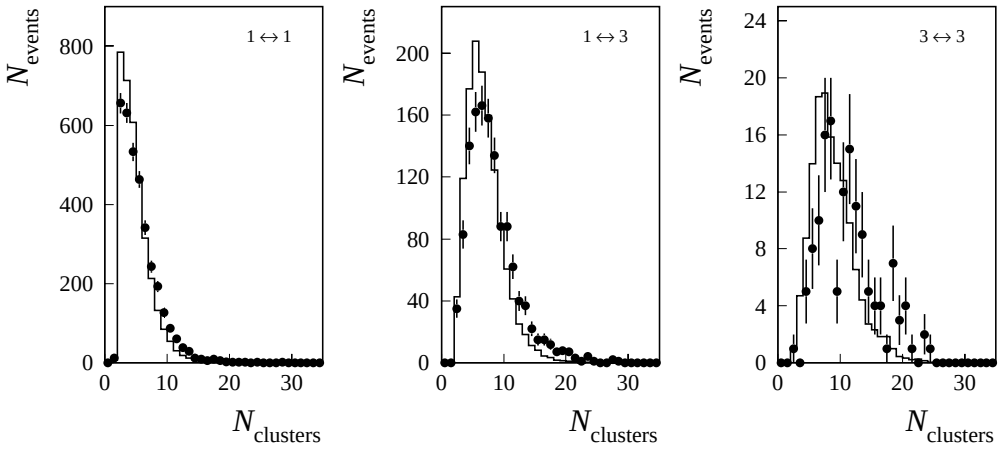

Figure 4.14 Distribution of the number of electromagnetic clusters for $1 \leftrightarrow 1$ prong, $1 \leftrightarrow 3$ prong and $3 \leftrightarrow 3$ prong sub samples, for data (points) and Monte Carlo (histogram).

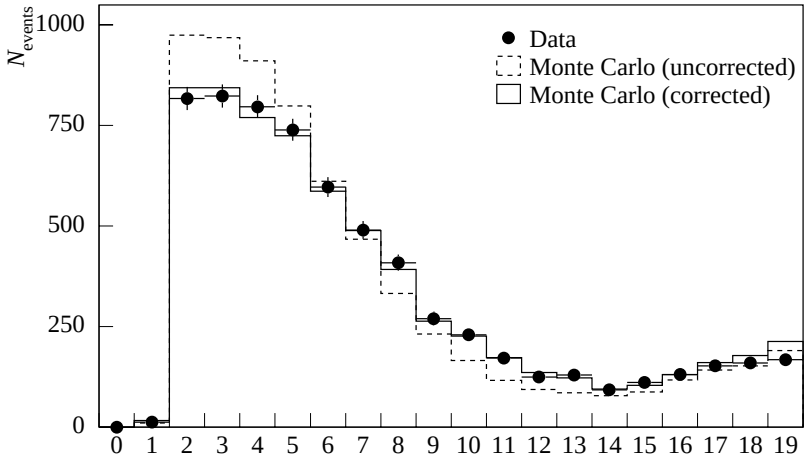

Figure 4.15 Distribution of the number of electromagnetic clusters for data (points) compared to the uncorrected Monte Carlo (dashed histogram) and corrected Monte Carlo (solid histogram). The corrected Monte Carlo prediction uses the data distributions shown in figure 4.14.

4.5 Trigger efficiency

For determining the trigger efficiency, the cross section sample is divided in two sub samples: events with a muon and events without a muon. Events with a muon can be triggered by one

	energy trigger $\varepsilon_{\mathrm{e}}(\%)$	track trigger $\varepsilon_{\mathrm{t}}(\%)$	muon trigger $\varepsilon_{\mathrm{m}}(\%)$
1990			
Events with muon	95.38 ± 0.88	82.95 ± 1.59	92.36 ± 1.12
Events without muon	99.59 ± 0.14	83.33 ± 0.84	
1991			
Events with muon	96.95 ± 0.43	88.87 ± 0.79	92.24 ± 0.67
Events without muon	99.53 ± 0.09	88.31 ± 0.44	

Table 4.2 Trigger efficiencies for various triggers for events with and without a muon for 1990 and 1991 data samples.

of the following independent triggers (see section 2.10):

- Muon trigger
- Energy trigger
- Track trigger

Events without a muon can be triggered by the following independent triggers:

- Energy trigger
- Track trigger

For the 1990 data the trigger efficiency is determined as follows. Of the 2564 events, 563 events have an isolated muon, 1974 have no muon and 27 events were in a run where the trigger information was not valid. Of the 563 events with a muon, 26 don't set the energy trigger, 96 don't set the track trigger and 43 don't set the muon trigger. Of the other 1974 events, 8 have not been triggered by the energy trigger and 329 have not been triggered by the track trigger. The resulting efficiencies for the various triggers for the 1990 data are listed in table 4.2, together with the numbers for the 1991 data, which were extracted in the same way. The energy trigger is found to be very efficient for tau pair events, even though the events may have energies of only a few GeV. The (single) muon trigger is not extremely efficient. This is partly due to the fact that the selection presented here imposes no requirements on the number of Z-segments that a muon should have, whereas the single muon trigger requires at least three out of four chambers hit. The low trigger efficiency of the track trigger can be partly explained by the fact that runs with problems in the data acquisition or reconstruction for the TEC were not removed from the cross section sample.

If the number of events with and without a muon is denoted as N^{m} and N^{t}, respectively, then the combined trigger efficiency $\varepsilon_{\mathrm{trig}}$, assuming the triggers are independent, follows from

the relation:

$$\varepsilon_{\mathrm{trig}} = \frac{N^{\mathrm{m}}}{N^{\mathrm{m}}+N^{\mathrm{t}}}\{1-(1-\varepsilon_{\mathrm{m}}^{\mathrm{m}})(1-\varepsilon_{\mathrm{e}}^{\mathrm{m}})(1-\varepsilon_{\mathrm{t}}^{\mathrm{m}})\}+ \tag{4.8}$$

$$\frac{N^{\mathrm{t}}}{N^{\mathrm{m}}+N^{\mathrm{t}}}\{1-(1-\varepsilon_{\mathrm{e}}^{\mathrm{t}})(1-\varepsilon_{\mathrm{t}}^{\mathrm{t}})\} \tag{4.9}$$

$$\tag{4.10}$$

Substituting the numbers from table 4.2 yields:

$$\varepsilon_{\mathrm{trig}} = \begin{cases} (99.93\pm0.02)\% & \text{for 1990 data} \\ (99.97\pm0.01)\% & \text{for 1991 data} \end{cases}$$

The cross section has been corrected for the trigger inefficiency.

4.6 Cross section

The total cross section for $\mathrm{e}^+\mathrm{e}^- \to \tau^+\tau^-(\gamma)$ is determined from:

$$\sigma = \frac{N_{\mathrm{sel}}}{\varepsilon\mathcal{L}} \tag{4.11}$$

with N_{sel} the number of selected events, $\mathcal{L}$ the time integrated luminosity and ε the combined efficiency of the detector and event selection. The efficiency ε can be written in the following way:

$$\varepsilon = \varepsilon_\tau + \varepsilon_{\mathrm{bg}}$$

with

$$\varepsilon_\tau = \frac{N^{\mathrm{MC}}_{\mathrm{sel},\tau}}{N^{\mathrm{MC}}_{\mathrm{tot},\tau}}$$

the selection efficiency, or the ratio of the selected number of tau pair Monte Carlo events and the total number of tau pair Monte Carlo events. The efficiency of the selection for background events, $\varepsilon_{\mathrm{bg}}$, normalized to the tau channel is:

$$\varepsilon_{\mathrm{bg}} = \sum_i \frac{N^{\mathrm{MC}}_{\mathrm{sel},\mathrm{bg}_i}}{N^{\mathrm{MC}}_{\mathrm{tot},\mathrm{bg}_i}} \cdot \frac{\sigma^{\mathrm{MC}}_{\mathrm{bg}_i}}{\sigma^{\mathrm{MC}}_\tau}$$

$$= \sum_i \frac{N^{\mathrm{MC}}_{\mathrm{sel},\mathrm{bg}_i}}{\sigma^{\mathrm{MC}}_\tau \mathcal{L}^{\mathrm{MC}}_{\mathrm{bg}_i}}$$

where the summation runs over the Z^0 background processes:

$$\mathrm{e}^+\mathrm{e}^- \to \mathrm{e}^+\mathrm{e}^-,\ \mu^+\mu^-,\ q\bar{q}$$

Process	Generator	N_{events}	ε_τ (%)	$\varepsilon_{\mathrm{bg}_i}/\varepsilon_\tau$ (%)
1990				
$\mathrm{e^+e^-} \to \tau^+\tau^-$	KORALZ 3.7 [38]	$27,494$	45.57 ± 0.30	
$\mathrm{e^+e^-} \to \mathrm{e^+e^-}$	BABAMC [39, 40]	$30,000$		0.80 ± 0.07
$\mathrm{e^+e^-} \to \mu^+\mu^-$	KORALZ 3.7	$17,000$		0.78 ± 0.10
$\mathrm{e^+e^-} \to q\bar{q}$	JETSET 7.2 [41]	$151,731$		1.34 ± 0.20
$\mathrm{e^+e^-} \to \mathrm{e^+e^-}f\bar{f}$	DIAG36 [42]	$10,000$		0.44 ± 0.31
1991				
$\mathrm{e^+e^-} \to \tau^+\tau^-$	KORALZ 3.7	$207,521$	45.69 ± 0.11	
$\mathrm{e^+e^-} \to \mathrm{e^+e^-}$	BABAMC	$28,000$		0.37 ± 0.05
$\mathrm{e^+e^-} \to \mu^+\mu^-$	KORALZ 3.7	$49,989$		0.99 ± 0.06
$\mathrm{e^+e^-} \to q\bar{q}$	JETSET 7.2	$594,190$		0.76 ± 0.08
$\mathrm{e^+e^-} \to \mathrm{e^+e^-}f\bar{f}$	DIAG36	$59,968$		0.69 ± 0.11

Table 4.3 Monte Carlo generators used for the different physics channels.

$N^{\mathrm{MC}}_{\mathrm{tot},\mathrm{bg}_i}$ and $N^{\mathrm{MC}}_{\mathrm{sel},\mathrm{bg}_i}$ are the total and selected number of events in the Monte Carlo simulation for process i. $\mathcal{L}^{\mathrm{MC}}$ and σ^{MC} are the luminosity and the cross section corresponding to the number of generated events.

The non Z^0 background has to be accounted for in a different way. Although the two photon process is s-dependent it varies only a few percent over the range of the energy points scanned around the Z^0 peak. The two photon events will be present in the sample with a rate proportional to the luminosity. Cosmic rays however, will have a rate proportional to the integrated time of data taking. Assuming the collider performed on average equally well at each of the energy points where data were taken, the time integrated luminosity $\mathcal{L}$ is proportional to the data taking time. At each energy point the number of cosmic ray and two photon events can then be subtracted using the luminosity as a weight. The total background of cosmic ray events in the tau pair sample was estimated by using additional selection requirements in order to obtain events that were likely to originate from cosmic rays. They were requirements on the TEC track vertex, the scintillator time and the number of muons (not necessarily in an ASJT). By scanning the thus selected events, the background from cosmic rays was estimated to be (0.2 ± 0.1)%.

The various Monte Carlo event generation programs used for determining the efficiency are listed in table 4.3, together with the number of generated events for each channel. The fourth column shows the efficiency of the selection code for tau pair events (ε_τ). This is the overall efficiency, including the geometrical acceptance. The efficiency within the fiducial volume is (74.8 ± 0.2)% averaged for 1990 and 1991. The last column in the table shows the fraction of background events in the selected tau sample. The fraction of two photon events is valid only on the Z^0 peak. The relative off-peak contribution will be larger.

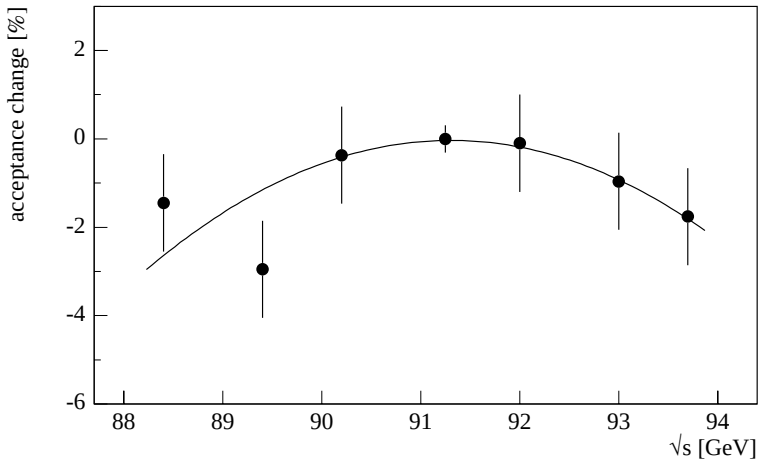

Figure 4.16 Relative acceptance as function of the center of mass energy. The line shows a parabola fit through the points.

The dependence of the acceptance on $\sqrt{s}$ has been checked by simulating an additional 10,000 tau pair events for each of six off-peak energy points. The relative change in acceptance for these points is plotted in figure 4.16, together with a fitted parabola. The cross section calculated at each point has been corrected for this dependence.

Table 4.4 and figure 4.17 show the results of the $\mathrm{e^+e^-} \to \tau^+\tau^-(\gamma)$ cross section measurement for the 1990 and 1991 data taking periods. The cross sections have been extrapolated to the full solid angle for each center of mass energy. Figure 4.17 also shows the result of a fit to these data points, which will be described in chapter 6.

$\sqrt{s}$ (GeV)	N_{events}	$\mathcal{L}(\mathrm{nb}^{-1})$	$\sigma_{\tau^+\tau^-}$ (nb)
1990			
88.232	36	337.8	0.218 ± 0.036
89.235	86	404.7	0.444 ± 0.048
90.237	138	319.9	0.910 ± 0.077
91.230	1887	2721.3	1.468 ± 0.034
92.227	190	366.3	1.096 ± 0.080
93.228	133	472.2	0.591 ± 0.051
94.223	94	477.4	0.411 ± 0.042
Total	2564	5099.6	
1991			
88.480	95	782.9	0.254 ± 0.026
89.469	204	851.1	0.506 ± 0.035
90.228	331	794.3	0.884 ± 0.049
91.242	5482	7864.5	1.481 ± 0.020
91.967	395	690.2	1.216 ± 0.061
92.966	235	759.2	0.656 ± 0.043
93.716	208	830.9	0.534 ± 0.037
Total	6950	12573.1	

Table 4.4 Number of events and cross sections for the various energy points for 1990 and 1991 data. The cross sections have been extrapolated to the full solid angle and the quoted errors are statistical only.

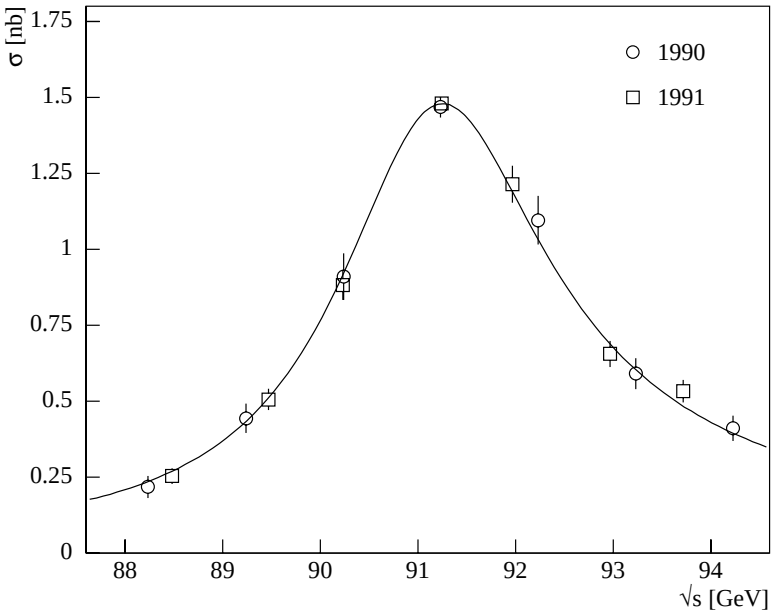

Figure 4.17 Measured tau pair cross section as a function of the center of mass energy. The line drawn is the result of a fit described in chapter 6.

4.7 Systematic errors

The contribution to the systematic errors due to the event selection is estimated by varying the values for each of the cuts within a reasonable range. The range is determined by the distribution of the events around the default value and by the physical meaning of the cut.

Figure 4.18 (top) shows the distribution of the polar angle of the event thrust axis. The plot shows the distribution of tau events that were selected by applying all selection cuts listed in section 4.3, except for the cut on $|\cos\theta_{\rm thr}|$. The points represent the number of selected events per bin and the error bars indicate the (statistical) errors on these points. The gray histogram shows the distribution of the background Monte Carlo events: $\mathrm{e^+e^-} \to \mathrm{e^+e^-}$, $\mu^+\mu^-$, $q\bar{q}$ and two-photon background ($\mathrm{e^+e^-} \to \mathrm{e^+e^-e^+e^-}$, $\mathrm{e^+e^-}\mu^+\mu^-$, $\mathrm{e^+e^-}\tau^+\tau^-$, $\mathrm{e^+e^-u\bar{u}}$). The solid line is the histogram of all Monte Carlo events, so the background plus the $\mathrm{e^+e^-} \to \tau^+\tau^-$

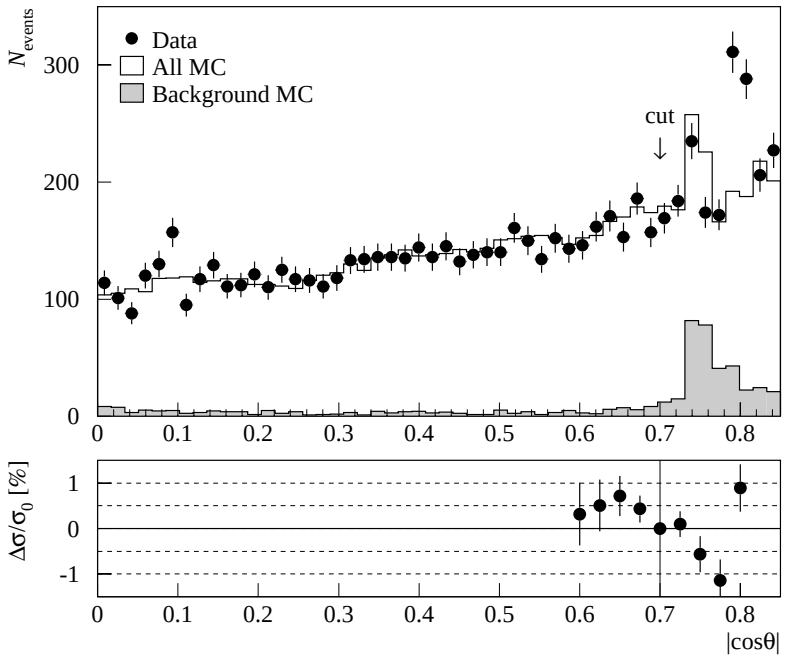

Figure 4.18 Angular distribution of the tau pair events (top). All selection criteria have been applied, except for the cut on $|\cos\theta_{\rm thr}|$. This cut value is indicated with an arrow. The relative change in the cross section resulting from a variation of fiducial volume is shown in the lower plot. The error bars shown in this plot reflect the statistical significance of the change.

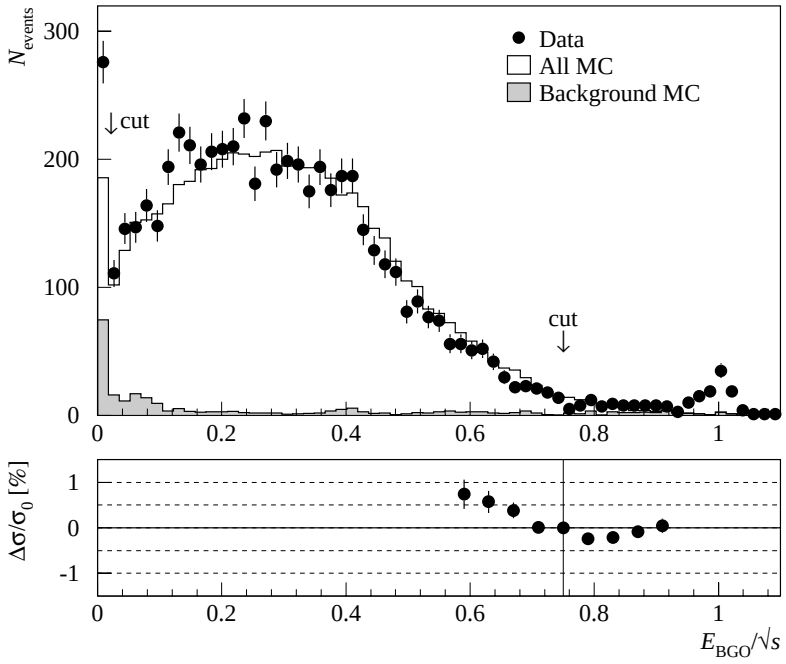

Figure 4.19 Energy distribution in the electromagnetic calorimeter. Both cuts applied are indicated with an arrow.

events[§]. The cut value (indicated with an arrow) is chosen such that the selected events lie well within the BGO barrel region. Up to the cut value the background is low and evenly distributed, but further forward the background increases. The peak at $|\cos\theta| \simeq 0.75$ is due to events in the gap between the barrel and endcap of the ECAL (see also figure 2.4 on page 18). The Monte Carlo does not describe the data very well in that region.

The bottom plot of figure 4.18 and subsequent figures in this chapter, show the relative change in the cross section when varying the cut value over the range indicated. The error bars on the points represent the statistical errors on the difference in the number of events ($\sqrt{|N - N'|}/N$), when going from the central cut value (accepting N events) to the one indicated (accepting N' events). This indicates to what extend the variations might be statistical. Inside the barrel region ($|\cos\theta| < 0.74$) the calculated cross section is quite stable. A systematic error of 0.5% is assigned to this cut.

Figure 4.19 (top) shows the distribution of the total electromagnetic energy. The data and

[§]It has to be noted that in figure 4.18, and in subsequent figures in this chapter, the Monte Carlo distributions are obtained using predicted cross sections and the measurement of the integrated luminosity. The Monte Carlo distributions have not been normalized to the number of data events.

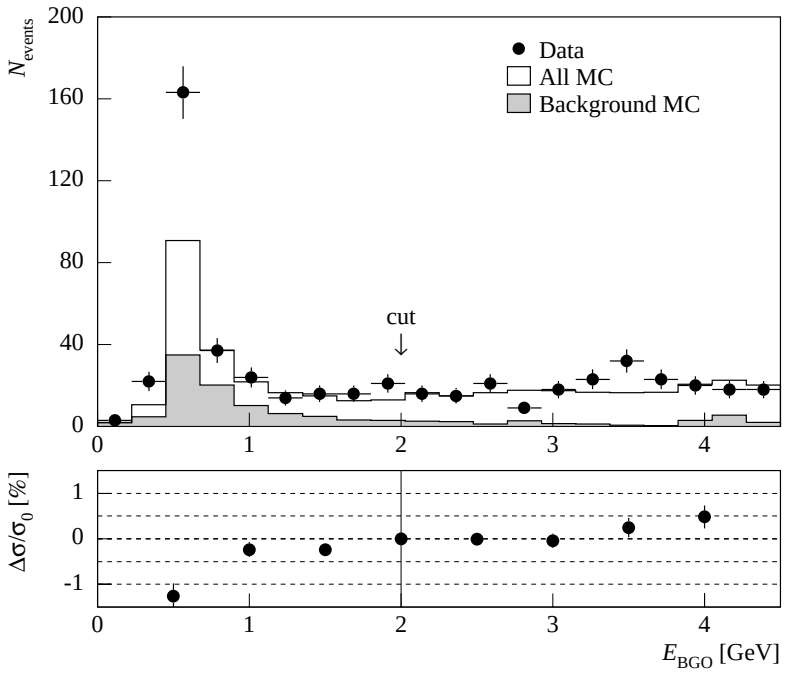

Figure 4.20 Low energy distribution in the electromagnetic calorimeter. The cut applied is indicated with an arrow.

Monte Carlo agree very well, except for the peaks in the data at the high side and the low side of the spectrum.

The peak on the high side comes from Bhabha scattering events ($e^+e^- \to e^+e^-(\gamma)$) that were not completely removed from the data by the cut on the energy of each electron separately (criterion (9) on page 55). These are Bhabha events where both jets have not been classified as electrons by the reconstruction software. The cut is far away from this peak. The relative change in cross section, when varying the cut value over the range shown is indicated in the bottom plot of figure 4.19. The systematic error introduced by this cut is estimated to be 0.3%.

An enlarged view of the low end of the BGO energy spectrum is shown in figure 4.20. The peak comes from dimuon and cosmic ray events (cf. figure 2.5 on page 18). The discrepancy is due mainly to the cosmic ray events which are not simulated in Monte Carlo. Since also this cut is well away from the peak and the variation of cross section is very small, no significant contribution to the systematic error is expected due to this cut.

The distribution of the number of ECAL bumps is shown in figure 4.21. The Monte Carlo distribution has been corrected, as discussed in section 4.4. In order to determine the contribution to the systematic error originating from the cut on the number of bumps the cut

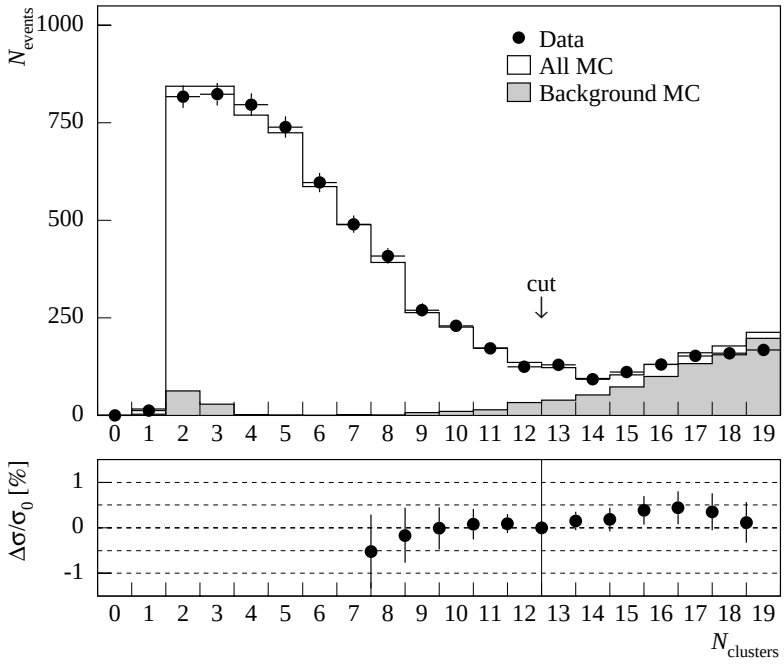

Figure 4.21 Distribution of the number of electromagnetic clusters for data (points) and Monte Carlo (histogram), using the data distributions shown in figure 4.14 for the tau Monte Carlo.

value is varied. The resulting effect on the cross section is very small, as is indicated in the lower plot of figure 4.21. Besides varying the cut value, two additional checks were made to ensure that the modified Monte Carlo describes the data well in the region around the cut value. As a first check, the sample is divided in two equally large sub samples. The first sample has a low total energy ($E_{\text{raw}}^{\text{tot}} < 40$ GeV) and is likely to contain all background except the hadronic background. The second sample has a high total energy ($E_{\text{raw}}^{\text{tot}} > 40$ GeV) and the background consists almost entirely of hadronic events. The difference in peak cross section for both sub samples agrees with the central cross section value to better than 1%, which is well within the allowed statistical fluctuation. The second check involves a cut on the maximum angle between any track in a jet and the central jet axis. This angle is required to be less than 15°. The hadronic background reduces from about 0.8% to 0.3% of the total selected sample. Also the hadronic two photon background is reduced. The change in cross section resulting from this extra cut is 0.2%.

After correction the Monte Carlo bump distribution describes the data very well, also in the region of overlap with the hadron events. From the variation of the cut value and from the

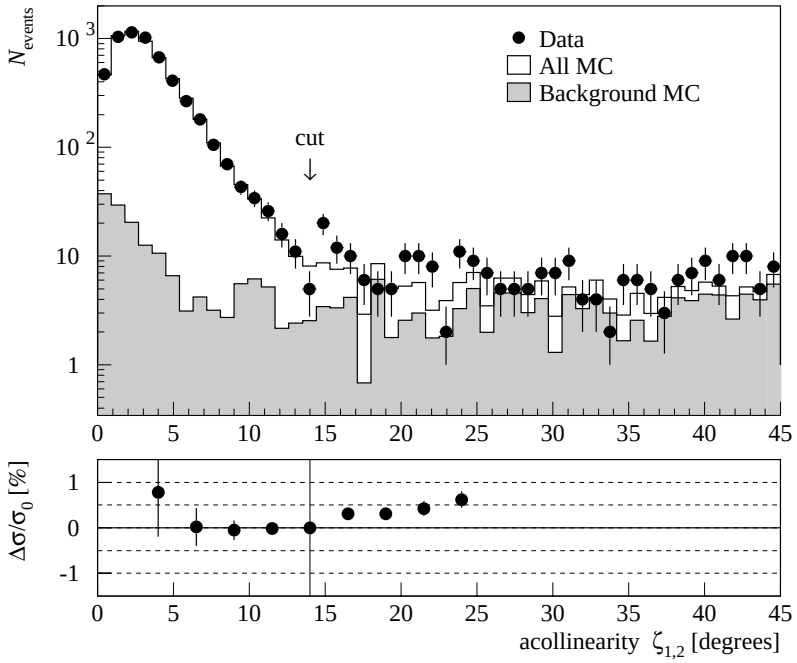

Figure 4.22 Logarithmic plot of the acollinearity angle distribution (top) and the relative change in cross section when varying the central cut value (bottom).

additional checks, a systematic error of 0.2% is assigned to this cut.

The second cut on the event multiplicity, requiring the number of charged tracks in the TEC to be less than 9, mainly reduces the hadronic background. A global inefficiency of the TEC of 8% has been taken into account in all Monte Carlo simulations, roughly corresponding to one non working TEC sector. Varying this inefficiency between 4–12% showed a negligible effect on the tau pair cross section.

Figure 4.22 shows a logarithmic plot for the distribution of the acollinearity angle $\zeta_{1,2}$ between the two most energetic jets in each event. For tau pair events this angle is on average about three degrees. The tail of the distribution contains the radiative events and the two photon events. In addition, cosmic ray events that happen to be in time with the beam crossing and look like two- or three-jet events, are in general not back to back and will be removed by this cut on the acollinearity angle (see also the event shown in figure 4.11). The lower plot in figure 4.22 again shows the cross section variation due to a change in the cut value. This variation is small and the contribution to the systematic error due to this cut is estimated to be 0.2%.

The energy spectrum for electrons is well simulated by Monte Carlo (figure 4.23). Shown

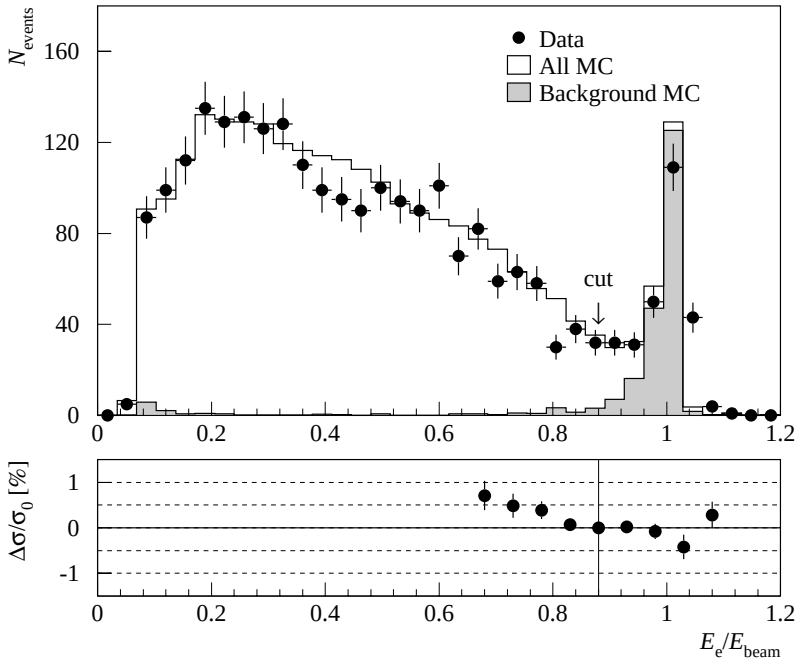

Figure 4.23 Distribution of the electromagnetic energy for recognized electrons (top). The bottom plot shows the relative change in cross section due to the indicated variation of the cut value.

in this plot is the electromagnetic energy of each ASJT consisting of a single electron or an electron in a jet. Data and Monte Carlo are in good agreement and a systematic error of 0.2% is assigned to this cut.

Figure 4.24 shows the momentum distribution for ASJT's that were classified as an isolated muon. The distributions for data and Monte Carlo agree well and the contribution to the systematic error due to this cut is estimated to be 0.2%.

Table 4.5 lists the main contributions to the systematic error due to the event selection. The total systematic error was obtained by adding these contributions in quadrature. Since the 1990 and 1991 event selections differ only in minor details, the same error is assigned to both samples.

Table 4.6 summarizes the main contributions to the systematic error on the cross section measurement. The contribution for the acceptance reflects not only the Monte Carlo statistics but includes a 0.25% effect originating from the uncertainty on the tau branching fractions [45]. An overall systematic error on the luminosity measurement of 0.6% [9] has not been included.

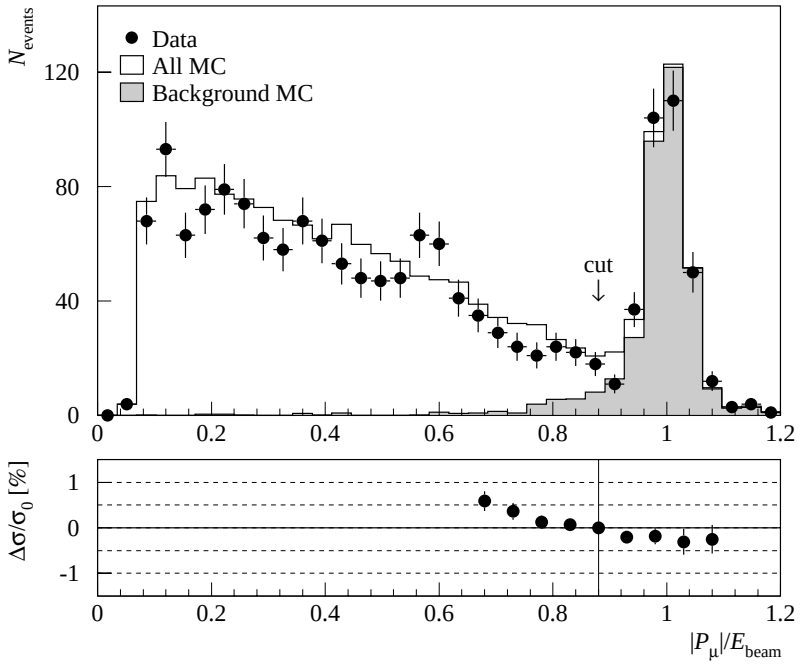

Figure 4.24 Distribution of the muon momentum for recognized isolated muons (top). The bottom plot shows the relative change in cross section due to the indicated variation of the cut value.

Selection Criterion		Systematic Error (%)
Fiducial volume	$\lvert\cos\theta_{\rm thr}\rvert < 0.7$	0.5
Electromagnetic energy	$E_{\rm BGO}/\sqrt{s} < 0.75$	0.3
Multiplicity	$N_{\rm cluster} < 13$	0.2
Acollinearity angle	$\zeta_{1,2} < 14^\circ$	0.2
Muon momentum	$P_\mu/\sqrt{s} < 0.88$	0.2
Electron energy	$E_{\rm e}/\sqrt{s} < 0.88$	0.2
Total		0.7

Table 4.5 Systematic errors in cross section measurement due to the event selection. These errors are assumed to be the same for the 1990 and 1991 data.

source	systematic error (%)	
	1990	**1991**
Acceptance (MC)	0.39	0.27
Background subtraction (MC statistics)	0.39	0.17
Cosmic background subtraction	0.1	0.1
Event selection	0.7	0.7
Total	0.90	0.78

Table 4.6 Summary of systematic errors in cross section measurement. An overall systematic error of 0.6% on the measurement of the luminosity has not been included.

Chapter 5

Forward-backward charge asymmetry

In this chapter the measurement of the tau pair forward-backward charge asymmetry $A_{\rm FB}$ is described. A short introduction is given in section 5.1. Section 5.2 describes the event selection and in section 5.3 the problem of the charge confusion is discussed. Background subtraction and systematic error estimates are described in section 5.4. In section 5.5 three methods of determining the asymmetry are described, and the final values and a comparison with the standard model predictions are presented.

5.1 Introduction

The forward-backward charge asymmetry $A_{\rm FB}$ is defined as (see also section 1.3):

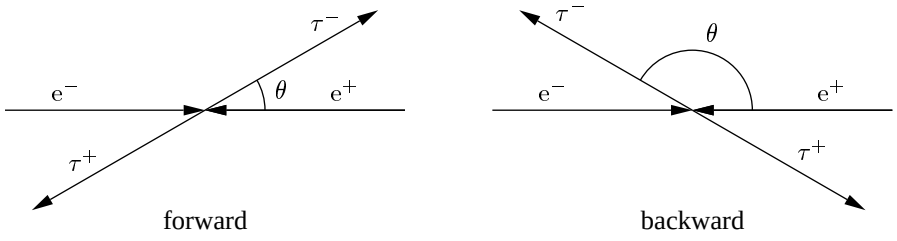

Figure 5.1 Definition of the polar angle θ between the incoming e^- and the outgoing τ^- for forward and backward events.

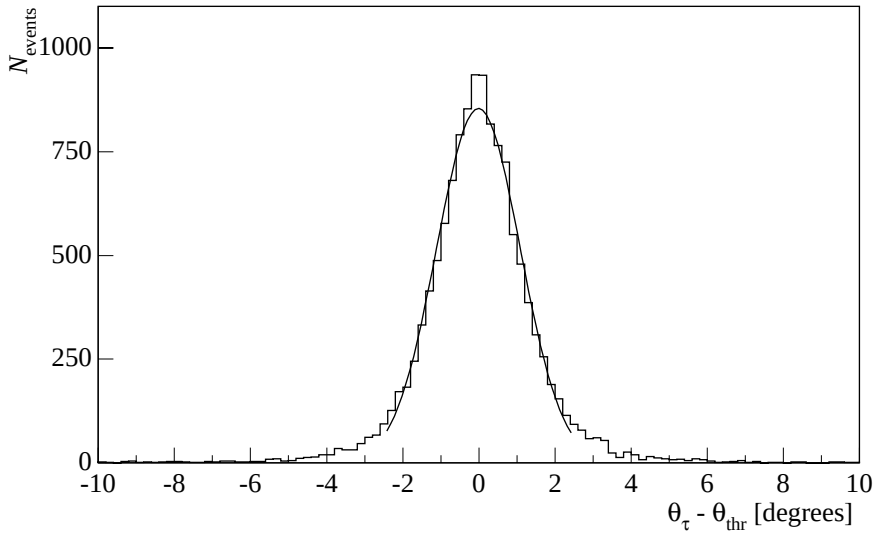

Figure 5.2 Difference in polar angle θ between the generated tau direction (θ_τ) and the reconstructed thrust axis direction ($\theta_{\rm thr}$).

$$A_{\rm FB} \equiv \frac{\sigma_{\rm F} - \sigma_{\rm B}}{\sigma_{\rm F} + \sigma_{\rm B}} \tag{5.1}$$

where

$$\sigma_{\rm F} = \int_0^1 {\rm d}(\cos\theta)\frac{{\rm d}\sigma}{{\rm d}\cos\theta}; \quad \sigma_{\rm B} = \int_{-1}^0 {\rm d}(\cos\theta)\frac{{\rm d}\sigma}{{\rm d}\cos\theta} \tag{5.2}$$

$\sigma_{\rm F}$ and $\sigma_{\rm B}$ being the cross sections in the forward and backward direction respectively, with the polar angle θ defined as shown in figure 5.1.

Since θ_τ cannot be measured directly, the direction of event thrust axis is used. The direction of the event thrust axis corresponds very well to the original τ direction, as can be seen from figure 5.2. The plot shows, for Monte Carlo events, the difference between the polar angle of the generated tau direction and the polar angle of the reconstructed event thrust axis. The distribution is symmetric around zero and its width is 1.1°.

5.2 Event selection

The data sample used for determining the forward-backward charge asymmetry is the same as used for the cross section, described in chapter 4. There are however some additional requirements, since the charge of the taus has to be determined.

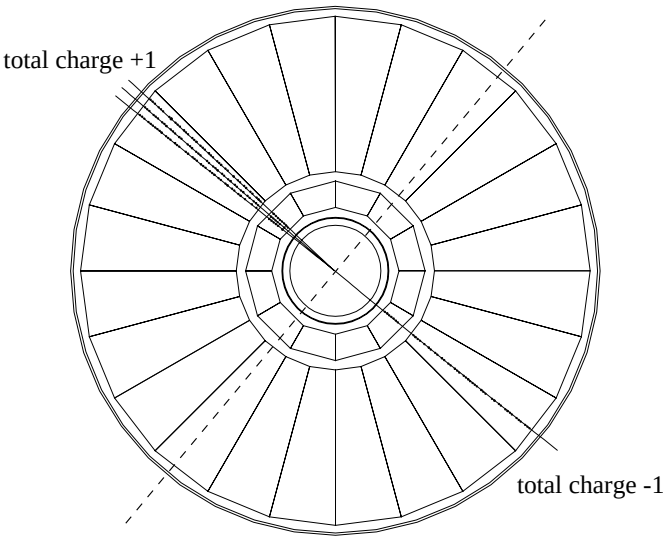

Figure 5.3 Determination of the tau charge from measuring the total charge of the decay products. The dashed line is the line perpendicular to the projected event thrust axis and divides the event in two halves.

The charge of the τ cannot be measured directly. In order to extract the tau charge, the charges of the decay products of each of the taus are summed. If one of the taus in an event decays into a muon plus neutrinos, the muon charge as measured accurately in the muon spectrometer is used. However, only about 32% of the tau pairs decay into one or two muons, and this percentage even drops to 23% as a result of the event selection.

In order to determine tau charges for the remaining events, the charged tracks as measured by the TEC are used. All the good TEC tracks in an event, i.e. those tracks that satisfy the requirements listed in section 2.3 on page 17, are used.

After identifying the good tracks, the event is divided in two halves in the transverse plane, the separation determined by the line perpendicular to the projection of the event thrust axis onto this plane, as is shown in figure 5.3. The charge of the taus is then determined by summing the charges of each of the tracks on either side of the dashed line.

5.3 Charge confusion

Having two opposite charges in one event enables the determination of the charge confusion. If only those events are preselected that have $+1$ or -1 total charge on either side, two groups of events can be distinguished. The opposite sign events ($+1 \leftrightarrow -1$) and the like sign events ($+1$

$\leftrightarrow +1$ or $-1 \leftrightarrow -1$). Let ζ be the fraction of the taus (per side) that change sign from $+1$ to -1 or vice versa. The number of opposite sign events, N_{+-}, and like sign events, $N_{++} + N_{--}$, is then given by:

$$N_{+-} = N(1 - 2\zeta + 2\zeta^2) \tag{5.3}$$

$$N_{++} + N_{--} = N(2\zeta - 2\zeta^2) \tag{5.4}$$

where $N = N_{+-} + N_{++} + N_{--}$, the total number of events. The fraction ξ of charge confused events in the used sample, i.e. the events where both sides have changed sign and look like good events, will then be:

$$\xi = \frac{N\zeta^2}{N(1 - 2\zeta + 2\zeta^2)} = \frac{1}{2} - \frac{\frac{1}{2}\sqrt{N^2 - 2N(N_{++} + N_{--})}}{N - N_{++} - N_{--}} \tag{5.5}$$

where the fraction ξ can be derived directly from the total number of events and the number of like sign events. The asymmetry is reduced because of the charge confusion. If, for instance, the charge asymmetry is positive (i.e. there are more forward than backward events), there will be more forward events becoming backward, than backward events becoming forward, thereby reducing the asymmetry. So, the measured number of forward events N'_{F} is not equal to the real number of forward events N_{F}:

$$N'_{\mathrm{F}} = (1 - \xi)N_{\mathrm{F}} + \xi N_{\mathrm{B}} \tag{5.6}$$

If now the asymmetry A'_{FB} is determined, one finds:

$$A'_{\mathrm{FB}} = \frac{N'_{\mathrm{F}} - N'_{\mathrm{B}}}{N'_{\mathrm{F}} + N'_{\mathrm{B}}} = \frac{N_{\mathrm{F}} - N_{\mathrm{B}}}{N_{\mathrm{F}} + N_{\mathrm{B}}}(1 - 2\xi) \tag{5.7}$$

so the asymmetry is reduced by a factor $(1 - 2\xi)$ because of the charge confusion.

In order to determine the wrong charge assignment for the events containing a muon, a sub set of events from the combined 1990 and 1991 data sample that have the charge determined both from the TEC and from the muon chambers is used. For the TEC tracks the most strict requirements are applied: all tracks should be more than 15 mrad away from the wire plane and the charge should be ± 1 on either side. There are 4441 events satisfying these requirements, 419 of which are like sign events ($+1 \leftrightarrow +1$ or $-1 \leftrightarrow -1$). This gives a fraction of charge confused events, according to (5.5), of $\xi = 0.27\%$. Out of the 4022 opposite sign events, 858 contain an isolated muon. For 7 events out of these, the charges determined from TEC and from the muon chambers do not agree. From these numbers a fraction of wrongly assigned charge to the muon tracks of $\zeta_\mu \simeq (7 - 858 \cdot 0.27\%) / 858 = (0.55 \pm 0.3)\%$ is extracted. The asymmetry is later corrected for the relative contribution of this charge confusion.

Since the error on the asymmetry is still dominated by statistics, the number of usable events is now increased by loosening the requirements on the charges of the tracks in an event. Instead of demanding that the total charge on one side is $+1$ and -1 on the other, now all

events that satisfy that the total charge on one side is positive and not positive on the opposite side, and events that have negative total charge on one and not negative on the opposite side are accepted. So instead of allowing only $-1 \leftrightarrow +1$ topologies, all events with charges satisfying $>0 \leftrightarrow \leq 0$ and $<0 \leftrightarrow \geq 0$ will now be accepted. In this case the charge confusion relation (5.5) derived previously can no longer be used. While it is still approximately correct for events with $> 0 \leftrightarrow <0$ it is no longer valid for the events with $>0 \leftrightarrow 0$ and $<0 \leftrightarrow 0$. In those cases only one side of the event determines the charge, hence the charge confusion will be much larger. Equation (5.5) is now used to obtain the value for the one side charge confusion ζ and the asymmetry is corrected for the weighted sum of these contributions to the total charge confusion. Using the above selection, 8262 events survive for the combined 1990 and 1991 data sample. Out of these, 8099 have the charge determined on both sides using the TEC. Of these events 1246 are like sign, resulting in $\xi = (0.83 \pm 0.05)\%$ and $\zeta = (8.4 \pm 0.2)\%$. For 1106 events only one side of the TEC can be used and there are 1899 events containing an isolated muon. If an event contains a muon, the charge as determined from the muon chambers is used. The resulting average charge confusion is $(1.6 \pm 0.1)\%$.

5.4 Background and systematic errors

As is shown in the previous section, the measured asymmetry is reduced by a factor $(1-2\xi)$ because of the charge confusion. The estimated value for ξ is $(1.6 \pm 0.1)\%$. The correction of this charge confusion therefore introduces a systematic error of $2 \times 0.1\%$ or $2 \cdot 10^{-3}$.

The contribution to the asymmetry from background sources with a known asymmetry can easily be subtracted from the measured asymmetry. Let the measured asymmetry be $A'_{\rm FB}$ and the real asymmetry $A_{\rm FB}$. By definition the real and background asymmetries are:

$$A_{\rm FB} = \frac{N_{\rm F} - N_{\rm B}}{N_{\rm F} + N_{\rm B}}; \quad A^{\rm b}_{\rm FB} = \frac{N^{\rm b}_{\rm F} - N^{\rm b}_{\rm B}}{N^{\rm b}_{\rm F} + N^{\rm b}_{\rm B}} \tag{5.8}$$

We measure:

$$A'_{\rm FB} = \frac{N_{\rm F} - N_{\rm B} + N^{\rm b}_{\rm F} - N^{\rm b}_{\rm B}}{N_{\rm F} + N_{\rm B} + N^{\rm b}_{\rm F} + N^{\rm b}_{\rm B}} = (1-\delta)A_{\rm FB} + \delta A^{\rm b}_{\rm FB} \tag{5.9}$$

or

$$A_{\rm FB} - A'_{\rm FB} = \delta(A_{\rm FB} - A^{\rm b}_{\rm FB}) \tag{5.10}$$

where

$$\delta = \frac{N^{\rm b}_{\rm F} + N^{\rm b}_{\rm B}}{N_{\rm F} + N_{\rm B} + N^{\rm b}_{\rm F} + N^{\rm b}_{\rm B}} \tag{5.11}$$

the fraction of background events in the selected sample. Equation (5.9) can be written as:

$$A_{\rm FB} = \frac{A'_{\rm FB} - \delta A^{\rm b}_{\rm FB}}{1-\delta} \tag{5.12}$$

and this expression can be used to subtract the background asymmetry.

The asymmetry of cosmic rays has been measured to be $(1.4 \pm 1.8)\%$ [46]. The cosmic ray background in the sample is estimated to be 0.2% so the maximum error due to this background follows from (5.10) and is about $5 \cdot 10^{-4}$.

For the background from the Bhabha process ($e^+e^- \rightarrow e^+e^-$), the theoretical predictions for the charge asymmetry from the ALIBABA program [47, 22] is used and this contribution is subtracted using (5.12). The maximum correction is about $4 \cdot 10^{-3}$ and the systematic error due to this subtraction is estimated to be about 20% of the correction, or $1 \cdot 10^{-3}$.

The background from dimuons ($e^+e^- \rightarrow \mu^+\mu^-$) is expected to have the same charge asymmetry as the tau events. Previous measurements have confirmed this expectation [24] and the dimuon background is not corrected for.

The contribution of the hadronic background to the asymmetry can be estimated as follows. Not all the TEC tracks in a hadronic event are well reconstructed. If a random set of tracks is left out, half of the events are expected to show up in the asymmetry data sample, because the other half are like sign events. The asymmetry of the accepted opposite sign events can be expected to be zero on average, since the event charge assignment is based on a random set of tracks. The hadronic background in the asymmetry sample is estimated to be 0.45% averaged for the 1990 and 1991 data sample. The same argument holds for the hadronic two photon background, which is about half of the total two photon background. This background is estimated to be 0.2% averaged for the 1990 and 1991 asymmetry data sample. The hadronic Z^0 and two photon background is corrected for using equation (5.12). The contribution to the systematic error coming from this correction is estimated to be about 20% of the correction, or $5 \cdot 10^{-4}$. The remaining two photon events in the sample are not corrected for, and an error of $5 \cdot 10^{-4}$ is assigned to this background.

Figure 5.4 shows the variation in the asymmetry at peak energy for the 1991 data for different values of the acollinearity cut. The errors on the points reflect the statistical significance of the change from the central value at 14° to the one indicated and these errors are calculated as follows:

$$\Delta(A'_{\mathrm{FB}} - A_{\mathrm{FB}}) = \frac{2}{N}\sqrt{\frac{\Delta N_{\mathrm{F}} \cdot \Delta N_{\mathrm{B}}}{\Delta N_{\mathrm{F}} + \Delta N_{\mathrm{B}}}} \cdot 1.25 \tag{5.13}$$

with ΔN_{F} and ΔN_{B} the change in number of forward and backward events with respect to the central values, respectively and N the total number of events at the central value. The factor 1.25 will be explained in the next section. A systematic error of $2 \cdot 10^{-3}$ is assigned to the uncertainty due to this cut.

Adding the above errors in quadrature, an estimate of the systematic error of the tau forward-backward asymmetry of $3 \cdot 10^{-3}$ is obtained.

5.5 Calculating the asymmetry

There are several methods to extract the asymmetry from the data. Three methods will be discussed here: counting, fitting the angular distribution and performing an unbinned maximum

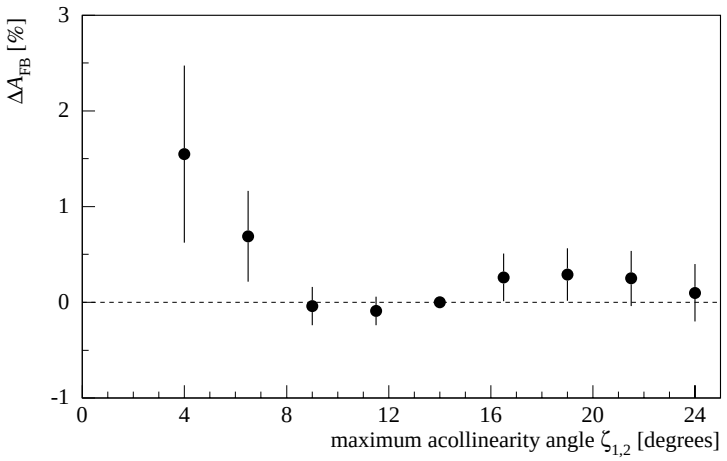

Figure 5.4 Change in forward backward asymmetry at the Z^0-peak energy, when varying the acollinearity cut value for the 1991 data sample.

likelihood fit.

Counting the number of forward and backward events

The simplest method is to count the number of forward and backward events and use equation (5.1) to extract the forward-backward charge asymmetry. However, the events selected lie in the barrel part of the detector only, $|\cos\theta| < 0.7$. The asymmetry extracted by counting the number of events is therefore reduced. If the differential cross section is assumed to have the Born form:

$$\frac{\mathrm{d}\sigma}{\mathrm{d}\cos\theta} = 1 + \cos^2\theta + \tfrac{8}{3}A_{\mathrm{FB}}\cos\theta \tag{5.14}$$

the angular expression for the cross section (5.2) can be integrated over a reduced polar range ($|\cos\theta| < \cos\theta_{\mathrm{c}}$). One obtains:

$$A_{\mathrm{FB}} = A_{\mathrm{FB}}(|\cos\theta| < \cos\theta_{\mathrm{c}}) \cdot \frac{3 + \cos^2\theta_{\mathrm{c}}}{4\cos\theta_{\mathrm{c}}} \tag{5.15}$$

which gives the following result, using the value for $\cos\theta_{\mathrm{c}} = 0.7$:

$$A_{\mathrm{FB}} = \frac{N_{\mathrm{F}} - N_{\mathrm{B}}}{N_{\mathrm{F}} + N_{\mathrm{B}}} \cdot 1.25 \tag{5.16}$$

This method is applied to the largest event sample (i.e. the sample with the loosest charge requirements). The number of forward and backward events for the different energy bins, are

$\sqrt{s}$ (GeV)	N_B	N_F	A_{FB}
1990			
88.23	19	13	-0.248 ± 0.225
89.24	36	33	-0.059 ± 0.156
90.24	66	57	-0.097 ± 0.117
91.23	787	894	0.083 ± 0.032
92.23	94	81	-0.098 ± 0.098
93.23	55	64	0.098 ± 0.119
94.22	34	47	0.209 ± 0.142
1991			
88.48	45	38	-0.112 ± 0.140
89.47	93	75	-0.140 ± 0.098
90.23	157	124	-0.153 ± 0.076
91.24	2381	2324	-0.016 ± 0.019
91.97	156	187	0.117 ± 0.069
92.97	91	105	0.092 ± 0.091
93.72	92	91	-0.008 ± 0.095

Table 5.1 Number of forward and backward events and extracted asymmetry using the counting method, extrapolated to the full angular range.

listed in table 5.1, together with the extracted value for the asymmetry, using the above relation (5.16).

Fitting the angular distribution

The second method to extract the asymmetry A_{FB} uses a χ^2 fit to the angular distribution of the tau events (5.14). The angular range in $\cos\theta$ is divided in four forward and four backward bins. Since the acceptance is different for different regions of the detector, the distribution has to be corrected for the θ dependent acceptance. In order to do this, Monte Carlo generated events were used to determine the acceptance per bin.

Figure 5.5 shows the acceptance corrected angular distribution for the on-peak tau events ($\sqrt{s} = 91.3$ GeV) and for one of the off-peak energy bins ($\sqrt{s} = 93.0$ GeV) for the 1991 data sample. The solid line represents the result of a χ^2 fit to the functional form shown in (5.14). The fit has a value of $\chi^2/N_{DOF} = 2.6/6$ for the top plot and $\chi^2/N_{DOF} = 7.7/6$ for the bottom plot. The same fit is performed also to the data in the other energy bins. All results of these fits are shown in table 5.2.

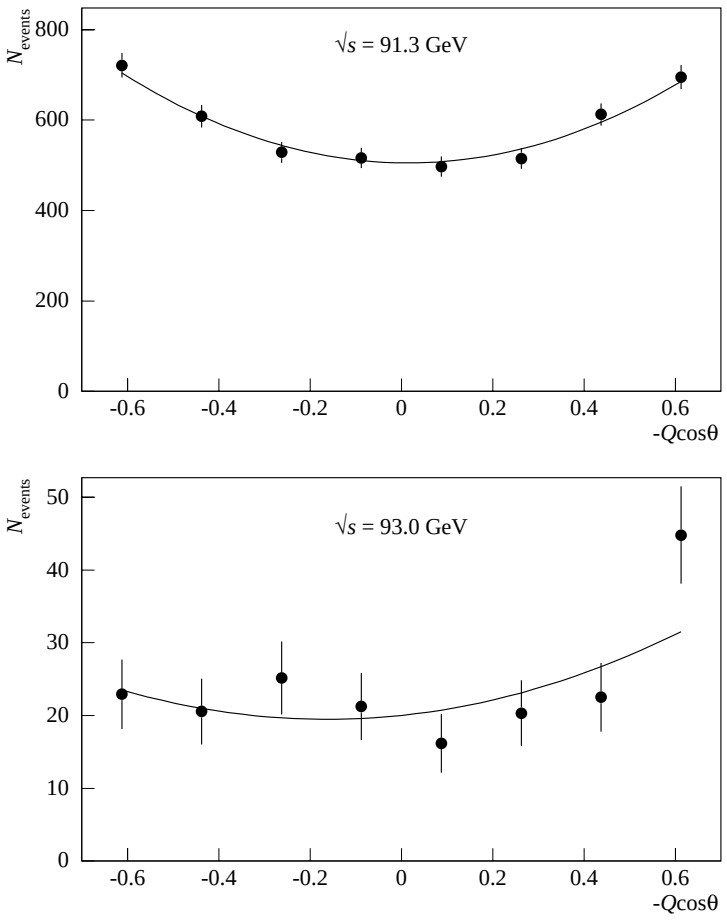

Figure 5.5 Acceptance corrected angular distribution for the on-peak tau events (top) and for one off-peak energy point (bottom). The solid line shows the least squares fit to the theoretical differential cross section. The fitted value for the charge asymmetry is $A_{FB} = -0.011 \pm 0.017$ for the top plot and $A_{FB} = 0.123 \pm 0.084$ for the bottom plot. Both distributions are for the 1991 data sample.

$\sqrt{s}$ (GeV)	A_{FB}	$\sqrt{s}$ (GeV)	A_{FB}
1990		**1991**	
88.23	-0.204 ± 0.216	88.52	-0.109 ± 0.133
89.24	-0.310 ± 0.140	89.51	-0.191 ± 0.091
90.24	-0.135 ± 0.103	90.27	-0.177 ± 0.065
91.23	0.072 ± 0.028	91.27	-0.011 ± 0.017
92.23	-0.034 ± 0.089	92.01	0.094 ± 0.061
93.23	0.011 ± 0.107	93.02	0.123 ± 0.084
94.22	0.062 ± 0.134	93.77	-0.049 ± 0.094

Table 5.2 Asymmetry A_{FB} as extracted from a χ^2 fit to the differential cross section for different energy points.

Unbinned likelihood fit

The third method is an unbinned maximum likelihood fit. The likelihood function is defined as:

$$\mathcal{L} \equiv \prod_i \left(1 + \cos^2\theta_i + \tfrac{8}{3} A_{\mathrm{FB}} \cos\theta_i\right) \tag{5.17}$$

and $-\log\mathcal{L}$ is minimized. The product runs over all selected events, where θ_i is the polar angle of the event thrust axis in the direction of the τ^-. The expression used in (5.17) corresponds to the lowest order differential cross section (cf. equation (1.5)). The event sample used for determining the asymmetry contains no events with hard bremsstrahlung photons due to the requirements on the acollinearity angle and is restricted to large angles due to the fiducial volume cut. Therefore this lowest order form can be used for the determination of the asymmetry. A comparison between this lowest order form and one with full electroweak corrections using ZFITTER shows that this is good to within 0.6%, corresponding to a systematic error of less than 0.003 in the asymmetry [24], which is negligible compared to the current statistical errors.

In using the unbinned likelihood fit, any θ dependent acceptance does not affect the result, as long as the acceptance does not depend on the charge of the particles. Furthermore, the fit behaves well even for a low number of events, as is the case in the off-peak energy bins. The unbinned maximum likelihood fit is performed to the maximum asymmetry sample, using either the muon tracks, or the TEC tracks with loose cuts, as described in section 5.3. This sample was also used for the counting method and for the χ^2 fit method and contains 2304 events for 1990 and 5959 events for the 1991 data. The results of the fits are shown in table 5.3.

As a further check, two independent sub samples are used and the asymmetry is determined for these sub samples.

$\sqrt{s}$ (GeV)	A_{FB}	A_{FB} (check 1)	A_{FB} (check 2)
1990			
88.23	-0.356 ± 0.199	-0.809 ± 0.318	-0.340 ± 0.315
89.24	-0.004 ± 0.146	0.704 ± 0.267	0.042 ± 0.244
90.24	-0.126 ± 0.106	-0.209 ± 0.219	-0.208 ± 0.157
91.23	0.077 ± 0.028	0.083 ± 0.061	0.122 ± 0.042
92.23	0.091 ± 0.089	-0.084 ± 0.184	0.012 ± 0.134
93.23	0.073 ± 0.106	-0.309 ± 0.214	0.088 ± 0.159
94.22	0.043 ± 0.134	0.194 ± 0.308	0.099 ± 0.173
1991			
88.48	-0.053 ± 0.126	-0.035 ± 0.259	-0.112 ± 0.177
89.47	-0.114 ± 0.087	-0.211 ± 0.198	-0.070 ± 0.113
90.23	-0.180 ± 0.071	-0.268 ± 0.141	-0.155 ± 0.096
91.24	-0.009 ± 0.017	0.005 ± 0.036	0.016 ± 0.023
91.97	0.092 ± 0.063	-0.028 ± 0.116	0.094 ± 0.086
92.97	0.160 ± 0.081	0.308 ± 0.153	0.143 ± 0.112
93.72	0.045 ± 0.083	-0.061 ± 0.178	0.004 ± 0.108

Table 5.3 Forward-backward charge asymmetry for three event samples for the various energy points obtained with an unbinned likelihood fit. The first sample is the maximum sample with the smallest statistical errors. The second sample (check 1) consists of events with an isolated muon, and uses the charge as determined in the muon chamber. The third sample (check 2) uses events which fulfill strict requirements on the tracks. All results are consistent.

The first sub sample uses only those events that contain an isolated muon. This sample has the lowest statistics, but makes no use of the TEC to determine the charge. The resulting asymmetry for the 483 events for 1990 and 1417 events for 1991 that have been used are listed in the second column of table 5.3 (check 1).

The second sub sample uses only events that have the charge determined from the TEC. All tracks should be more than 15 mrad away from the wire planes and the charges should be $+1 \leftrightarrow -1$. The asymmetry for this sub sample of 952 events for 1990 and 3070 events for 1991 is listed in the third column of table 5.3 (check 2).

The three samples listed in table 5.3 give compatible results for the charge asymmetry. The values for the off peak energy points of the muon sub sample (check 1) for the 1990 period are based on only a few events. The three methods described in the previous sections also give similar results for the maximum sample as can be seen by comparing the results listed in table 5.1–5.3. The systematic error on the asymmetry, 0.003, as estimated in section 5.4, is much smaller than the current statistical error, even for the combined 1990 and 1991 measurements

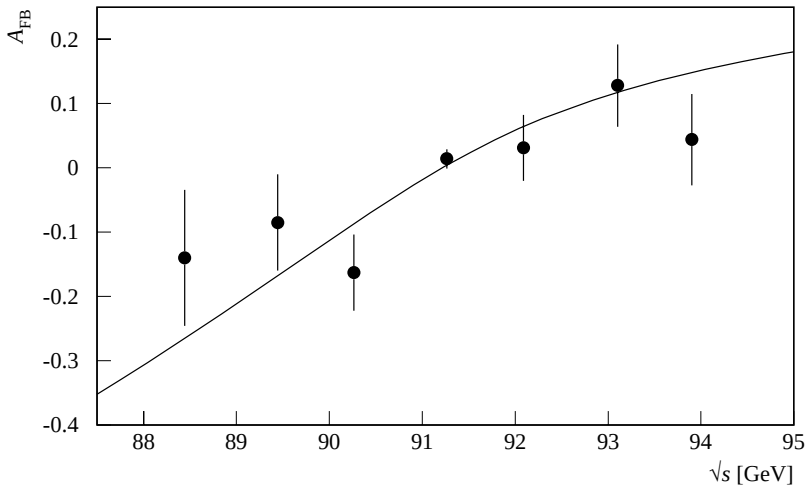

Figure 5.6 Measurement of the forward-backward charge asymmetry compared to the standard model prediction using the ZFITTER program with the Higgs mass set to 300 GeV and the top mass to 140 GeV. The data points are the combined results of the 1990 and 1991 measurements.

on the Z^0 peak.

The results from the unbinned likelihood fit to the maximum sample (first column of table 5.3) have been combined for the 1990 and 1991 data sample and are displayed in figure 5.6 and compared to the standard model prediction. The standard model prediction has been obtained using the ZFITTER program [12] with the mass of the Higgs set to 300 GeV and the top mass to 140 GeV. The measurements are in good agreement with the prediction.

Chapter 6

Interpretation of the results

In this chapter the cross section and asymmetry measurements described in the previous chapters are interpreted in terms of the Standard Model. The analytical program ZFITTER [12] is used together with the MINUIT [48] program to fit the data and to determine the electroweak parameters. ZFITTER includes electroweak radiative corrections to $\mathcal{O}(\alpha)$ and a common exponentiation of initial and final state bremsstrahlung. It also takes into account the leading $\mathcal{O}(\alpha^2 m_{\mathrm{t}}^2/m_{\mathrm{W}}^4)$ corrections from top quark insertions in the gauge boson self-energies. Comparisons have been made between ZFITTER and other programs and one finds agreement in cross section and asymmetry predictions between those programs within 0.5% [9, 12].

The first section in this chapter describes the results of fits to the cross section measurement, the second section describes the results of fits to the combined cross section and asymmetry measurement. The last section gives the L3 result for the measurement of the top mass.

The Standard Model predictions in this chapter are obtained using the values $m_{\mathrm{Z}} = 91.195$ GeV, $m_{\mathrm{t}} = 140$ GeV, $m_{\mathrm{H}} = 300$ GeV and $\alpha_{\mathrm{s}} = 0.120$.

6.1 Mass and width of the Z^0

The mass and width of the Z^0 can be extracted from the total cross section for $\mathrm{e}^+\mathrm{e}^- \to \tau^+\tau^-$ as a function of the center of mass energy. Imposing lepton universality, also the leptonic partial width, Γ_ℓ, can be extracted.

In order to extract these values, a minimum χ^2 fit is performed. The χ^2 function has the following form:

$$\chi^2 = \sum_i \left(\frac{\sigma_i^{\mathrm{t}} - \sigma_i}{\Delta\sigma_i} \right)^2 \tag{6.1}$$

where σ_i^{t} is the theoretical cross section (cf. eq. (1.10) for the lowest order theoretical cross section) and σ_i the measured cross section at the various energies and $\Delta\sigma_i$ is the statistical

error on the measurements.

The systematic errors have been accounted for by introducing scale factors. For the fit to the tau pair cross section, three scale factors were used: one scale factor taking into account the common systematic errors between the 1990 and 1991 data samples (i.e. the errors due to event selection and luminosity determination), and one scale factor for each of the two samples taking into account the uncorrelated systematic errors (i.e. those originating from acceptance and background determination). Each scale factor s_j adds a term $\left((1-s_j)/\Delta_j\right)^2$ to the χ^2 function, where Δ_j is the magnitude of the systematic error. The results of the fit are:

$$\begin{aligned} m_{\mathrm{Z}} &= 91.19 \pm 0.04 \ \text{GeV} \\ \Gamma_{\mathrm{Z}} &= 2488 \pm 65 \ \text{MeV} \\ \Gamma_{\ell} &= 83.5 \pm 1.9 \ \text{MeV} \end{aligned}$$

with $\chi^2/N_{\mathrm{DOF}} = 3.7/8$, where $\Gamma_{\ell} \equiv \sqrt{\Gamma_{\mathrm{e}}\Gamma_{\tau}}$ in this case. The extracted values for the scale factors deviated from unity by less than 0.1% for all fits presented in this chapter. The uncertainty on the absolute energy scale of LEP must be added to the error on m_{Z} and Γ_{Z}. This uncertainty was ± 20 MeV for 1990 [49] and ± 5.2 MeV for 1991 [50], resulting in an additional uncertainty of 7 (5) MeV for m_{Z} (Γ_{Z}) for the combined data sample [9]. The values are in good agreement with standard model predictions for a Z^0 mass of 91.195 GeV:

$$\begin{aligned} \Gamma_{\mathrm{Z}} &= 2487 \ \text{MeV} \\ \Gamma_{\ell} &= 83.6 \ \text{MeV} \end{aligned}$$

Figure 6.1 shows the measured cross sections, together with the result of the fit. Also shown are the cross section predictions for two and four light neutrinos. The data are clearly inconsistent with the latter predictions.

In order to determine Γ_{e} and Γ_{τ} separately, the cross section measurements for the Bhabha scattering process must also be included. The Bhabha cross section data are taken from ref. [9] and concern the s-channel contribution only* (see also section 4.2). A fit similar to the one described above is then performed to the combined tau pair and electron pair cross sections. The values extracted are:

$$\begin{aligned} m_{\mathrm{Z}} &= 91.19 \pm 0.03 \ \text{GeV} \\ \Gamma_{\mathrm{Z}} &= 2507 \pm 48 \ \text{MeV} \\ \Gamma_{\mathrm{e}} &= 83.2 \pm 1.5 \ \text{MeV} \\ \Gamma_{\tau} &= 84.7 \pm 1.8 \ \text{MeV} \end{aligned}$$

with $\chi^2/N_{\mathrm{DOF}} = 13.8/19$. The values for the partial widths are again in good agreement with the Standard Model prediction and support the assumption of lepton universality.

*The non s-channel subtraction and the extrapolation to the full solid angle leads to an overall systematic error of 0.5% for the Bhabha channel and has been taken into account in the fit.

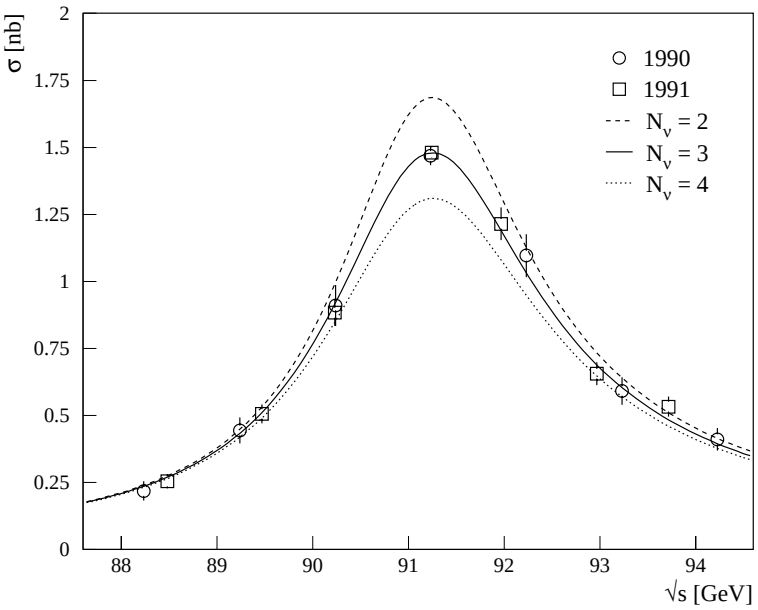

Figure 6.1 Z^0 lineshape for the combined 1990 and 1991 data samples for $e^+e^- \rightarrow \tau^+\tau^-(\gamma)$, together with the result of the fit (solid line). Also shown are the cross section predictions for two and four types of light neutrinos.

Combining the different Z^0 decay channels, global fits have been performed to L3 cross section data available for the 1990 and 1991 data taking periods. The selection of the tau pairs for the cross sections used in these fits was almost identical to the selection presented in this thesis for the 1990 period and very similar for the 1991 period. The cross sections for all four channels, $e^+e^- \rightarrow hadrons$, e^+e^-, $\mu^+\mu^-$ and $\tau^+\tau^-$ are displayed in figure 6.2 together with the lineshape curve resulting from the fit. The results from the fit are presented in table 6.1. The six parameter fit, extracting m_Z, Γ_Z, Γ_{had}, Γ_e, Γ_μ and Γ_τ, shows that the leptonic partial widths Γ_e, $\Gamma_\mu$and Γ_τ are in good agreement with one another thus supporting the hypothesis of lepton universality, which is used in a four parameter fit. The results of this fit are also listed in table 6.1. An additional uncertainty of 7 (5) MeV must be ascribed to m_Z (Γ_Z) for both the six and four parameter fit, originating from the LEP energy calibration.

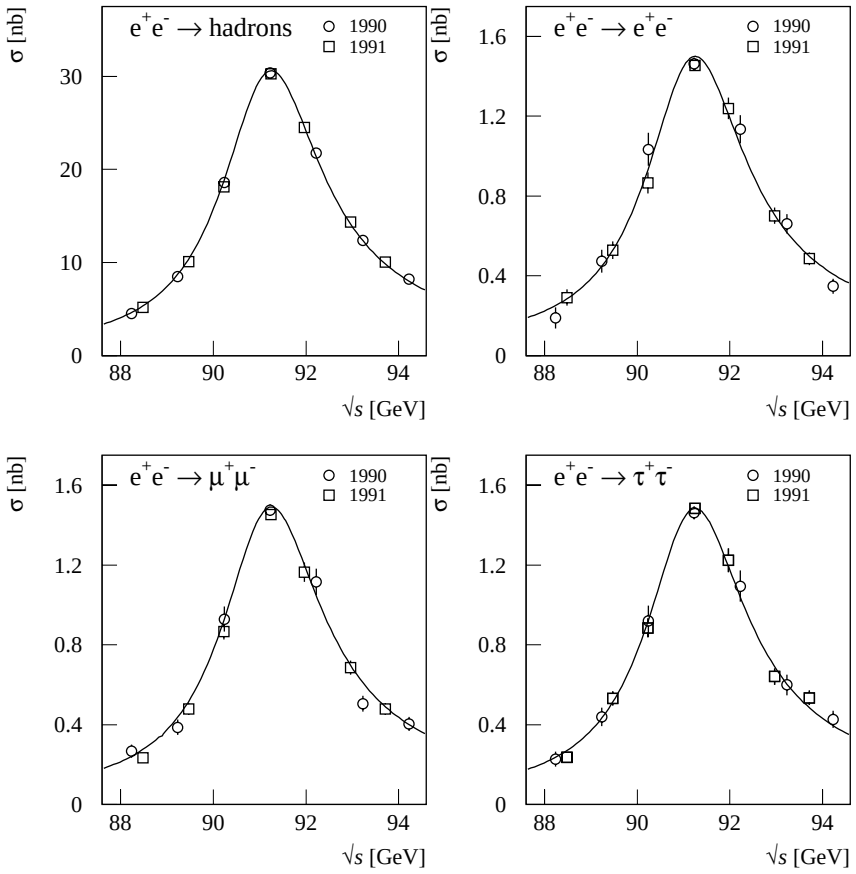

Figure 6.2 Z^0 lineshapes for the combined 1990 and 1991 data samples for $e^+e^- \to \mathrm{hadrons}$, e^+e^-, $\mu^+\mu^-$ and $\tau^+\tau^-$.

6.2 Effective weak neutral current coupling constants

Using the tau pair forward-backward asymmetry A_{FB} as well as the tau pair total cross section data, one can determine the effective Z^0 vector and axialvector couplings $|\bar{g}_{\mathrm{A}}|$ and $|\bar{g}_{\mathrm{V}}|$ (cf. eq. (1.10) and (1.16)). The relative sign of these couplings can be determined from the

Parameter	Six parameter fit	Four parameter fit
m_{Z}	91.195 ± 0.006 GeV	91.195 ± 0.006 GeV
Γ_{Z}	2490 ± 10 MeV	2490 ± 10 MeV
Γ_{had}	1750 ± 13 MeV	1747 ± 11 MeV
Γ_{e}	83.0 ± 0.6 MeV	
Γ_{μ}	82.8 ± 1.0 MeV	
Γ_{τ}	84.6 ± 1.2 MeV	
Γ_{ℓ}		83.1 ± 0.5 MeV

Table 6.1 Results of the six and four parameter fits to the cross section data of $\mathrm{e^+e^-} \to \mathrm{hadrons}$, $\mathrm{e^+e^-}$, $\mu^+\mu^-$ and $\tau^+\tau^-$.

tau polarization (see eq. (1.20) and ref. [51]) and including results from neutrino scattering experiments [52] determines the absolute sign. A fit is performed to extract m_{Z}, Γ_{Z}, $\bar{g}_{\mathrm{A}}$ and $\bar{g}_{\mathrm{V}}$, assuming lepton universality. The values extracted are:

$$\begin{aligned} m_{\mathrm{Z}} &= 91.19 \pm 0.04 \ \text{GeV} \\ \Gamma_{\mathrm{Z}} &= 2494 \pm 65 \ \text{MeV} \\ \bar{g}_{\mathrm{V}} &= -0.045^{+0.015}_{-0.011} \\ \bar{g}_{\mathrm{A}} &= -0.500 \pm 0.006 \end{aligned}$$

with a value of $\chi^2/N_{\mathrm{DOF}} = 20.2/20$. The values for the effective couplings are in good agreement with the standard model predictions:

$$\begin{aligned} \bar{g}_{\mathrm{V}} &= -0.034 \\ \bar{g}_{\mathrm{A}} &= -0.501 \end{aligned}$$

The results of the fit regarding $\bar{g}_{\mathrm{A}}$ and $\bar{g}_{\mathrm{V}}$ are shown in figure 6.3 together with the 68% and 90% confidence levels. The standard model predictions for three values of the top mass are also indicated, and the central value is in good agreement with the measurement.

From the tau cross section and asymmetry data one can also extract the parameters $\sin^2\bar{\theta}_{\mathrm{W}}$ and $\bar{\rho}$ instead of $\bar{g}_{\mathrm{A}}$ and $\bar{g}_{\mathrm{V}}$, again assuming lepton universality (cf. eqs. (1.24) and (1.25)). The results of this fit to the tau data only are:

$$\begin{aligned} m_{\mathrm{Z}} &= 91.19 \pm 0.04 \ \text{GeV} \\ \Gamma_{\mathrm{Z}} &= 2500 \pm 45 \ \text{MeV} \\ \sin^2\bar{\theta}_{\mathrm{W}} &= 0.2276^{+0.0052}_{-0.0043} \\ \bar{\rho} &= 1.004 \pm 0.046 \end{aligned}$$

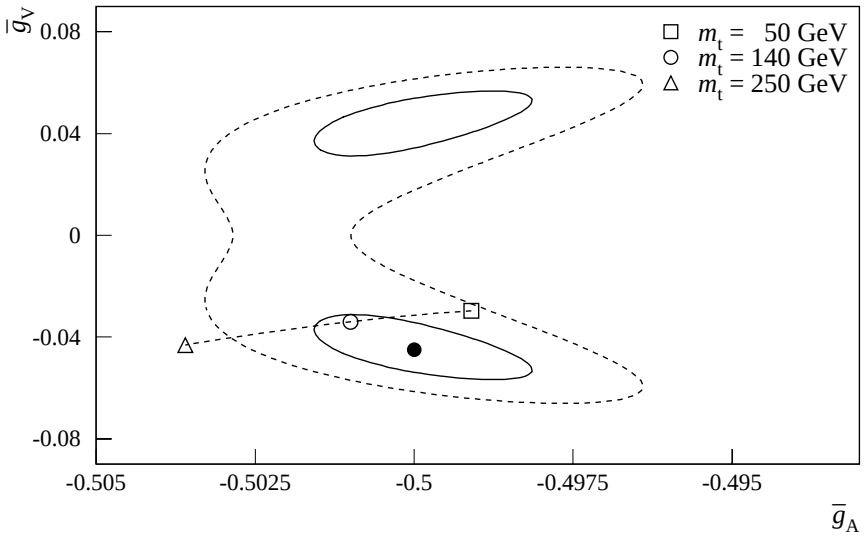

Figure 6.3 The result of the fit to the tau cross section and asymmetry data extracting $\bar{g}_A$ and $\bar{g}_V$, assuming lepton universality. The black point shows the result of the fit and the solid (dashed) line shows the 68% (90%) confidence level contour. The standard model prediction for different values of the top mass is also indicated.

which compares well to the standard model values:

$$\begin{aligned} \sin^2\bar{\theta}_W &= 0.2332 \\ \bar{\rho} &= 1.002 \end{aligned}$$

After including also the cross section and asymmetry data for the Bhabha scattering process a fit is performed to extract separately the values for $\bar{g}_A^e$, $\bar{g}_V^e$, $\bar{g}_A^\tau$ and $\bar{g}_V^\tau$. The results of the fit are:

$$\begin{aligned} m_Z &= 91.19 \pm 0.03 \text{ GeV} \\ \Gamma_Z &= 2545 \pm 48 \text{ MeV} \\ \bar{g}_V^e &= -0.037 \pm 0.015 \\ \bar{g}_A^e &= -0.506 \pm 0.004 \\ \bar{g}_V^\tau &= -0.055 \pm 0.038 \\ \bar{g}_A^\tau &= -0.507 \pm 0.007 \end{aligned}$$

with a value of $\chi^2/N_{DOF} = 35.9/43$. The corresponding values for the effective coupling

Parameter	Nine parameter fit	Five parameter fit
m_{Z} (MeV)	$91195 \pm 6 \pm 7$ (LEP)	$91195 \pm 6 \pm 7$ (LEP)
Γ_{Z} (MeV)	$2490 \pm 10 \pm 5$ (LEP)	$2490 \pm 10 \pm 5$ (LEP)
σ^0_{had} (nb)	41.34 ± 0.28	41.34 ± 0.28
$\bar{g}^{\mathrm{e}}_{\mathrm{A}}$	-0.4980 ± 0.0021	
$\bar{g}^{\mathrm{e}}_{\mathrm{V}}$	$-0.040^{+0.013}_{-0.011}$	
$\bar{g}^{\mu}_{\mathrm{A}}$	$-0.4968^{+0.0050}_{-0.0037}$	
$\bar{g}^{\mu}_{\mathrm{V}}$	$-0.048^{+0.021}_{-0.033}$	
$\bar{g}^{\tau}_{\mathrm{A}}$	-0.5032 ± 0.0038	
$\bar{g}^{\tau}_{\mathrm{V}}$	-0.037 ± 0.008	
$\bar{g}_{\mathrm{A}}$		-0.4986 ± 0.0015
$\bar{g}_{\mathrm{V}}$		$-0.040^{+0.006}_{-0.005}$

Table 6.2 Results of the nine and five parameter fits to the cross section, lepton asymmetry and tau polarization data [9].

constants for electrons and taus are in good agreement with each other and with the results from the fit to the tau data only. This again supports the assumption of lepton universality.

Global fits have been performed to the leptonic forward-backward asymmetries A_{FB} as well as the τ polarization $\mathcal{P}_\tau$ in addition to the total cross section data for $\mathrm{e^+e^-} \rightarrow \mathrm{e^+e^-}$, $\mu^+\mu^-$, $\tau^+\tau^-$ and $\mathrm{hadrons}$ [9]. As mentioned in the previous section, the tau selection for the sample used in those fits was very similar to the selection described in this thesis. The Z^0 vector and axialvector couplings $\bar{g}_{\mathrm{A}}$ and $\bar{g}_{\mathrm{V}}$ to lepton pairs can be extracted. Inclusion of the τ polarization significantly improves the error obtained for $\bar{g}^{\tau}_{\mathrm{V}}$ and determines the relative sign of the couplings. Not assuming lepton universality the nine fitted parameters are: m_{Z}, Γ_{Z}, σ^0_{had}, $\bar{g}^{\mathrm{e}}_{\mathrm{A}}$, $\bar{g}^{\mathrm{e}}_{\mathrm{V}}$, $\bar{g}^{\mu}_{\mathrm{A}}$, $\bar{g}^{\mu}_{\mathrm{V}}$, $\bar{g}^{\tau}_{\mathrm{A}}$ and $\bar{g}^{\tau}_{\mathrm{V}}$, where σ^0_{had} is the measured hadronic cross section on the peak corrected for photon radiation.

Results from this fit are given in the first column of table 6.2. The relative sign of the vector and axialvector coupling to the tau is determined to be positive. Since all other signs for the coupling constants are not determined in this fit, they are taken to be negative, in agreement with the results from neutrino-electron scattering experiments [52]. Comparing the resulting error values for the coupling constants for muons and taus shows the significant effect of the inclusion of the tau polarization measurement. The error on $\bar{g}^{\tau}_{\mathrm{V}}$ is reduced to about one third of the corresponding muon value.

Again, the results are in good agreement with a universal weak neutral current coupling to charged leptons. The fit is thus repeated imposing that $\bar{g}_{\mathrm{A}}$ and $\bar{g}_{\mathrm{V}}$ are the same for all charged leptons, reducing the number of free parameters to five. The result is shown in the second

column of table 6.2.

At increasing statistics, the above results will improve. Not only will the statistical error go down with an increase in the number of events, larger samples will also allow more thorough investigations of the systematics involved. In 1992 all of the data were taken on the peak of the Z^0 resonance with increased luminosity, resulting in almost twice as many events as the combined 1990 and 1991 data sample. For the 1993 data taking period the data will be taken more at the off peak energy points, to improve the measurement on Γ_Z and m_Z.

6.3 Limit on the top mass

A simultaneous fit to all cross section, lepton asymmetry, $b\bar{b}$ asymmetry, tau polarization, and tau decay width data has been performed in the framework of the Standard Model, for different values of the Higgs mass, $m_H = 50$, 300, 1000 GeV. From this fit the top mass m_t can be extracted (cf. eq. (1.28)). The value of $\alpha_s = 0.124 \pm 0.006$ extracted from the hadronic event topology and the tau decay measurement has been used as a constraint in the fit. The value thus obtained for the top mass in the Standard Model is [9]:

$$m_t = 152^{+36}_{-46} \pm 20\ (\text{Higgs})\ \text{GeV}$$

This is in agreement with current direct experimental mass limits on the Standard Model top mass, which are $m_t > 108$ GeV from the CDF collaboration [53] and $m_t > 103$ GeV from the D0 collaboration [54].

References

[1] UA1 Collaboration, G. Arnison et al., "Experimental observation of isolated large transverse energy electrons with associated missing energy at $\sqrt{s} = 540$ GeV", *Phys. Lett.* B122 (1983) 103;
UA1 Collaboration, G. Arnison et al., "Experimental observation of lepton pairs of invariant mass around 95 GeV$/c^2$ at the CERN SPS collider", *Phys. Lett.* B126 (1983) 398;
UA2 Collaboration, P. Bagnaia et al., "Evidence for $\mathrm{Z}^0 \to \mathrm{e}^+\mathrm{e}^-$ at the CERN $\bar{\mathrm{p}}\mathrm{p}$ collider", *Phys. Lett.* B129 (1983) 130.

[2] M. Bernardini et al., "Limits on the mass of heavy leptons", *Nuovo Cimento* 17A (1973) 383;
M. Orito et al., "A search for heavy leptons with $\mathrm{e}^+\mathrm{e}^-$ colliding beams", *Phys. Lett.* B48 (1974) 165.

[3] M.L. Perl et al., "Evidence for anomalous lepton production in $\mathrm{e}^+\mathrm{e}^-$ annihilation", *Phys. Rev. Lett.* 35 (1975) 1489.

[4] M. Kobayashi and T. Maskawa, "CP-violation in the renormalizable theory of weak interaction", *Prog. Theor. Phys.* 49 (1973) 652.

[5] S.W. Herb et al., "Observation of a dimuon resonance at 9.5 GeV in 400-GeV proton nucleus collisions", *Phys. Rev. Lett.* 39 (1977) 252.

[6] S.L. Glashow, "Partial-symmetries of weak interactions", *Nucl. Phys.* 22 (1961) 579;
S. Weinberg, "A model of leptons", *Phys. Rev. Lett.* 19 (1967) 1264;
A. Salam, "Relativistic groups and analyticity", In N. Svartholm, editor, *Elementary Particle Theory*, page 369. Almquist and Wiksell, Stockholm, 1968.

[7] P.W. Higgs, "Broken symmetries, massless particles and gauge fields", *Phys. Lett.* B351 (1964) 132;
P.W. Higgs, "Broken symmetries and the masses of gauge bosons", *Phys. Rev. Lett.* 13 (1964) 508;
P.W. Higgs, "Spontaneous symmetry breakdown without massless bosons", *Phys. Rev.* 145 (1966) 1156;

F. Englert and R. Brout, "Broken symmetry and the mass of gauge vector mesons", *Phys. Rev. Lett.* 13 (1964) 321.

[8] M. Consoli and W. Hollik, "Z physics at LEP 1", *CERN 89-08* Vol. 1 (1989) 7.

[9] L3 Collaboration, O. Adriani et al., "Results from the the L3 experiment at LEP", *CERN-PPE/93-31* (1993).

[10] M. Böhm and W. Hollik, "Z physics at LEP 1", *CERN 89-08* Vol. 1 (1989) 203.

[11] S. Jadach and Z. Wąs, "Z physics at LEP 1", *CERN 89-08* Vol. 1 (1989) 235.

[12] D. Bardin et al., "An analytical program for fermion pair production in e^+e^- annihilation", *CERN-TH 6443* (1992).

[13] LEP design report, "The LEP injector chain", *CERN-LEP/TH/83-29* vol. I (1983).

[14] LEP design report, "The LEP main ring", *CERN-LEP/TH/84-01* vol. II (1984).

[15] L3 Collaboration, B. Adeva et al., "The construction of the L3 experiment", *Nucl. Instr. and Meth.* A289 (1990) 35.

[16] ALEPH Collaboration, D. Decamp et al., "ALEPH: a detector for electron-positron annihilations at LEP", *Nucl. Instr. and Meth.* A294 (1990) 121.

[17] OPAL Collaboration, K. Ahmet et al., "The OPAL detector at LEP", *Nucl. Instr. and Meth.* A305 (1991) 275.

[18] DELPHI Collaboration, P. Aarnio et al., "The DELPHI detector at LEP", *Nucl. Instr. and Meth.* A303 (1991) 233.

[19] R. Wilhelm, "The L3 event visualisation system and its use in the Z^0 line shape analysis", PhD thesis, University of Amsterdam, December 1992.

[20] H. Akbari et al., "The L3 vertex detector: Design and performance", *Nucl. Instr. and Meth.* A315 (1992) 161.

[21] F. Beissel et al., "Construction and performance of the L3 central tracking detector", *Nucl. Instr. and Meth.* A332 (1993) 33.

[22] M. Merk, "Study of Bhabha scattering at the Z^0-resonance using the L3 detector", PhD thesis, University of Nijmegen, September 1992.

[23] T. Foreman, "Bottom quark production at the Z resonance", PhD thesis, University of Amsterdam, June 1993.

[24] L3 Collaboration, B. Adeva et al., "Measurement of electroweak parameters from hadronic and leptonic decays of the Z^0", *Z. Phys.* C51 (1991) 179.

[25] O. Adriani et al., "Hadron calorimetry in the L3 detector", *Nucl. Instr. and Meth.* A302 (1991) 53.

[26] Yue Peng, "The muon spectrometer of the L3 detector at LEP", PhD thesis, University of Amsterdam, December 1988.

[27] P. Duinker et al., "Some methods and tools for testing and optimizing proportional wire chambers", *Nucl. Instr. and Meth.* A273 (1988) 814.

[28] J.G. Branson, private communication.

[29] X. Leijtens, "The electro-optical alignment system for the L3 muon chambers", Master's thesis, University of Amsterdam, June 1988.

[30] R. Fabbretti et al., "The laser beacon", *Nucl. Instr. and Meth.* A280 (1989) 13.

[31] M. Fabre, "The dimuon mass resolution of the L3 experiment at LEP", PhD thesis, Swiss Federal Institute of Technology Zürich, 1992.

[32] B. Adeva et al., "Test results of the L3 precision muon detector", *Nucl. Instr. and Meth.* A289 (1990) 335.

[33] C. Timmermans, "Measurement of muon pair production around the Z-resonance using the L3 detector at LEP", PhD thesis, University of Nijmegen, April 1992.

[34] Lin Li, "Precision muon spectrometry in the L3 experiment at LEP", PhD thesis, Swiss Federal Institute of Technology Zürich, 1991.

[35] Particle Data Group, "Review of particle properties", *Phys. Rev.* D45 (1992) II.3.

[36] F.A. Berends, P.H. Daverveldt and R. Kleiss, "Total and visible cross sections for multi-lepton events in e^+e^- collisions", *Phys. Lett.* B148 (1984) 489.

[37] H. Janssen and J. Karyotakis, "Four lepton events with the L3 detector", *L3 Note* 1119 (1992).

[38] S. Jadach et al., "Z physics at LEP 1", *CERN 89-08* Vol. 3 (1989) 69.

[39] M. Böhm, A. Denner and W. Hollik, "Radiative corrections to Bhabha scattering at high energies (I)", *Nucl. Phys.* B304 (1988) 687.

[40] F.A. Berends, R. Kleiss and W. Hollik, "Radiative corrections to Bhabha scattering at high energies (II)", *Nucl. Phys.* B304 (1988) 712.

[41] T. Sjöstrand, "Z physics at LEP 1", *CERN 89-08* Vol. 3 (1989) 143.

[42] F.A. Berends, P.H. Daverveldt and R. Kleiss, "Complete lowest-order calculations for four-lepton final states in electron-positron collisions", *Nucl. Phys.* B253 (1985) 441.

[43] R. Brun, F. Bruyant, M. Maire, A.C. McPherson and P. Zanarini, "GEANT3 users guide", *CERN DD/EE/84-1* (1987).

[44] T.S. Dai and T. Foreman, "Determination of the muon chamber efficiency in the 1990 data", *L3 note 954* (1990).

[45] M.W. Grünewald, "Measurement of the tau-pair cross section and charge asymmetry at the Z^0 resonance", PhD thesis, California Institute of Technology, 1993.

[46] J. Qian, "Study of muon pair production at LEP", PhD thesis, Massachusetts Institute of Technology, November 1990.

[47] W. Beenakker, F.A. Berends and S.C. van der Marck, "Large-angle Bhabha scattering", *Nucl. Phys.* B349 (1991) 323.

[48] F. James and M. Roos, "MINUIT manual", *CERN D506* (1989).

[49] R. Bailey et al., "LEP energy calibration", *CERN SL/90-95* (1990).

[50] The working group on LEP energy, L. Arnaudon et al., "Measurement of the mass of the Z boson and the energy calibration of LEP", *CERN PPE/93-53* (1993).

[51] L3 Collaboration, O. Adriani et al., "A measurement of τ polarization in Z^0 decays", *Phys. Lett.* B292 (1992) 472.

[52] CHARM Collaboration, J. Dorenbosch, et al., "Experimental results on neutrino-electron scattering", *Z. Phys.* C41 (1989) 567;
K. Abe et al., "Determination of $\sin^2\theta_w$ from measurements of differential cross sections for muon-neutrino and -antineutrino scattering by electrons", *Phys. Rev. Lett.* 62 (1989) 1709;
CHARM II Collaboration, D. Geiregat et al., "A new determination of the electroweak mixing angle from muon-neutrino-electron scattering", *Phys. Lett.* B232 (1989) 539;
F. Avignone et al., "Interpretation of $\overline{\nu}$-e^- scattering with reactor antineutrinos", *Phys. Rev.* D16 (1977) 2383;
U. Amaldi et al., "Comprehensive analysis of data pertaining to the weak neutral current and the intermediate-vector-boson masses", *Phys. Rev.* D36 (1987) 1385.

[53] A. Caner for the CDF Collaboration, XXVIIIth Rencontres de Moriond, March 1993, to be published.

[54] M. Narian for the D0 Collaboration, XXVIIIth Rencontres de Moriond, March 1993, to be published.

Summary

After completion of the Large Electron-Positron collider LEP in 1989, a vast quantity of data became available for research of the Standard Model parameters. The standard model is the theory describing the interactions between all fundamental particles. The energy of the electrons and positrons (anti-electrons) accelerated by LEP can be tuned to produce the Z^0 boson in large quantities. Together with the $\mathrm{W}^{\pm}$ bosons, the Z^0 is the carrier of the weak force. It decays almost instantaneously in two particles: one of the fundamental particles and its anti-particle. More than 3% of all decays of the Z^0 produce a positively and a negatively charged tau particle. Tau particles are predicted to be identical to electrons, except for their mass: the tau is about 3400 times as heavy as the electron. The production of tau pairs from Z^0 decay is the topic of research of this thesis. Chapter 1 gives a theoretical introduction and presents the expressions for the cross section and the decay width for the process $\mathrm{e}^+\mathrm{e}^- \rightarrow \tau^+\tau^-$. In addition the forward-backward charge asymmetry is treated. From these measurable quantities the magnitude of the coupling constants $\bar{g}_{\mathrm{A}}$ and $\bar{g}_{\mathrm{V}}$ can be determined. These constants are important Standard Model parameters.

Chapter 2 discusses briefly the LEP collider and in detail the L3 detector, the apparatus used for obtaining the experimental data. The L3 detector is housed in a solenoidal magnet which measures about 12 m in length and 12 m in diameter. The accelerated electrons and positrons collide in the center of the detector. From the inside out the main detector components are described. The central part is a wire chamber, detecting the tracks of all charged particles. Surrounding this is an electromagnetic calorimeter accurately measuring the energy of electrons and photons. The next sub detector is the hadron calorimeter, absorbing all hadrons and measuring their energy. The outside of the detector consists of three layers of the muon spectrometer, measuring the momenta of muons with high precision.

In chapter 3 the RASNIK alignment system is treated. This alignment system is necessary in order to reach the high accuracy of the muon momentum measurement. Both the hardware and the software implementation are described. The RASNIK alignment system is proven to be very stable and the accuracy is better than required.

Chapter 4 discusses the determination of the production cross section of tau pairs. The possible backgrounds are discussed and the selection criteria that have been used are listed. The combined 1990 and 1991 data sample contains over 9500 tau pair events selected with a

purity of 97%. The cross section of the process $e^+e^- \to Z^0, \gamma \to \tau^+\tau^-(\gamma)$ at the Z^0 at a center of mass energy of 91.2 GeV is determined to be: $\sigma_{\tau^+\tau^-} = 1.478 \pm 0.017 \pm 0.015$ nb. The errors are statistical and systematic respectively and the systematic error includes the 0.6% contribution of the luminosity measurement. The forward-backward charge asymmetry A_{FB} for tau pairs is determined in chapter 5. The possible backgrounds are discussed. The asymmetry is extracted using three different methods and the results are compared. As an additional test, one of the three methods, the maximum likelihood method, is also applied to two sub samples. All results are in agreement. Corrected for the background the value extracted for the forward-backward charge asymmetry at a center of mass energy of 91.2 GeV is: $A_{FB} = (0.014 \pm 0.015 \pm 0.003)\%$.

The last chapter interprets the results in the framework of the Standard Model. Using only the values for the cross section for tau pair production, the values for the mass and the width of the Z^0 are determined to be $m_Z = 91.19 \pm 0.04$ GeV and $\Gamma_Z = 2488 \pm 65$ MeV. If one assumes (in agreement with all experimental results) that the coupling of leptons (e, μ, τ) to the Z^0 is the same for all leptons, the partial width of the Z^0 in leptons (Γ_ℓ) can be determined using only the tau data: $\Gamma_\ell \equiv \sqrt{\Gamma_e \Gamma_\tau} = 83.5 \pm 1.9$ MeV. With the same assumption and including the measurements of the charge asymmetry one can determine the magnitude of the coupling constants as well: $\bar{g}_V = -0.045^{+0.015}_{-0.011}$ and $\bar{g}_A = -0.500 \pm 0.006$. After combining the results with those of other Z^0 decay channels a higher accuracy is achieved: $m_Z = 91.195 \pm 0.006$ GeV, $\Gamma_Z = 2490 \pm 10$ MeV, $\bar{g}_V = -0.040^{+0.006}_{-0.005}$ and $\bar{g}_A = -0.4986 \pm 0.0015$. An additional error of 7 (5) MeV must be ascribed to m_Z (Γ_Z) caused by the uncertainty in the LEP energy calibration. Within the Standard Model, the top quark mass can be extracted from the predicted radiative corrections. The value of the top mass thus determined is: $m_t = 152^{+36}_{-46} \pm 20$ (Higgs) GeV, where the second error reflects the effect of varying the Higgs mass in the range 50–1000 GeV.

Samenvatting

Productie van tau paren bij de Z resonantie

Na het gereedkomen van de 'Large Electron-Positron collider' LEP in 1989 is er een grote hoeveelheid gegevens beschikbaar gekomen voor onderzoek aan de parameters van het Standaard Model, de theorie die de wisselwerking tussen alle fundamentele deeltjes beschrijft. De energie van de bij LEP versnelde electronen en positronen (anti-electronen) kan zo worden ingesteld dat Z^0 bosonen in grote hoeveelheden worden geproduceerd. Het Z^0 boson is, samen met de $\mathrm{W}^{\pm}$ bosonen, drager van de zwakke kracht. Het Z^0 boson vervalt vrijwel direct in twee deeltjes: één van de fundamentele deeltjes en het bijbehorende anti-deeltje. Van alle vervalsmogelijkheden van dit Z^0 boson resulteert ruim 3% in een positief en een negatief geladen tau deeltje. Tau deeltjes worden geacht in alle opzichten gelijk te zijn aan electronen, behalve wat betreft de massa: de tau massa is ruwweg 3400 keer zo groot als die van het electron. Het onderzoek aan de productie van tau paren door Z^0 verval vormt het onderwerp van dit proefschrift.

Hoofdstuk 1 geeft een theoretische inleiding en behandelt de voorspellingen voor de werkzame doorsnede, de vervalsbreedte en de voorwaarts-achterwaarts ladingsasymmetrie voor het proces $\mathrm{e}^+\mathrm{e}^- \rightarrow \tau^+\tau^-$. Uit deze meetbare grootheden kan de grootte van de koppelingsconstanten $\bar{g}_{\mathrm{V}}$ en $\bar{g}_{\mathrm{A}}$ worden bepaald. Deze constanten zijn belangrijke parameters van het Standaard Model.

Hoofdstuk 2 behandelt kort de LEP versneller en in detail de L3 detector, het apparaat waarmee de experimentele gegevens zijn verkregen. De gehele L3 detector bevindt zich in een solenoïde van ongeveer 12 m lengte en 12 m diameter. De versnelde electronen botsen in het centrum van de detector. Van binnen naar buiten bestaat de L3 detector uit: 1) een centrale detector die sporen van alle geladen deeltjes registreert en hun impuls bepaalt; 2) een electromagnetische calorimeter die nauwkeurig de energieën en richtingen van electronen en fotonen meet; 3) een hadronische calorimeter waar de hadronen geabsorbeerd worden en de energieën en richtingen worden bepaald; 4) een muon spectrometer die de sporen van muonen registreert en hun impuls nauwkeurig bepaalt.

In hoofstuk 3 wordt het RASNIK uitlijnsysteem van de muon spectrometer beschreven. Dit uitlijnsysteem is nodig om de hoge resolutie voor de muon impuls meting te realiseren. Zowel de hardware als de software implementatie van dit systeem wordt besproken. Het RASNIK

uitlijnsysteem blijkt erg stabiel en de nauwkeurigheid is beter dan vereist.

Hoofdstuk 4 behandelt de bepaling van de werkzame doorsnede voor de productie van tau paren. De selectie criteria om tot een zuivere verzameling van tau paren te komen en de mogelijke achtergronden worden besproken. In totaal zijn voor 1990 en 1991 ruim 9500 tau-paar gebeurtenissen geselecteerd, met een zuiverheid van 97%. De werkzame doorsnede voor het proces $\mathrm{e^+e^-} \to \mathrm{Z}^0, \gamma \to \tau^+\tau^-(\gamma)$ bij een zwaartepuntsenergie corresponderend met de Z^0 resonantiepiek (91.2 GeV) wordt bepaald op: $\sigma_{\tau^+\tau^-} = 1.478 \pm 0.017 \pm 0.015$ nb, waar de fouten respectievelijk statistisch en systematisch zijn.

In hoofdstuk 5 wordt de waarde van de voorwaarts-achterwaarts ladingsasymmetrie (A_{FB}) van tau paren bepaald. De mogelijke achtergronden en de daaruit voortvloeiende correcties worden besproken. Drie methoden voor het bepalen van de ladingsasymmetrie worden behandeld en de resultaten onderling vergeleken. Als extra test is de 'maximum likelihood' methode toegepast op twee deelverzamelingen. Alle aldus verkregen waarden zijn in overeenstemming met elkaar, en de asymmetrie bij een zwaartepuntsenergie van 91.2 GeV wordt bepaald op: $A_{\mathrm{FB}} = (0.014 \pm 0.015 \pm 0.003)\%$.

In het laatste hoofdstuk worden de metingen geïnterpreteerd binnen het raamwerk van het Standaard Model. Uit de gegevens van de werkzame doorsnede voor het proces $\mathrm{e^+e^-} \to \tau^+\tau^-$ als functie van de energie wordt de waarde van de massa en de breedte van de Z^0 bepaald op: $m_{\mathrm{Z}} = 91.19 \pm 0.04$ GeV en $\Gamma_{\mathrm{Z}} = 2488 \pm 65$ MeV. Indien (in overeenstemming met alle experimentele resultaten) wordt aangenomen dat de koppelingen aan de Z^0 gelijk zijn voor alle geladen leptonen (e, μ, τ), dan kan de vervalsbreedte van de Z^0 in leptonen (Γ_ℓ) met alleen de tau gegevens worden bepaald: $\Gamma_\ell \equiv \sqrt{\Gamma_{\mathrm{e}}\Gamma_\tau} = 83.5 \pm 1.9$ MeV. Als onder dezelfde aanname ook de meting van de ladingsasymmetrie wordt gebruikt, dan kunnen eveneens de koppelingsconstanten worden bepaald: $\bar{g}_{\mathrm{V}} = -0.045^{+0.015}_{-0.011}$ en $\bar{g}_{\mathrm{A}} = -0.500 \pm 0.006$. Door de meetresultaten te combineren met die van andere Z^0 vervalskanalen kunnen de bovengenoemde parameters nauwkeuriger worden bepaald: $m_{\mathrm{Z}} = 91.195 \pm 0.006$ GeV, $\Gamma_{\mathrm{Z}} = 2490 \pm 10$ MeV, $\bar{g}_{\mathrm{V}} = -0.040^{+0.006}_{-0.005}$ en $\bar{g}_{\mathrm{A}} = -0.4986 \pm 0.0015$. Een bijkomende onzekerheid van 7 (5) MeV moet worden toegekend aan de waarde van m_{Z} (Γ_{Z}) ten gevolge van de LEP energiecalibratie. Alhoewel het top quark nog niet direkt is waargenomen, kan, met de LEP gegevens en de theoretische voorspellingen voor de invloed van het top quark op de stralingscorrecties, het toegestane massa-gebied voor dit deeltje drastisch worden beperkt. De door L3 bepaalde waarde van de top massa in het Standaard Model is: $m_{\mathrm{t}} = 152^{+36}_{-46} \pm 20\ (\mathrm{Higgs})$ GeV, waarbij de tweede fout het effect van een fluctuatie van de Higgs massa van 50–1000 GeV weergeeft.

Acknowledgements

The analysis presented in this thesis could not have been performed without the combined effort of many people. It is my pleasure to thank all members of the L3 collaboration who contributed to this work in one way or another.
I have enjoyed working with my promotor Piet Duinker. I thank him for introducing me to the L3 experiment and for his guidance and support. I am indebted to Graziano Massaro, my co-promotor, for his supervision and for the pleasant cooperation. I thank Harry van der Graaf and Gerjan Bobbink for their help and supervision.
I would like to thank the members of the L3 muon group. It has been a pleasure to work with them. I thank all members of the monitor group and particularly Jianming Qian, Charles Timmermans, Enrique Gonzalez and Irwin Sheer for the fruitful cooperation in developing and writing the monitoring software. I am grateful for the kind assistance of the mechanical and electronic workshops of NIKHEF. Especially I would like to mention Henk Groenstege, Wim Gotink and Gerard Goede for their help during the installation of the RASNIK hardware.
I thank the members of the lineshape analysis group for many helpful discussions. In particular I would like to mention Hesheng Chen and Hongfang Chen for the fine cooperation and Jianming Qian, Som Ganguli, Andrey Kunin, Frank Filthaut and Raymond Rosmalen for their help and suggestions about the analysis. I am very grateful to Monty IJzerman who continued the tau selection at CERN after my return to Amsterdam. I also much appreciated our discussions about the various programs and calculations.
I thank all my fellow graduate students for, among many other things, their pleasant company at CERN and during the many diners at Manora.
I would like to mention my 'room mate' at NIKHEF, Tim Foreman, for interesting discussions and the sharing of experiences. Thanks also to René Wilhelm for answering my questions about the L3 scan program and about POSTSCRIPT and to Zhang Dehong for discussions about the interpretation of the results.
Graag wil ik mijn ouders bedanken die me de gelegenheid hebben gegeven te studeren. Tenslotte bedank ik mijn familie, vrienden en vooral Marian en Irene. Zij "brachten heel gelaten 't offer aan de wetenschap".

— Xaveer